Element-Sensitive X-Ray Imaging and Computed Tomography Using Energy-Selective Photodetection

Thèse présentée à la Faculté des Sciences
Université de Neuchâtel

Pour l'obtention du grade de docteur ès sciences

Par

Joachim Nüesch

Acceptée sur proposition du jury:
Prof. P. Seitz, directeur de thèse
Prof. A. Dommann
Prof. H. P. Herzig
Prof. H. Stoeckli-Evans

Soutentue le 14 juilet 2010

Université de Neuchâtel
2010

Université de Neuchâtel

FACULTE DES SCIENCES
Secrétariat-Décanat de la faculté
- Rue Emile-Argand 11
- CP 158
- CH-2009 Neuchâtel

IMPRIMATUR POUR LA THESE

Element-Sensitive X-Ray Imaging and Computed Tomography Using Energy-Selective Photodetection

Joachim NÜESCH

UNIVERSITE DE NEUCHATEL

FACULTE DES SCIENCES

La Faculté des sciences de l'Université de Neuchâtel,
sur le rapport des membres du jury

Mme H. Stoeckli-Evans
MM. P. Seitz (IMT-UniNe, directeur de thèse), H.P. Herzig (IMT-EPFL),
et A. Dommann (Hochschule Liechtenstein et CSEM, Neuchâtel)

autorise l'impression de la présente thèse.

Neuchâtel, le 19 juillet 2010

Le doyen :
F. Kessler

Fix Kessler

■ Téléphone : +41 32 718 21 00 ■ E-mail : secretariat.sciences@unine.ch ■ www.unine.ch/sciences

Contents

Abstract

Keywords: X-Ray, transmission, photoabsorption, element detection, microscope, microCT

Mot-clé: rayon-x, transmission, absorption photoélectrique, détection d'élément, microscope, microCT

A new method in X-ray imaging is presented and a proof of concept shown. The proof of concept is done with the simultaneous identification of aluminum, silicon and titanium and the determination of its integrated density. Also some additional measurements are conducted with aqueous solutions. In this case the concentration of sodium chloride and calcium chloride is measured. The result of the method is an elemental distribution in the path of the X-ray photons. The concept has no strict limit of the number of elements simultaneously detectable. The method works in transmission and with a spectral analysis of the absorbed photons. In this work only a single spectrometer is used. The detector can be extended to an array of spectrometers. The method can also be combined with tomography. In this case it is possible to calculate the density of the elements in the voxels of the reconstruction.

The method works in photoabsorption and is therefore optimized for thin biological samples. Experiments conducted are in the energy range of $10\,\mathrm{keV}$–$13\,\mathrm{keV}$ using a X-ray source with $15\,\mathrm{kV_p}$ and with a broad spectrum. The sample can be kept under standard conditions which allows measurements on living tissue. Minute effects on the mass-absorption coefficients are measured in order to identify the elements. Because these fine effects are difficult to detect the stability of the system is important.

The elemental distribution information can be used to increase the contrast of some conventional images or to identify tissues, cells, or even molecules. Therefore functional informations could be added to the images. This would be a strong enhancement in the practical value of X-ray images.

Preface

This doctoral thesis has been carried out at the Nanomedicine Devision of the Center Suisse d'Electronique et de Microtechnique (CSEM) in Landquart.

In the first place I would like to thank Peter Seitz, my thesis supervisor, to have given me the opportunity to conduct this thesis. During the whole period at CSEM he encouraged me in my research and gave me a great support. Furthermore he passes his optimism in searching and finding solutions.

My thanks also go to the following peoples

Alex Dommann for being a member of the jury and for his help in the first calibration of the spectrometer

Hans Peter Herzig and Helen Stoeckli-Evans for being members of this doctoral thesis jury

Rolf Kaufmann for introducing me to the field of X-rays

Max Wiki for all our discussions in our common office

Stefano Cattaneo for his disponibility as my supervisor and his helpful comments on this thesis

Pascal Gaggero for our discussions in the office and the train as well as the hours in the gym

Further I want to thank the whole team of the CSEM Landquart. It was a pleasure to work together with this supporting team. I appreciated its entrepreneurship spirit.

Finally I want to thank my family and friends, especially my wife Véronique, for their support, patience, and motivation.

Landquart, June 2010 Joachim Nüesch

1. Introduction

It was more than 100 years ago, that Wilhelm Conrad Röntgen discovered X-rays, electromagnetic radiation in the energy range of $10\,\mathrm{keV}$ to a few $100\,\mathrm{keV}$. The first images with X-rays were made in the year 1895 (see figure 1.1), and it became immediately clear that X-rays will revolutionize medical diagnostics. This is due to the fact that the linear attenuation coefficient of the human body lies in the range of $0.1\,\frac{1}{\mathrm{cm}}$ to $1\,\frac{1}{\mathrm{cm}}$ for X-rays, making it possible to penetrate the human body and to create images of the body's inner structure. For this reason, several imaging modalities using X-rays have been developed since the time of W. C. Röntgen, including the classic two dimensional radiography (projection images) and the three dimensional reconstruction techniques of Computer Tomography (CT). In this way, absorption-based X-ray imaging techniques have become an indispensable tool for the medical practitioner to create high-resolution structural views of the human body's inner parts.

In addition, technical applications of X-ray imaging modalities represent an important part of the growing domain of non-destructive testing (NDT). Well known examples include the security checks at airports, baggage inspections for arms and explosives, access control to public buildings, quality control in industrial processes, etc.

Despite the many advances made in the various X-ray measurement modalities mentioned above, medical and NDT X-ray imagery still look the same as in the times of W. C. Röntgen: They are essentially grayscale representations of the local X-ray density in the object, showing structural detail of the object under study. In practice, no or very little information can be gained from these images regarding the composition of the sample or even functional details.

The reason for this fundamental restriction in the practical use of X-ray imaging modalities is the very limited number of contrast mechanisms that are available in the X-ray range from between $10\,\mathrm{keV}$ and a few $100\,\mathrm{keV}$, which is of primary interest to medical and NDT applications. Actually, one finds only two distinct physical attenuation mechanisms in this energy range, namely photoabsorption and Compton scattering. Each of these effects has its own characteristic energy dependence of the attenuation behavior, and it appears that these attenuation functions do not depend on the composition of the object. Therefore, it has only been possible until now to measure and depict at most two distinct physical parameters at each pixel or voxel of an X-ray or CT picture.

The basic question of the present thesis is whether there exists a (subtle) physi-

Figure 1.1.: The first X-ray image which shows the hand of Mrs. Röntgen [14].

cal effect that has not yet been exploited, which would allow the extraction of more information from X-ray attenuation measurements in the energy range of interest to medical and NDT applications.

The main result of this research work is that, indeed, such an effect exists, and it can be exploited in practice to obtain information on the elemental composition of samples. In addition, our novel approach does not require special X-ray sources (for example to produce monochromatic spectra) but it works with conventional X-ray tubes as employed today in all medical and NDT applications. Other than existing methods, our approach is capable of identifying multiple chemical elements simultaneously, and only a rather limited X-ray energy band is required for this. The simultaneous detection of aluminum, silicon, and titanium is preformed in this work and they could be detected. The method developed in this work could lead to some interesting applications which will be described in the following paragraphs.

The identification of the elements can be used, in particular, in medical imagery to increase the contrast in specific tissues. For example, cancer tissue is known to have a different elemental composition than healthy tissue – some widespread cancer types, such as breast cancer, exhibit micro-calcifications, and the identification of these calcium-rich areas is a indication of cancer [33].

Another potential application field can be functional imaging without tracers. Today tracers are used to image the spatial distribution of a specific target molecule or function. This can be done label-free if this molecule or function can be identified by a characteristic element. In the security domain the identification of elements would increase the quality in the determination of the searched materials.

This work is divided in five chapters. The subsequent chapter gives background information about the creation of X-ray photons and its interaction with mater. The third chapter describes the conventional part of the machine with a focus on tomography. This is followed by the presentation of the element sensitive X-ray measuring method with its calculation method as well as its experimental results. In the last chapter the main results of this work are summarized and conclusions are drawn.

2. Generation of X-rays and their interaction with matter

In the literature two definitions of X-rays can be found. In a first one the electromagnetic spectrum between **10 nm** and **10 pm** is defined as X-ray. This means that only the wavelength of the radiation is used as a selection criteria. In the second approach X-rays are defined by both a upper limit of **10 nm** and the creation process. In this latter definition the X-ray radiation is created by electron-based processes. Two processes create the X-ray based on electron interaction: the radiation created by decelerating electrons and the radiation emitted by the transition of an electron in the orbits of an atom.

The X-rays are situated between the ultra-violet and the γ-rays spectral regions as shown in figure 2.1. γ-rays have a shorter wavelength or are created by other processes dependent on the X-ray / γ-ray definition. The creation of γ-rays can be limited to energy transitions in the nucleus. In the neighboring range from **380 nm** to **10 nm** on the longer wavelength side the radiation is called ultra-violet.

The wavelength and the photon energy are related by the equation $\lambda = \frac{h \cdot c}{E}$ with the Planck constant $h = 6.626 \times 10^{-34}\,\mathrm{J\,s} = 4.136 \times 10^{-15}\,\mathrm{eV\,s}$ and the velocity of light $c = 299\,792\,458\,\frac{\mathrm{m}}{\mathrm{s}}$. From this equation the energy for the X-ray limits can be calculated as $10\,\mathrm{nm} \mathrel{\widehat{=}} 124\,\mathrm{eV}$ and $10\,\mathrm{pm} \mathrel{\widehat{=}} 124\,\mathrm{keV}$.

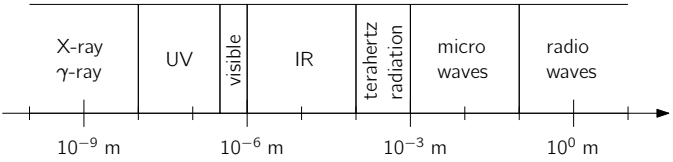

Figure 2.1.: The electro magnetic spectrum with the X-rays at the lower end of the wavelength.

2.1. X-ray generation

X-rays can be generated by two different source types

- X-ray tube (schematic in figure 2.2 and spectrum in figure 2.3)
- particle accelerator

In an X-ray vacuum tube, electrons are accelerated and directed towards a target. Inside the target the X-rays are generated by two different effects. One effect is called bremsstrahlung. It generates a continuous spectrum over a wide range of energies. The photons are emitted in an acceleration process occurring when a high energy electron is deflected by a nucleus. The other effect is discrete and dependent on the energy level of the target element. The accelerated electron can eject electrons out of their energy state inside the target material. Those vacancies will be filled by other electrons. This process will emit an X-ray photon. Because this transition have discrete energies the radiation will also be discrete.

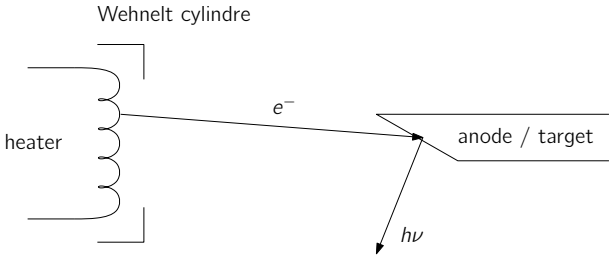

Figure 2.2.: Schematical construction of an X-ray tube. The acceleration potential is applied to the anode. The Wehnelt cylinder focuses the electrons primarily. The X-ray photons are generated by a deceleration of the electrons in the target.

The second X-ray source type are particle accelerators, especially synchrotrons. In order to generate X-rays the force exerted on the particle must be in the right range. This leads to a continuous energy spectrum. The advantage of a synchrotron is the high brilliance that it can achieve. The brilliance of an X-ray system is defined as the number of photons per second, per solid angle, per creation surface, and per 0.1 % bandwidth. The brilliance of a classical tube is up to $10^6 \frac{\#\text{photons}}{\text{s rad}^2\,\text{mm}^2\,0.1\,\%\text{b w}}$. In the

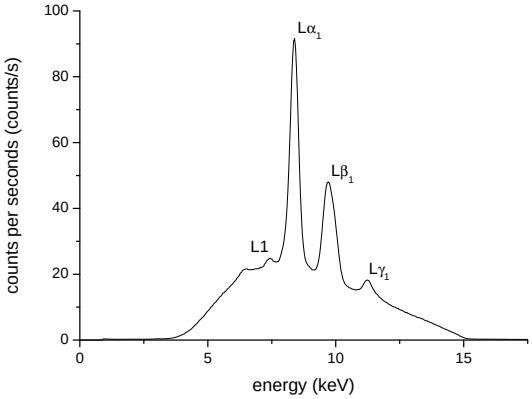

Figure 2.3.: A spectrum of the Hamamatsu microfocus source L10101 used in this work. The source is driven by 15 kV acceleration tension and 1 µA electron current. This spectrum is measured with a spectrometer from Amptek (X-123).

fourth synchrotron generation, the so called free electron laser, the maximal brilliance is $10^{34}\ \frac{\#\text{photons}}{\text{s rad}^2\,\text{mm}^2\,0.1\,\%\text{b w}}$.

2.1.1. Bremsstrahlung

The bremsstrahlung of a vacuum tube has a continuous spectrum. The Duane-Hunt law [12] describes the maximal energy. The conversion of energy is the basis of this law. The maximal energy is the energy of the electrons. In figure 2.3 such a spectrum is shown. In the figure several absorption effects take place. There is self-absorption in the target, in both beryllium windows of the source and of the spectrometer, and in the air between those two.

The range of the electrons in the target can be estimated with the equation from Kanaya and Okayama [19]

$$R = \frac{2.76 \times 10^{-10} \cdot A \cdot E_0^{\frac{5}{3}}}{\rho \cdot Z^{\frac{8}{9}}}$$

where R has the unit meter, ρ kilogram per cubic meter and E_0 electron volt. As an example the range of the electrons at 15 keV is 0.5 µm in tungsten.

2.1.2. Electron excitation

One way to excite an atom is to eject an electron of the atom by another striking electron. This striking electron is part of the electron beam directed towards the target in an X-ray tube. The vacancy created by this event will be filled by an electron of an outer shell. The energy of those transitions is discrete and dependent on the element (see figure 2.4).

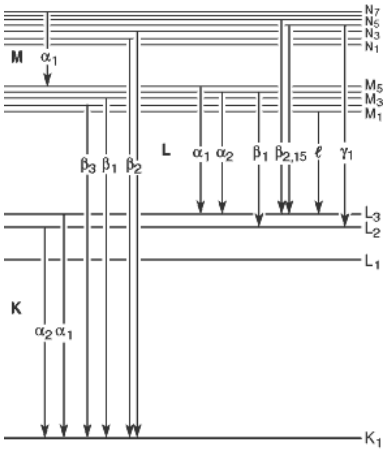

Figure 2.4.: The different transitions which give rise to the excitation peaks [35]

2.2. Interaction with matter

Five absorption effects are observed: The photoabsorption, the Compton scattering, the Rayleigh scattering, the pair production, and the photo disintegration. Each of these five effects is dominant in a specific energy range with the exception of Rayleigh scattering. This is shown with the example of silicon (Si) in figure 2.5 for low energies. At the lower end of the X-ray range the photoabsorption is the most important absorption. At higher energies, of the order of tens of keV, scattering becomes dominant. The inelastic scattering (Compton scattering) is more important than the elastic

one (Rayleigh/Thompson scattering). Above 1.02 MeV pair production becomes possible and with increasing energy also more and more important. In the pair production an electron-positron pair is created. At even higher energies photodisintegration can take place. In the photodisintegration an atom disintegrates into two daughter atoms with the energy of one photon. The three most important absorption effects in the considered X-ray range are described later and shown in figure 2.6.

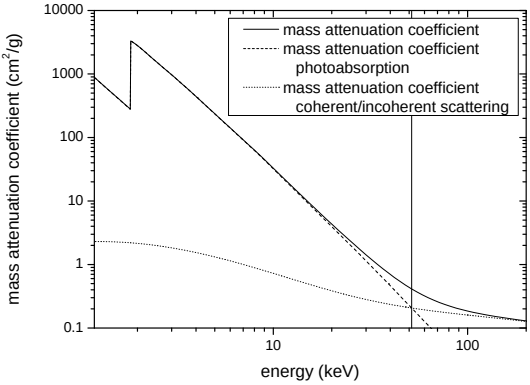

Figure 2.5.: In this energy range the absorption is the sum of two effects: the photoabsorption and the scattering. The vertical, dot-dash line indicates the point where 50 % of the absorption is photoabsorption and 50 % is scattering.

The threshold energy between photoabsorption and scattering is shown in figure 2.7. From the graph, it is clearly visible that this threshold energy increases with the atomic number.

The absorption combination of the different effects can be written as

$$\mu = \mu_p + \mu_{si} + \mu_{sc} + \mu_{pp} + \mu_{pd} \tag{2.1}$$

where μ_p is the absorption due to the photoabsorption, μ_{sc} the Compton scattering, μ_{si} the Rayleigh scattering, μ_{pp} the pair production, and μ_{pd} the photo disintegration.

The absorption within a material is characterized by the mass-absorption coefficient $\frac{\mu}{\rho}$.

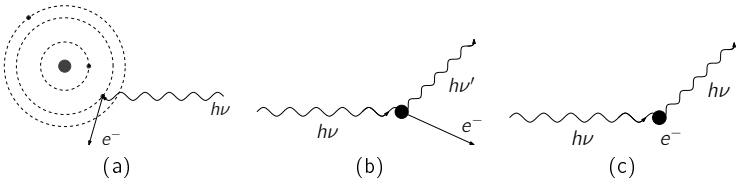

Figure 2.6.: The three different interaction types in the considered energy range. (a) photoabsorption, (b) incoherent scattering (Compton scattering), and (c) coherent scattering (Thomson/Rayleigh scattering).

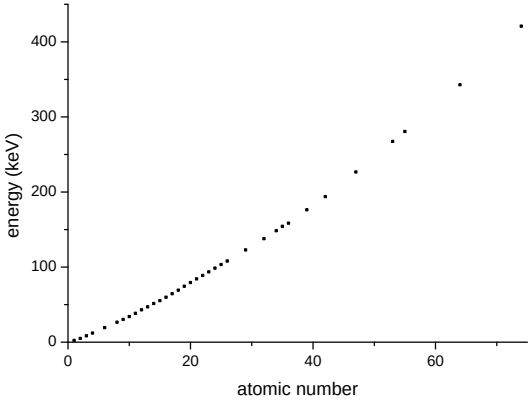

Figure 2.7.: The energy range where photoabsorption is dominant has an end point dependent on the element. This graph shows the energy where 50 % of the absorption is due to photoabsorption as a function of the atomic number.

2.2.1. Absorption Law

The intensity decay follows the Beer-Lambert law. The absorption is an exponential decay in homogeneous matter

$$I(x) = I_0 \cdot e^{-\mu \cdot x} \tag{2.2}$$

The mass-absorption coefficient $\frac{\mu}{\rho}$ is the absorption μ divided by the density ρ. The advantage of the mass-absorption coefficient is its independence on the density. Therefore the mass-absorption coefficient depends only on the X-ray photon energy for a given material and does not depend on any material parameter.

To measure the absorption a relative measurement is needed. If two measurements are made

$$\begin{aligned} I_1 &= I_0 \cdot e^{-x_1 \cdot \mu_1} \\ I_2 &= I_0 \cdot e^{-x_2 \cdot \mu_1} \end{aligned}$$

the absorption can be calculated by

$$\ln\left(\frac{I_1}{I_2}\right) = x_2 \cdot \mu_2 - x_1 \cdot \mu_1 \tag{2.3}$$

Several absorptions in sequence row are multiplicative. The case of two absorptions is shown as example

$$I_b = I_a \cdot e^{-x_b \cdot \mu_b} = I_0 \cdot e^{-x_a \cdot \mu_a} \cdot e^{-x_b \cdot \mu_b} = I_0 \cdot e^{-(x_a \cdot \mu_a + x_b \cdot \mu_b)} \tag{2.4}$$

This can be generalized for multiple objects to

$$I = I_0 \cdot e^{-\sum_i x_i \cdot \mu_i} \tag{2.5}$$

or, in case of an object varying continuously

$$I = I_0 \cdot e^{-\int_d \mu(x)\, dx}$$

where the integral is evaluated over the beam path d in the object. Those equations are also valid in the case of a compound (e.g. alloy).

In the case of additional material in the second measurement from equation (2.4), the absorption can be written as

$$x_2 \cdot \mu_2 = x_1 \cdot \mu_1 + x \cdot \mu_x$$

where x is the length of the additional material and μ_x the absorption coefficient. In this case equation (2.3) can be simplified.

$$\ln\left(\frac{I_1}{I_2}\right) = x_2 \cdot \mu_2 - x_1 \cdot \mu_1 = (x_1 \cdot \mu_1 + x \cdot \mu_x) - x_1 \cdot \mu_1 = x \cdot \mu_x \tag{2.6}$$

The two measurements can be separated in time or in space. When the measurements are separated in time, two measurements are made. Between these two measurements the object in question is either put in or taken out of the beam path. In the case of spatial separation the measurement is made with one or two dimensional detectors. Two pixels of the detector are compared. The photons collected by one pixel must traverse the object in question and the photons collected by the other pixel must traverse the same material just without the object.

2.2.2. Photoabsorption

Photoabsorption is the dominant absorption at the lower end of the X-ray energy range. In photoabsorption the incoming photons eject the bound electrons from their shells. It is customary to approximate the dependence of the mass-absorption coefficient on the atomic number and energy by the Bragg-Pierce law as

$$\frac{\mu}{\rho} \propto Z^4 \cdot E_\gamma^{-3} \tag{2.7}$$

as can be found in many textbook, see for example [6]. A more accurate equation is

$$\frac{\mu}{\rho} \propto Z^{b(E)} \cdot E_\gamma^{a(Z)} \tag{2.8}$$

2.2.2.1. Absorption edges

The electrons of an atom are organized in shells around the nucleus. Each electron is bound by a specific energy to the nucleus. These energies are similar to the electron in the same shell. The photoabsorption ejects electrons from the atom. The photon can only eject electrons with smaller bonding energy than the kinetic energy of the photon. With decreasing energy the number of potential electrons will decrease. Around the energy of a shell there will be therefore an edge in the absorption probability (see figure 2.8). If the shell is filled by multiple electrons the edge can be divided into several substeps. Those substeps are at the energy of the different electrons in the shell. From the broadening of the edge and from the exact fine structure the chemical state of the atom can be determined. The exact fine structure reveals the energy state of each electron. Thanks to this information the chemical state is derived. Those fine structures are used in X-ray absorption fine structure (XAFS) method.

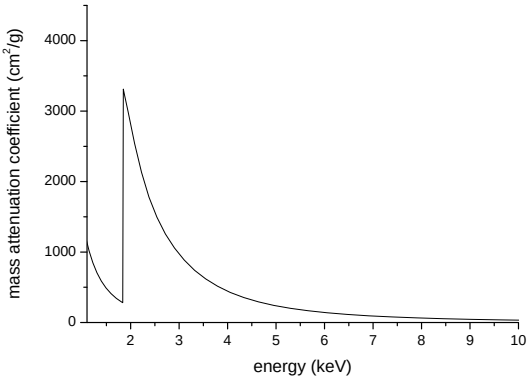

Figure 2.8.: K-edge in the photoabsorption of silicon.

These edges can be used to produce an image of one element. For this purpose two images must be produced. For the first image the energy should be slightly lower than the edge energy and the second image should have a slightly higher energy. The difference of these two images will be essentially the element responsible for the edge, as the absorption for the other elements changes much more smoothly. In air this method works for heavy elements starting from iron (Fe $K = 7.11\,\mathrm{keV}$). For elements with a smaller atomic number the measurement must be performed in vacuum as the air absorbs too much of the radiation at those energies. Vacuum condition is lethal for most biological tissues and therefore vacuum restricts the utility of such a measuring method.

An important energy range for biology is the water window. The water window separates water from organic material containing carbon. This is the range between the K-edges of oxygen $532\,\mathrm{eV}$ and carbon $283.8\,\mathrm{eV}$. As explained above this is only accessible in high vacuum.

The edge energy for hydrogen $Z = 1$ can be calculated through the Rydberg-energy which is

$$E_n = -R_y Z^2 \left(\frac{1}{n_1^2} - \frac{1}{n_2^2} \right)$$

For electrons leaving the atom completely $n_2 \to \mathrm{inf}$ will tend to infinity. In this case the equation becomes

$$E_n = -R_y \frac{Z^2}{n^2}$$

In the case of the K-edge quantum number $n_k = 1$. The energy is

$$E_k = -R_y Z^2 \sim Z^2$$

where $R_y = 13.6\,\text{eV}$ is the ionization energy for hydrogen. Even though the atomic number Z is part of the equation, this is only correct for $Z = 1$ which is hydrogen. For other hydrogen like atoms (Li, Na, K, ...) it is true for the last shell filled with just one electron. In all other cases this equation is only a rough estimation.

2.2.3. Scattering

The most important type of scattering is Compton scattering. Compton scattering is an inelastic scattering, and therefore the photon has a lower frequency after the scattering. The simplified probability of the Compton scattering is $\frac{\mu}{\rho} \sim \frac{1}{E_\gamma}$ i.e. independent of the atomic number Z (see figure 2.9).

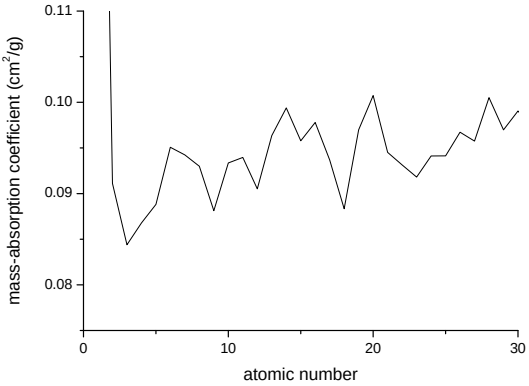

Figure 2.9.: The dependence of Compton scattering on the atomic number. The figure represents the situation at 380 keV. To the end of the scale the photoabsorption becomes more important and modifies the behavior.

The increase in wavelength is only dependent on the angle ϕ between the incident and the scattered photon direction [34]

$$\Delta\lambda = \frac{2h}{m_e c}\sin^2\frac{\phi}{2} = \frac{h}{m_e c}(1-\cos\phi) = 0.0243\,\text{Å}\cdot(1-\cos\phi)$$

where $m_e = 9.11 \times 10^{-31}\,\text{kg}$ is the mass of an electron [9]. In terms of energy the decrease is also dependent of the energy as $E \sim \frac{1}{\lambda}$. The higher the energy is, i.e. the

shorter the wavelength, the larger the fraction of the total energy of the photon will be which is transfered in the process.

The distribution of the angle ϕ is not uniform over 2π and depends on the energy. At low energy there is a significant amount of backscattered photons. At higher energies most photons are scattered only by a few degrees.

Compton scattering exhibits the following absorption equation depending on the energy of the photons. The equation was first derived by Klein-Nishina [20]

$$f_{KN} = c \cdot \left[\frac{1+\alpha}{\alpha} \left(\frac{2(1+\alpha)}{1+2\alpha} - \frac{1}{\alpha} \ln(1+2\alpha) \right) + \frac{1}{2\alpha} \ln(1+2\alpha) - \frac{1+3\alpha}{(1+2\alpha)^2} \right] \tag{2.9}$$

where $\alpha = \frac{E_\gamma}{510.975\,\mathrm{keV}}$.

In addition to Compton scattering, Rayleigh/Thompson scattering also occurs. This type of scattering is less important than the Compton scattering. The difference is the elasticity of the Rayleigh/Thompson scattering. The photon has the same energy afterwards but a different propagation direction.

2.3. Fluorescence

Fluorescence is based on the same principle as electron excitation described in section 2.1.2. In the case of electron excitation the electron is ejected by another electron. In fluorescence the ejection is due to an X-ray photon.

When an object is irradiated by X-ray photons all the excited atoms will emit fluorescence photons. These new photons will have an element specific energy lower than the energy of the primary photons. The photons are emitted isotropically into all directions (4π). Because of the absorption in the object the measured radiation outside the object comes predominantly from the surface. With this technique it is possible to identify the elements on the surface of an object. Because the photons are emitted in all directions it is not possible to image a surface in one or two dimensions without scanning the excitation radiation or using a strong collimator.

In this work the fluorescence is used to calibrate the spectrometer. Otherwise in the regular measurements fluorescence is detrimental to our experiments and should be avoided.

2.4. Optimal absorption

The fundamental noise limiting the detection of X-ray photons is shot noise. Shot noise is a result of the quantization of the radiation in photons. The photons do not arrive in a continuous manner but rather as single, independent particles with random

time spacing. The probability distribution of the arriving photons follows a Poisson distribution. The average numbers of photons N arriving in a certain time interval is proportional to the intensity $N \propto I$. Intensity is described in section 2.2.1. The shot noise σ will be dependent on the number of photons arriving $\sigma_N = \sqrt{N}$ which can be approximated for this calculation with

$$\sigma_N \approx \sqrt{N} \approx \sqrt{N_0} e^{-\frac{\mu x}{2}}$$

The signal will be

$$\Delta N = N_2 - N_1 = N_0 e^{-\mu x} \left(e^{-\mu \Delta x} - 1 \right)$$

Considering the case of $\mu \Delta x \ll 1$ the expression $e^{-\mu \Delta x} \approx 1 - \mu \Delta x$ can be simplified. The signal will become

$$\Delta N = -N_0 e^{-\mu x} \cdot \mu \cdot \Delta x$$

With these two equations the signal to noise ratio (SNR) can be calculated

$$SNR = \frac{\Delta N}{\sigma_{N_1}} = \frac{-N_0 e^{-\mu x} \cdot \mu \cdot \Delta x}{\sqrt{N_0} e^{-\frac{\mu x}{2}}} = -\sqrt{N_0} e^{-\frac{\mu x}{2}} \cdot \mu \cdot \Delta x$$

To minimize the SNR the derivative has to be zero.

$$\frac{\partial SNR}{\partial \mu} = -\sqrt{N_0} \cdot \Delta x \cdot e^{-\frac{\mu x}{2}} \left(1 - \mu \frac{x}{2} \right)$$

The only root of this equation interesting for this problem is

$$1 - \frac{\mu x}{2} = 0$$

This gives a result which is independent of the signal Δx but dependent on the absolute absorption.

$$\begin{aligned} \mu x &= 2 \\ e^{-2} &= 0.135 \end{aligned}$$

Now two approaches are possible. The energy can be fixed and an optimal thickness of the object can be calculated (see figure 2.10). The second possibility is to fix the object and its absorption and then calculate the optimal energy.

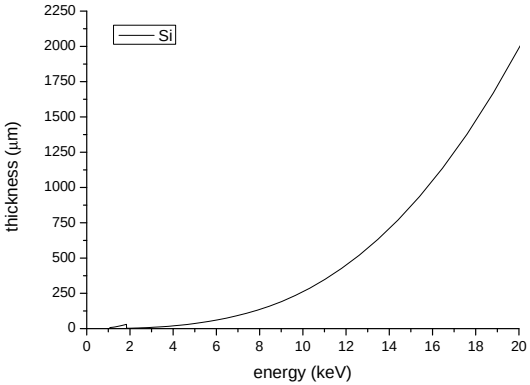

Figure 2.10.: The shot noise will be minimized when **13.5 %** of the radiation is transmitted. This combines an energy and an object thickness for an optimal measurement.

3. Conventional X-ray micro-radiography and micro-CT

The X-ray setup which was built especially for this work is versatile and can be either used for conventional absorption X-ray imaging of for element-sensitive X-ray measurements. In this chapter, the conventional X-ray imaging part is described.

The setup can be used to generate two dimensional micro-radiography images. In addition, the setup can also be used as a micro-computed-tomograph (microCT). This chapter contains a description of the setup, the imaging process, and the generation of two and three dimensional tomographical images.

The instrument is controlled by a computer program written in C# and partly in C++.

3.1. Experimental setup

The setup (shown in figure 3.2) consist of three main parts for the imaging and the mechanical requirements. Additionally, a shielding made of lead and steel, is necessary to protect the user from the ionizing radiation. The three parts of the setup (see figure 3.1) are

- the Hamamatsu microfocus X-ray source,
- the rotation stage with a sample holder,
- the X-ray camera

The source, the rotation stage, and the camera are positioned on a line. This optical axis is illustrated by a dashed line in the figure. The source and the camera are mounted on rails and can be moved along this axis. The relative distances control the magnification which is

$$M = \frac{b}{a} \tag{3.1}$$

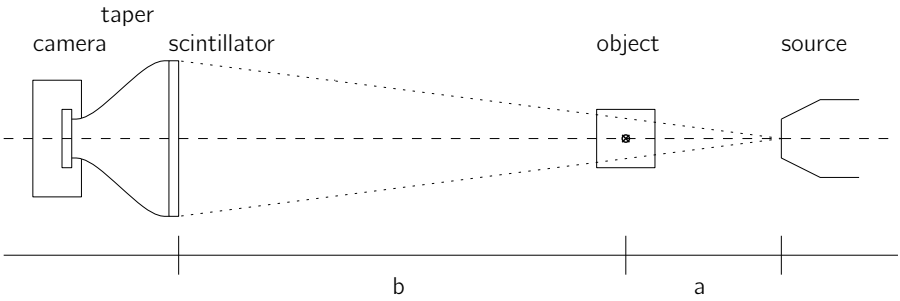

Figure 3.1.: Schematic representation of the setup. The dashed line is the optical axis. The distances a and b are determining the magnification of the X-ray images. The object is on a rotation stage and its rotation axis is indicated by a crossed circle.

where a is the distance source - object and b the distance object - detector as indicated in the figure. The distances a and b are to some extent variable. The limits of these distances are on one hand fixed by the external case's dimension and on the other hand by the internal shielding. Some combinations of a and b are impossible because of the internal shielding. The limits for a, b, and M are presented in table 3.1. Additionally the photon flux reaching the detector is dependent on $a+b$, the total distance source - camera, because this distance fixes the solid angle of the collected photons on the detector area.

parameter	minimal	maximal
a	12 mm	60 mm
b	300 mm	485 mm
M	5	40
FOV width	0.12 mm	9.5 mm
FOV height	0.09 mm	7.1 mm

Table 3.1.: The range for the different parameters is shown. The two distances a and b are indicated in figure 3.1. The range of the magnification M is described in equation (3.1). This magnification leads to the listed possible dimensions of the field of view (FOV).

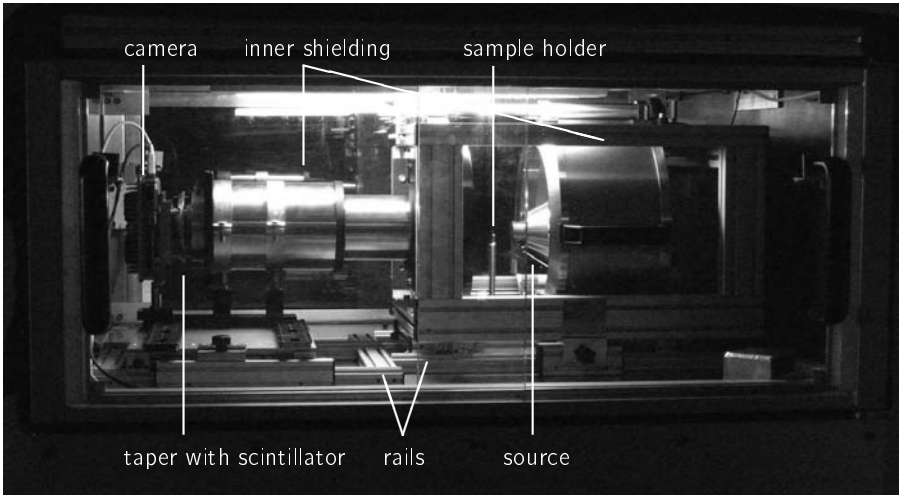

Figure 3.2.: The setup with the X-ray source, a sample, and the camera. Two layers of shielding protect from the radiation. The instruments and one layer of shielding is mounted on a rail system to adjust the magnification.

The shielding is about **6 mm** of lead or an equivalent of steel in all directions. If lead is replaced by steel the thickness must be **6.5** times thicker [11]. This thickness is divided into a inner and an outer shielding. With this combination and its overlap the shielding quality is insured. All doors of the shielding are secured. If one of these doors opens the source shuts down immediately. Outside the instrument the radiation level is below $0.2\,\frac{\mu Sv}{h}$. With this radiation level all operators are sufficiently protected against the radiation and no additional protection measure must be taken. For monitoring of the radiation level outside the shielding a radiation meter from Thermo Fisher Scientific (900 Ratemeter with Type 42B Probe) is used. This probe has a sodium iodide (NaI) scintillator with **1 mm** thickness and a **0.25 µm** beryllium window. The radiation meter is shown in figure 3.3.

Figure 3.3.: For the measurement of the radiation level outside of the shielding a ratemeter from Thermo is used.

The resolution of the system at the maximal magnification is about **10 µm**. One example of this resolution is shown in figure 3.4, which shows a glass sample with platinum electrodes. The platinum track has a width of **11 µm**. In figure 3.5 an image of the edge from a **5 µm** platinum sheet is analyzed. This analysis is compared with a modulation transfer function (MTF), which gives the contrast dependent on the periodicity of the structures and is shown in figure 3.6. The MTF is a standard characterization of a optical system's resolution. An example for an X-ray system can be found in [27]. It is defined as the Fourier transformation of the point spread function of the system. To compare the diagram 3.5b with an MTF the step percentage must be halved because the diagram is from a step and not from a grating. This is shown with a simplified example in figure 3.7. This division by two is due to the fact that the step has a predecessor and a successor. Both decrease the contrast of the signal.

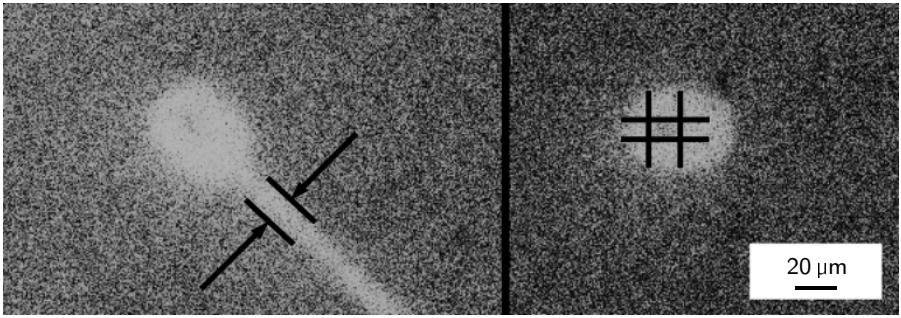

Figure 3.4.: The resolution in the 2D images is about **10 µm**. On this image a platinum track with the width of **11 µm** is visible. The two electrodes have a hole in the platinum of the size of **11 µm** × **7.5 µm**.

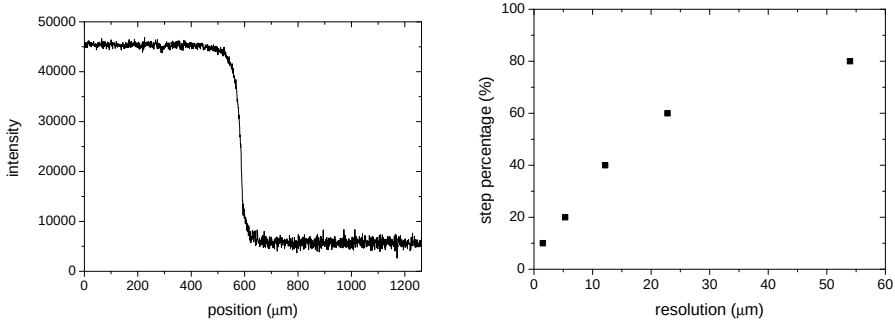

(a) step (b) resolution

Figure 3.5.: In graph (a) is a edge of **5 µm** platinum sheet under **40 kV** acceleration voltage. This line is analyzed in graph (b) to calculate the resolution for a part of the step.

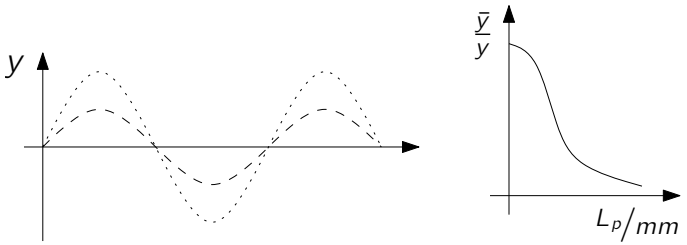

(a) signal (b) ratio

Figure 3.6.: The modulation transfer function (MTF) is the ratio of the input (y; dotted) versus output ($\bar{y}$; dashed) amplitude of a sinusoidal signal over a range of frequencies in line per millimeter L_p/mm.

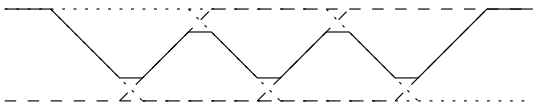

Figure 3.7.: From a series of steps a grating can be constructed. The dotted lines are the falling edge and the dashed line the rising edge of a step. The normal line is the simplified signal.

3.1.1. Source

The X-ray source is a commercial available microfocus X-ray source from Hamamatsu (L10101) [15] (see figure 3.8). The source is sealed and therefore the vacuum is stable and no maintenance is needed. The maximal acceleration voltage is 100 kV. The current that passes through the filament is between 0 µA to 200 µA. Below 40 kV acceleration voltage the maximal current is dependent on the voltage. Below 20 kV the maximal current is not specified (see figure 3.9b). The maximal electron power is therefore 20 W. The spot size is dependent on the electron power. Up to 4 W the diameter is 5 µm while for higher power the spot size increases linearly (see figure 3.9a). The electron target is made out of tungsten. The distance between the focal spot and the beryllium window is 6.8 mm. This distance determines the minimal distance of the focal spot to the object and therefore affects strongly the maximal possible magnification. This is due to the fact that the magnification is the ratio between the object to detector distance and the focal spot to object distance as indicated in equation (3.1).

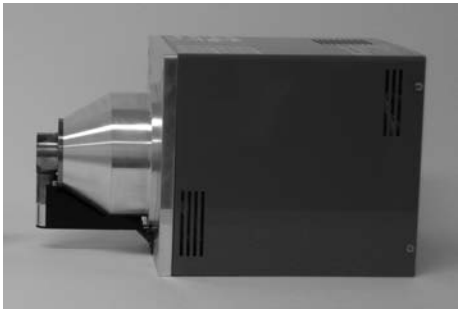

Figure 3.8.: The Hamamatsu L10101 source with a minimal focal spot diameter of 5 µm.

The beryllium windows has to seal the vacuum in the source. The downside is that all material, including for example beryllium, in the beam path will absorb part of the radiation. As the low energy photons are more strongly absorbed than the high energy ones, the spectral distribution is shifted towards higher energies (beam hardening). As introduced in section 2.2.2 in the range of a few keV this effect is strong. The thickness of the window must be minimized, in this source 150 µm, in order to minimize the hardening.

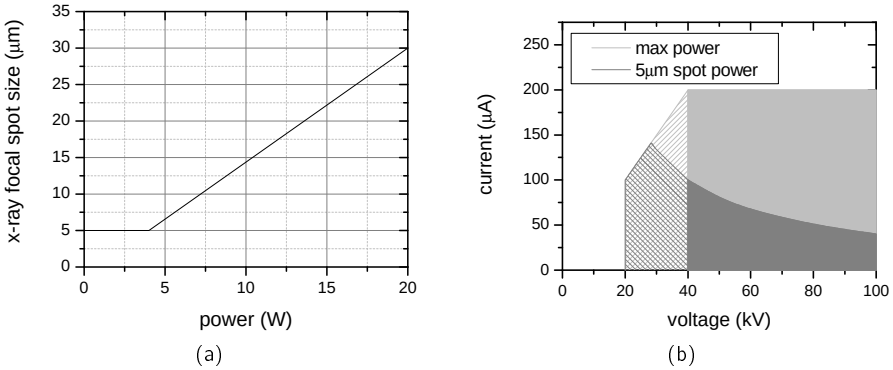

Figure 3.9.: Diagram (a) shows the X-ray focal spot size versus the electron power. In (b) the maximal power is shown as a function of the current and of the voltage. Below 20 kV no information is given and up to 40 kV the function is not specified.

3.1.2. Camera

The X-ray camera is a commercially available astronomical low-noise charge-coupled device (CCD) camera Alta U2000 from Apogee [4] (see figure 3.10).The noise levels are for dark current $0.1\,\frac{e^-\,s}{px}$ at $-30\,°C$ and for the electronic read-out noise $8\,e^-$ RMS. On top of the CCD an optical taper from Incom is fixed. On this taper a scintillator is glued. The scintillator is a cesium iodide (CsI) crystal doped with thallium (Tl) with a thickness of 150 µm manufactured by Hilger Crystals (see figure 3.11). The thallium is needed to shift the wavelength of the maximal emission to 550 nm where the quantum efficiency of a silicon CCD is near to maximum. In figure 3.12 the absorption characteristic of the CsI scintillator is shown. The taper reduces the image size by a factor of 4. This reduction is needed as the scintillator has a coarser resolution than the CCD. Even with this reduction the resolution difference cannot be entirely compensated.

The CCD in the camera is cooled down to reduce the dark current. In the specifications of the camera 50 °C below ambient is guaranteed. Because of the adaptations carried out to the camera the temperature can be kept only at 35 °C below ambient. The chamber of the CCD is still sealed but additional losses exist now through temperature dissipation over the taper. The chamber is shown in figure 3.13.

The taper is too heavy to be glued directly onto the CCD. Therefore an additional mechanical construction fixes the taper on the camera. Due to this indirect fixation

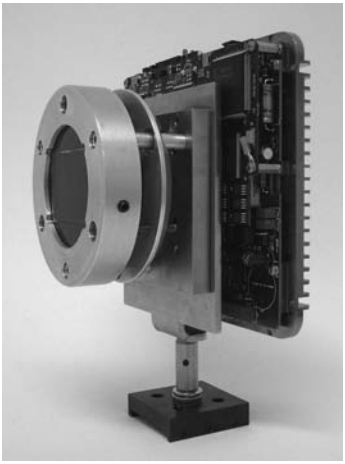

Figure 3.10.: The Apogee Alta U2000 with taper and scintillator (CsI:Tl). After the changes on the camera, the CCD can be cooled down to 35 °C below ambient temperature.

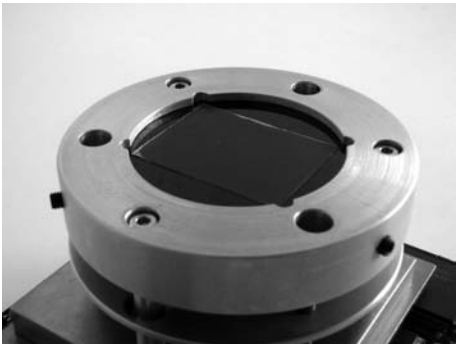

Figure 3.11.: Detail view of the scintillator (CsI:Tl) on top of the taper.

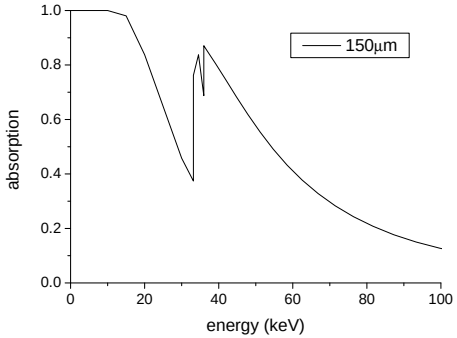

Figure 3.12.: The absorption characteristic for **150 µm** CsI as the scintillator is fixed on the camera.

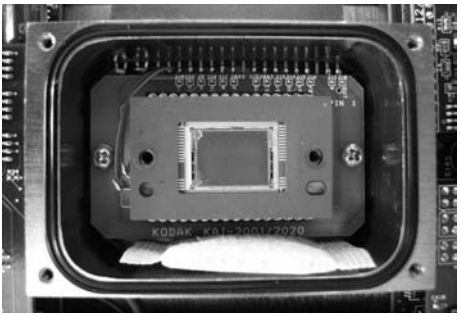

Figure 3.13.: The cooling chamber of the CCD which is sealed in operation. On the bottom there is a desiccant bag to inhibit the creation of condensed water/ice.

relative to the CCD an additional procedure is needed to make sure that the taper and the CCD will be parallel. The parallelism is achieved by a liquid drop (shown in figure 3.15). The distance taper-CCD is controlled with three screws. If the drop grows but does not move it means that the taper is approached parallel to the CCD by tightening those screws. Additionally the distance between the taper and the CCD is controlled by the volume of the liquid drop. This distance is not accessible directly because the CCD chamber is sealed. A sketch of the construction is presented in figure 3.14.

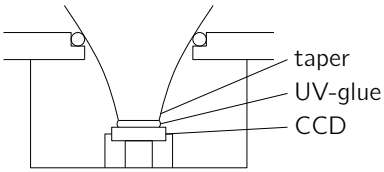

Figure 3.14.: The taper is glued on the CCD with a UV adhesive. The adhesive drop was additionally used in order to control the distance and the parallelism.

Another reason to fill the space between the CCD and taper with a liquid is the refractive index of both of them. The refractive index of the space should be matched to the silicon nitride **2.05** on the CCD chip and the taper **1.85** [17]. The effect of this index matching is shown in figure 3.16. First a high refractive index oil $n_D = 1.70$ from Cargille Labs was used. This oil had a too large volumetric thermal expansion coefficient. Because of the strong volume variations the oil could not fill the volume between the CCD and the taper at $-15\,°C$. This is the minimal temperature the thermoelectrical elements can still reach.

To overcome the volumetric thermal expansion an ultra-violet glue (Norland Optical Adhesive 61 [24]) was used afterwards. The performance was reduced with respect to the refractive index (**1.56**) but once solidified the volume of the glue remains almost unchanged. The taper was completely mounted and the cooling chamber sealed. Afterwards the glue was cured with ultra-violet light from LEDs. This light was directed through the taper. The additional absorption of ultra-violet light in the taper was taken into account for the curing.

The active surface of the CCD and the small surface of the taper have an area of $12\,mm \times 9\,mm \approx 100\,mm^2$. A glue volume of $1\,\mu l$ over the whole area will give a distance of about $10\,\mu m$. In the case of NOA 61, the volume was $4\,\mu l$. The actual distance between the CCD and the taper should be $40\,\mu m$. The mechanical limit in

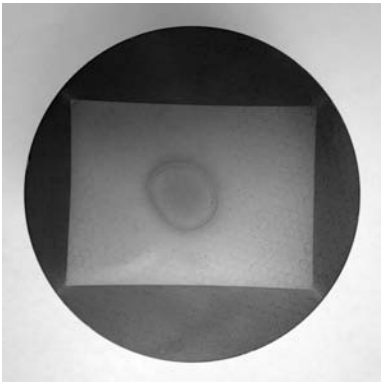

Figure 3.15.: With the help of a liquid drop the taper and the CCD could be approached in parallel manner.

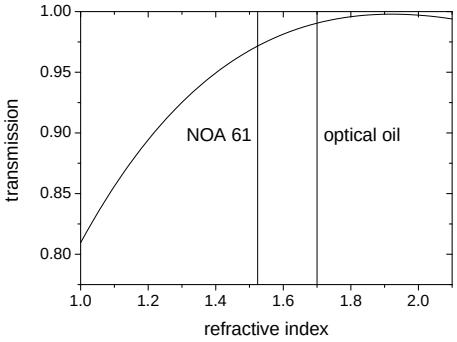

Figure 3.16.: Transmission with two interfaces in a three layers system with a variable refractive index in the middle. The first layer consistes of a glass taper ($n_g = 1.85$), the third one of the silicon nitride ($n_n = 2.05$) of the CCD chip. Two values for the refractive index are indicated (NOA 61 and optical oil). For simplicity normal incidence is considered.

adjusting this distance is in the order of a few micro meters. This adjustment is done with M4 screws with a pitch of **700 µm**. A rotation of about **1°** corresponds in this case to a height variation of about **2 µm**.

The CCD is an interline image sensor with 1600 times 1200 pixel from Kodak (KAI-2020 [13]). The pixel spacing is in both directions **7.4 µm**. Vertically the whole distance is taken by the photo-active cell. In the horizontal direction only a part of the spacing is photoactive. Between two pixels in an interline CCD there are the charge transport structure. The fill factor of this CCD is around **20 %**. This CCD is available with microlenses on top of it. These microlenses focalize the light on the photosensitive part of a pixel. Those microlenses are designed for an interface with air. Because UV-glue is used on top of the CCD in this work, the microlenses would not have the desired effect. Therefore the image sensor version without microlenses is used.

The scintillator is not very homogeneous. The effects of the inhomogeneities can be compensated with a correction algorithm. The pictures are corrected by two images. One is taken under the exact same conditions only without the sample and the second one is taken without X-ray irradiation. The equation used in this case is

$$p_{\text{corr}} = \frac{p_{\text{img}} - p_{\text{black}}}{p_{\text{white}} - p_{\text{black}}}$$

In the case of a tomography a logarithm of the division is taken.

The algorithm is extended to support different exposure times but the result may be wrong especially for the black image as the black current is not linear with the exposure time. The most important part of the value of each pixel is an offset from the analog to digital converter and not the time dependent dark current. This is also true for exposure times up to **100 s**. Corrections with only one of these two images are also possible. In this case only the division or the subtraction is performed.

After this correction some inhomogeneities are still in the image. This has two sources: first the image can be locally saturated and second the system is not strictly linear. In particular the CCD is slightly non-linear. The first effect can be identified by a saturation detection and therefore this region can be marked as special.

Before working with a CsI:Tl scintillator, a cerium doped yttrium aluminum garnet (YAG:Ce; $Y_3Al_5O_{12}$) scintillator from Crytur Ltd. was used (see figure 3.17). This scintillator has the same wavelength of the maximal emission as CsI:Tl which is at **550 nm** [23]. Its conversion capacity is lower but the scintillator had a much better homogeneity. The homogeneity is compared in the figures 3.18 and 3.19.

The image in figure 3.19 is made with a different setup (see figure 3.20). This setup has the disadvantage of losing a lot of light. Only a small percentage of the light generated in the scintillator can be collected by the object and is focused to the CCD. The rest of the light which is emitted over 4π is lost. To protect the camera from the direct irradiation with X-rays a mirror is inserted in the setup. In addition the camera is

Figure 3.17.: A free standing scintillator based on yttrium aluminum garnet (YAG) doped with cerium. The thickness is 300 µm.

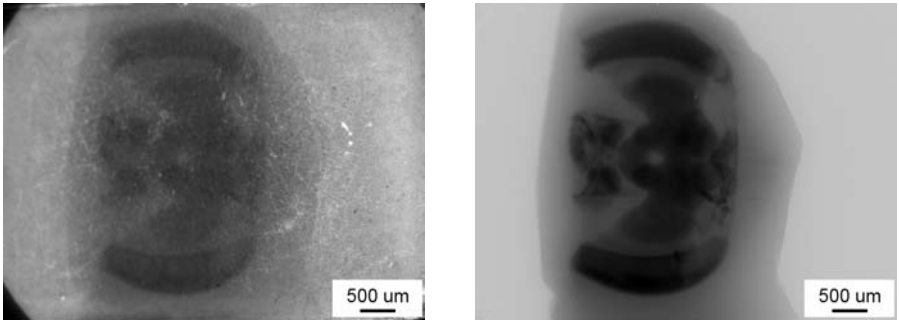

(a) without correction (b) with correction

Figure 3.18.: The homogeneity of the CsI:Tl scintillator crystal is not good enough to use the image directly. The image quality can be increased significantly with a correction by a white image. This is demonstrated with the radiography image of the brain of a bee.

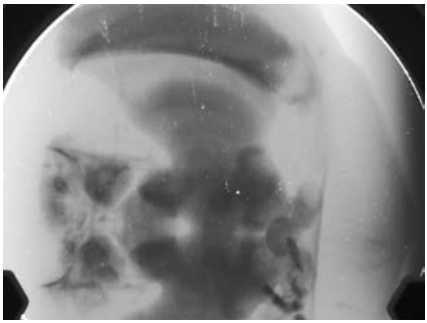

Figure 3.19.: The YAG:Ce scintillator crystal is homogeneous enough that uncorrected images can used directly. The image was taken with the setup presented in figure 3.20.

further protected by an additional shielding between the camera and the X-ray source. The taper shields the camera from X-ray beam not absorbed in the scintillator in the other setup.

The taper setup was finally selected because of its better efficiency compared to the setup in figure 3.20. The selection of CsI:Tl over YAG:Ce is due to the the thinner thickness available and therefore the better geometrical resolution.

3.1.3. Rotation stage

The motor of the rotation stage is outside the X-ray shielding. It is a stepper motor from Systec with a gear box. The rotation axis crosses the shielding and so this axis is the fixed point of the setup. The rotation stage has **48 000** steps per rotation and therefore a step angle of **0.0075°**.

The sample holder is mounted on the rotation stage. On the axis of the gear there is a connector with a thread as shown in figure 3.22. The sample can be fixed on a threaded rod which then can be screwed in the thread of the connector (see figure 3.21). The threaded rod is made out of brass, an alloy built by **63 %** copper and **37 %** zinc. This material was selected because heavier elements are less fluorescent. The fluorescence peaks are also below the analyzed energy range described in the next chapter. The fluorescence peak with the highest energy for copper is $K\beta_{1,3} = 8.9053\,\text{keV}$ and for zinc $K\beta_{1,3} = 9.5720\,\text{keV}$.

As the rod is screwed in the connector, the height can be adjusted. One rotation will change the height of one pitch. For the selected thread size M10 the pitch is **1.5 mm**.

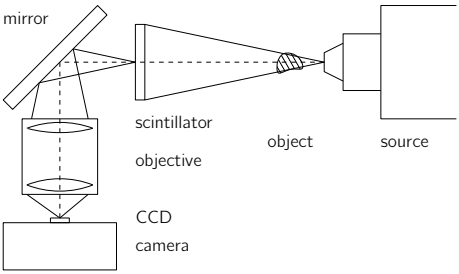

Figure 3.20.: The scintillator can also be a free standing crystal. This crystal can be imaged with an objective on a CCD. The mirror is used to protect the camera from the direct radiation of the X-ray source.

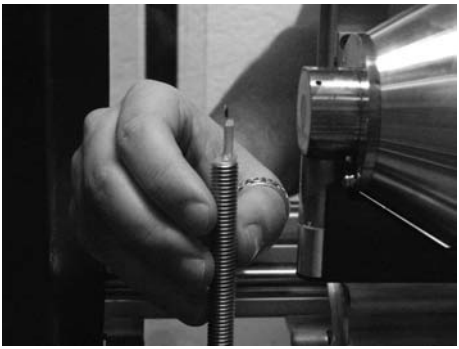

Figure 3.21.: Sample holder with a sample of a bee brain in front of the X-ray source.

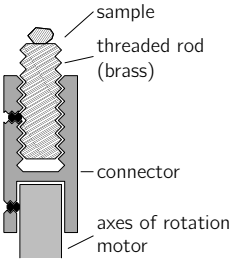

Figure 3.22.: Schematic of the sample holder. As the sample is fixed on top of a threaded rod the height can be adjusted.

3.1.4. Magnification

The magnification of an image is calculated indirectly. Under the same mechanical constrains as a corresponding image a cylindrical metal bar (see figure 3.23a) is imaged. Generally two types of bars are used. One has a diameter of **1.5 mm** and the other is for higher magnification and has a diameter of **500 µm**. The positions of the strongest differential change are searched to determine the diameter of the bars. This is done by using a band-pass filter. The high-pass component is to detect the differential change and the low-pass component in order to increase the stability of the algorithm as it filters the noise. After the filter the algorithm must just search the maximum and the minimum. Because the bars are cylindric the diameter is independent of the actual imaging direction and therefore no alignment is needed. Knowing the diameter of the bar, it is possible to calculated the size of one pixel in the image. With this information it is possible to know the scale of the other objects. Figure 3.23b is a typical X-ray image of such a bar. In this system typical magnifications of the sample on the scintillator range from 6 to 50, resulting in a pixel size in the sample between **4.6 µm** and **0.6 µm**. With the CTControl program a scale can be inserted on the bottom of a image based on this procedure.

3.1.5. Photon conversion

The photon flux for one pixel of the camera is measured indirectly by the spectrometer described in the chapter 4. Several corrections had been made from the spectral count rate. The absorption capability of **680 µm** silicon must be taken into account as well as the absorption by the **25 µm** beryllium window. Additionally the spectrum was corrected for the double events. Double events (also called dead-time effect) means that two or more photons are arriving within a time interval that is too small for the spectrometer

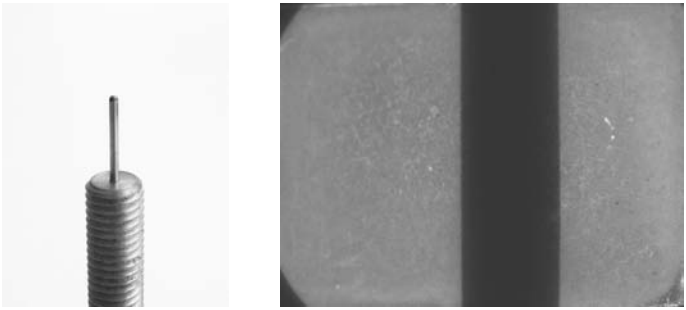

(a) (b)

Figure 3.23.: The cylinder shown in the part (a) is imaged under the same geometric conditions as the images (b). From the width of the bar the size of a pixel in the object can be determined. Here in the example the bar has a width of 392 px (1.5 mm) and therefore one pixel has a size of 3.8 µm.

to separate them. Those steps are visualized in figure 3.24. The last correction was made for the different solid angles. Those two solid angles are dependent on the distance between the source and the detector and are specific to this calculation. The spectrometer has a solid angle of

$$\Omega_{\text{spec}} = \frac{5\,\text{mm}^2}{(0.465\,\text{m})^2} = 23.1\,\text{msr}$$

In the case of the camera the solid angle is

$$\Omega_{\text{CCD}} = \frac{0.2 \cdot 16 \cdot (7.4\,\mu\text{m})^2}{(0.505\,\text{m})^2} = 0.7\,\text{nsr}$$

The factor $f_c = 0.2$ is the fill factor of the CCD in the camera.

From these two solid angles a correction factor

$$c_s = \frac{\Omega_{\text{CCD}}}{\Omega_{\text{spec}}} = 3.0 \times 10^{-8}$$

can be calculated. The result of this calculation is a flux of $0.21\,\frac{\text{h}\nu}{\text{As}}$ with a mean energy at 25.3 keV. The mean energy is calculated by the weighted arithmetic average

$$a_e = \frac{\sum_i s(E_i) \cdot E_i}{\sum_i E_i}$$

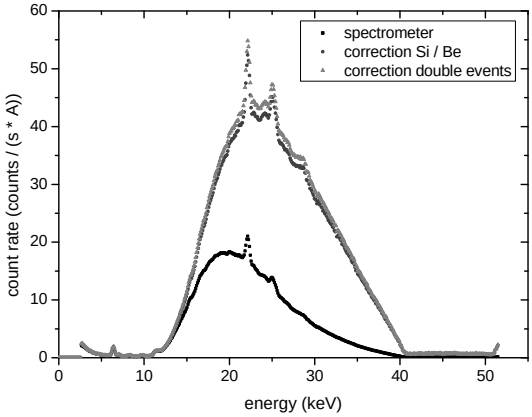

Figure 3.24.: The spectrometer cannot measure the whole flux. The losses from the finite diode thickness and from the beryllium window as well as the correction for double events are taken into account.

The current of the photo-electrons in one pixel can be calculated from the error on the signal. For this calculation nine pixels in the center of the camera are selected. Each time ten exposures are made for four tube currents (25 µA, 50 µA, 100 µA, and 200 µA) at a tube voltage of 40 kV. From those ten exposures the average and the standard deviation

$$\sigma = \sqrt{\frac{1}{N-1}\sum_{i=1}^{N}\left(S_i - \bar{S}\right)^2}$$

are determined.

For the photo-electron counts F_e, the shot noise is

$$\sigma_{F_e} = \sqrt{F_e}$$

The digital signal $D = K \cdot F_e$ is linear with respect to the photo-electron counts. In that case the conversion factor K has a negligible error. Therefore the relative error for D is

$$\frac{\sigma_D}{D} = K \cdot \frac{\sigma_{F_e}}{F_e}$$

Form this equation the error in the digital signal depends on the photo-electron counts as

$$\sigma_D = K^2 \cdot \sigma_{F_e} = K^2 \cdot \sqrt{F_e}$$

In the diagram 3.25 the y-axis is σ_D and the x-axis D with the equation

$$y = \sqrt{K^4 \cdot F_e} = \sqrt{K^3 \cdot D} = K^{\frac{3}{2}} \cdot \sqrt{x}$$

From a fit in this diagram the value for K is of $1.14\,\frac{\text{bit}}{\text{h}\nu}$ in this case. The flux of the photo-electron can be calculated on this knowledge and at the current of $100\,\mu\text{A}$.

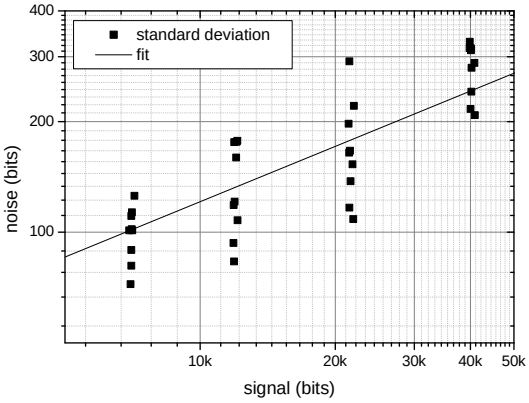

Figure 3.25.: The photon transfer curve of this system generated with an exposure time of $10\,\text{s}$ and four different currents.

The tube current of $100\,\mu\text{A}$ is the maximal current at $40\,\text{kV}$ tube voltage to keep the focal size at $5\,\mu\text{m}$. From the spectrometrical measurement the flux at the position of the scintillator is $21\,\frac{\text{h}\nu}{\text{s}}$ generating 1900 photo-electrons per second in the CCD. The X-ray photon flux converted by $100\,\%$ into visible photons of $550\,\mu\text{m}$ would give a flux of $2.4 \times 10^5\,\frac{\text{h}\nu}{\text{s}}$.

3.2. Tomography

In this section the principles and algorithms for the creation of a tomographical model are presented. The tomography is calculated by a filtered backprojection [25]. The maximal volume of a sample to be imaged tomographically is given by the field of view at the minimal magnification. The maximal volume has the dimensions of $9.5\,\text{mm} \times 9.5\,\text{mm} \times 7.1\,\text{mm}$.

Two images are presented to illustrate the capability of the X-ray tomography. In figure 3.26 a tomographic reconstruction of the brain of a female worker bee is shown. The different brain areas are visible.

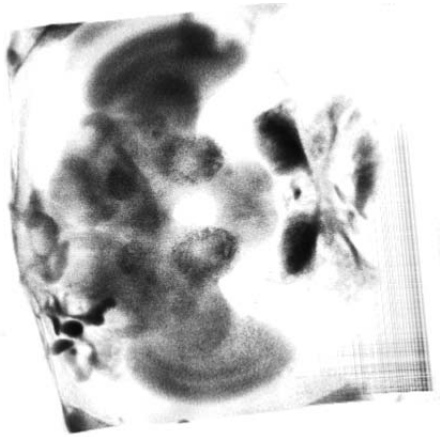

Figure 3.26.: Perspective view of a tomographic image of the brain of a female worker bee.

In the second figure 3.27 a tomographic image of a filled tube is made. The tube is filled with an artificial material used to model thrombosis in a blood vessel. An opaque black polyurethane tube with an outer diameter of **6 mm** was used. For the three dimensional reconstruction, 200 projections were made over **180°**. Each of those projections required an exposure time of **20 s**, resulting in a total imaging time of slightly more than **1 h**. The image volume is **7.2 mm** × **7.2 mm** × **5.4 mm** (400 × 400 × 300 voxels[1]) with a voxel size of **18 µm** in all three directions and a sample magnification of **6.5** times. The source acceleration voltage was **20 kV**$_p$, yielding highest intensity at the $L\alpha_1$ tungsten peak (**8.4 keV**). At this energy, the transmission through the sample was **16 %**, i.e., close to the value of **13.5 %** where shot noise is minimized (see section 2.4).

The computer calculates the reconstruction algorithm with 200 projections in **1.9 min** if no high-pass filtering to the projections is applied. With an additional high-pass

[1] A voxel stands for volumetric pixel and is a volume element in a three dimensional space.

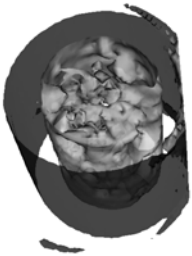

(a)

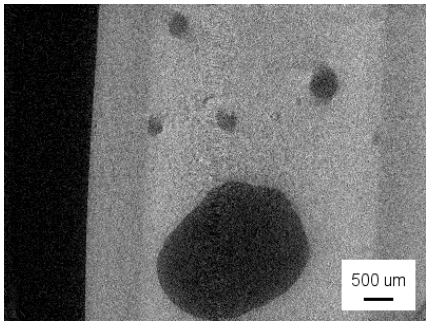

(b)

Figure 3.27.: A tomographic image (a) of a tube filled with an artificial material used to model thrombosis. In (b) a cut in the x-z plane.

filtering employing a convolution in real space the reconstruction time becomes **53 min**. This reconstruction is made on a dual core PC with **2.4 GHz** and **2 GB** RAM. The reconstruction time could be significantly decreased with a convolution in frequency space using a fast Fourier transformation (FFT) instead of a convolution in real space.

3.2.1. Projections

The numbers of projections p is determined by the resolution selected in the image space. This number is estimated by the equation

$$p = \frac{\max(v_x, v_y)}{2}$$

where v_x is the number of voxels on the x axis and v_y on the y axis. The x-y-plane is perpendicular to the rotation axis. The projection should be equiangular over a half revolution of the rotation axis.

An X-ray projection in one dimension is characterized by

$$p(t,\theta) = \int_{-\infty}^{\infty}\int_{-\infty}^{\infty} f(x,y)\ \delta(x\cos\theta + y\sin\theta - t)\ dx\ dy$$

t is the position in the rotated space of the projection. p is the projection function for an angle θ. f is the function of the sample in the x-y space. Such a projection is shown in figure 3.28.

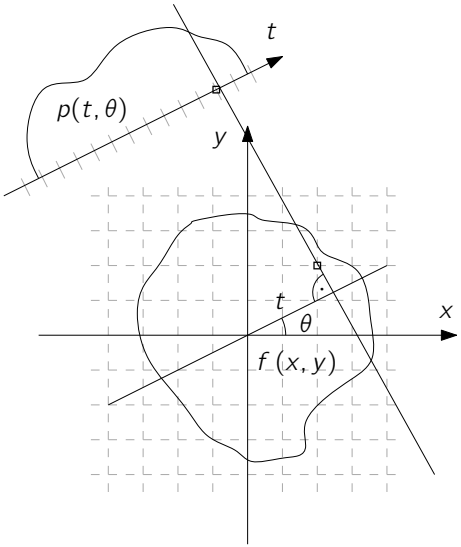

Figure 3.28.: The projection $p(t, \theta)$ of the probe $f(x, y)$ where θ is the projection angle relative to the x,y coordinates. t is the coordinate of the projection defined by time the distance of the beam to the origin in x-y. The gray grid is for the subsequent backprojection.

3.2.2. Algorithms

For the calculation of the tomographic cross section image a filtered backprojection is used. The filter applied to the data is a Shepp-Logan filter [32]. The convolution kernel of this filter is

$$f(x) = -\frac{1}{4 \cdot x^2 - 1}$$

The function is plotted in figure 3.29. In a two dimensional image the convolution kernel becomes

$$f(r) = -\frac{1}{4 \cdot r^2 - 1}$$

where r is the polar coordinate in the kernel space. The origin is in the middle of the kernel space. The convolution can be calculated in the real space or in the frequency domain. In frequency domain two additional Fourier transformations are necessary but the convolution becomes a multiplication with the kernel

$$F(\omega) = -\left|2\sin\left(\frac{\omega}{2}\right)\right| \left(\frac{\sin\left(\frac{\omega}{2}\right)}{\frac{\omega}{2}}\right)^2$$

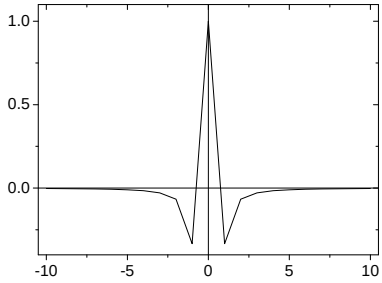

Figure 3.29.: The convolution kernel from Shepp-Logan for the filter backprojection.

The backprojection algorithm can be used for two or three dimensional reconstruction. In the two dimensional case the beams have the form of a fan. In an approximation these beams can also be treated as parallel. The same is true for three dimensional

reconstruction where the cone beam radiation can also be approximated by a parallel approach. In the parallel beam approach in three dimension all the x-y planes are treated independently.

The projected image will be upsampled to have an eight times higher resolution as the image space. The upsampling is done by a linear interpolation. If a convolution is preformed the spatial frequency in the projected image must be limited to the possible spatial frequencies in the image space. Both upsampling and the convolution are done only one dimensionally.

The actual backprojection is done by the following procedure. Each point in the image space is projected in the detector space for each angle. In the detector space the nearest point is selected. The value of this point is added to the value of the point in the image space. In figure 3.28 those two points are the squared points on the gray grid.

This procedure generates a tomographical image of the irradiated objects.

3.2.2.1. Rotation axis in projection image

The whole imaging setup is not stable enough to fix the projected rotation axis in the middle or at another fixed position in the projection image. From two projections with a relative angle of a half rotation the virtual axis can be found. One of the projections must be flipped horizontally in the middle to compensate the half revolution. A correlation of these two projections should have the maximum at the position of the rotation axis. To increase the quality of this correlation the projection can be filtered. In this work a high pass filter was temporarily used but the results were not convincing on random pictures and too strong optimized for the bars measurements described in section 3.1.4. In general in this work good results are achieved when one of the metal bars is used for the search of the virtual rotation axis.

The mechanical setup is stable enough so the virtual rotation axis is unchanged when the sample is rotated. But still the system has two types of translation of the rotation axis. The first is a shift in the x-direction. The second type is a tilt of the axis. This tilt can have the origin in a tilt of the real rotation axis or of the camera. The shift is the stronger effect and highly dependent of the actual setup. As the rotation axis of the system is not fixed relatively to the rails of the source and detector. If the rotation axis is additionally not in the middle of the rails even a change of the position of the detector or source will have an effect on the shift. To reconstruct a useful tomographic image the rotation axis must be positioned mechanically in the middle of the detector before the start.

The tilt has a range of 0.5° to 1°. To detect the tilt the analysis of several lines in the image is necessary. With the detection of the two squared points in figure 3.30 the angle α and the position can be detected. The rotation axis can be described with the

equation

$$\text{shift} = a_1 + a_2 \cdot \text{line}$$

a_1 is the position at line zero and a_2 is the slope and indirect the angle α. In this work only the simplified case with an vertical rotation axis is considered.

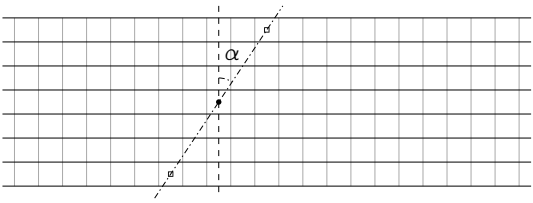

Figure 3.30.: In this work the rotation axis in the projection is simplified to a vertical line (dashed line). In reality the rotation axis has a small angle α (dash dotted line).

4. Element-sensitive X-ray absorptiometry

X-ray imaging techniques have revolutionized medical diagnostics. Whether three dimensional imaging modalities are employed, as in radiography, or three dimensional reconstructions, as in Computer Tomography (CT), absorption-based X-ray imaging techniques are offering the medical practitioner a high-resolution structural view of the human body's inner parts.

Despite the many advances made in functional X-ray measurement techniques, described in section 4.1 below, medical X-ray imagery still look the same, as in 1895, when W. C. Röntgen discovered X-rays [26]: They are grayscale representations of the local integrated X-ray density, showing structural detail of the object under study; no functional or compositional information can be gleaned from them.

The reason for this restriction is the very limited number of contrast mechanisms that are available in the diagnostic X-ray range from about **10 keV** to **150 keV**. As discussed in sections 2.2.2 and 2.2.3, there are essentially only two distinct physical attenuation effects in this energy range, photoabsorption and Compton scattering, each with its characteristic energy dependence of the absorption behavior, described by the textbook equations (2.8) and (2.9).

As a consequence of this situation, at most two distinct physical parameters can be measured at each location in an X-ray or CT image: The photoabsorption component μ_p and the Compton component μ_c of the total linear attenuation coefficient μ, which is the sum of the two components:

$$\mu = \mu_p + \mu_c \tag{4.1}$$

Since the attenuation behavior as a function of energy for both effects are well known, the two components can be calculated, once two attenuation measurements in two different X-ray photon energy bands have been made. This technique is called dual-energy absorptiometry or dual-energy CT imaging [2].

The driving force behind the present thesis is the fundamental question whether there exists a (subtle) physical effect that has not yet been exploited, which would allow the extraction of more information out of X-ray attenuation measurements. The aim is to contribute a novel and practical technique to the existing arsenal of X-ray

measurement methods, in particular for biomedical applications, which would make it possible to reconstruct functional or compositional two or three dimensional X-ray imagery out of suitably modified attenuation measurements.

4.1. State of the art of functional X-ray measurement techniques

In fact, several X-ray measurement techniques are known with which the composition of an object, in terms of different elements or materials, can be identified. All of them have their own advantages and drawbacks. The following list is not intended to be exhaustive. K-edge imaging [29] uses the increase of absorption at the energy corresponding to a shell for a specific element to identify it. For each element another energy is needed as the k-edges for different elements are distant from each other in the spectrum. This technique is limited to the identification of heavy elements under standard conditions. The energy of the edges from light elements is too low to be imaged in air. Under standard conditions which are necessary for biological living tissues the radiation would be absorbed in the air between the source and the detector. This is also true for X-ray fluorescence [7] as the energy is similar for the fluorescence peaks as for the edges. The fluorescence also has a limited penetration depth in the object. The photons generated deep in the object will have a too low probability to reach the detector as they are strongly absorbed within the object. It is also possible to characterize the object by the measuring relative strength of Compton scattering and photoabsorption [2]. But in each point only one and at most two materials/elements can be identified. Two are possible when the intersections between photoabsorption and Compton scattering and between Compton scattering and photo disintegration are determined. If only one of these two intersections is determined then only one material can be identified.

4.2. Fundamentals of element-sensitive X-ray absorptiometry

According to the textbook equations (2.8) and (2.9), the photoabsorption and the Compton component of the X-ray mass-absorption coefficient of an element both factorize into a product of a power of the atomic number times a universal energy function that does not depend on the atomic number of the element. Also, the power of the atomic number appears to be a constant that does not depend on the energy [6].

Assuming that the textbook assertion was only an approximation and that each element had its proper, well-known energy dependence of the mass-absorption coefficient, then it could become possible, in principle, to measure the exact energy dependence of an object's absorption and to deduce from it which elements contribute to the object's composition.

In order to investigate the principal feasibility of this basic idea, the precisely measured and publicly available mass-absorption data of the National Institute of Standards and Technology (NIST) are employed, see references [8] and [16]. Since our primary interest is in biomedical applications, where relatively thin specimens must be examined, we are limiting our investigation to the photoabsorption, i.e. rather to the low-energy spectral X-ray range.

The simplest functional relationship of an element-specific mass-absorption coefficient would be a factorization into a power of the atomic number times a power of the photon energy, i.e.

$$\frac{\mu}{\rho}(E, Z) = c \cdot Z^{b(E)} \cdot E_{\gamma}^{a(Z)} \tag{4.2}$$

where the exponent $a(Z)$ depends on the atomic number Z and the exponent $b(E)$ depends on the photon energy E. By making use of the NIST data in the energy range **9.5 keV** to **14.5 keV**, a non-linear fit of the physically measured mass-absorption coefficient to the simplified approximation in equation (4.2) results in the surprising behavior of $a(Z)$ as a function of atomic number shown in figure 4.1 and $b(E)$ as a function of energy shown in figure 4.2. In both cases, the different values of the exponents are unique. This implies that each element exhibits, indeed, its unique functional behavior in terms of atomic number and photon energy.

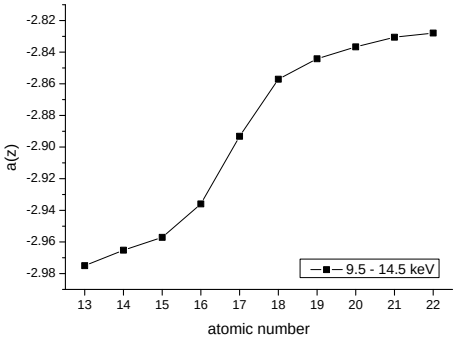

Figure 4.1.: The exponent $a(Z)$ is dependent on the atomic number.

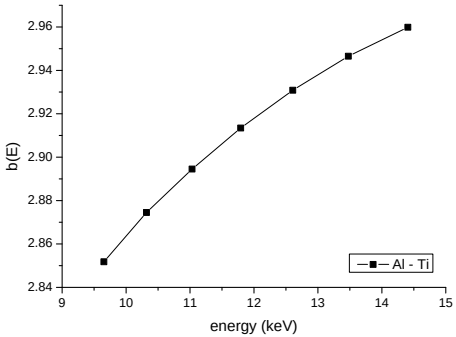

Figure 4.2.: The second exponent $b(E)$ is dependent on the radiation energy.

This realization forms the basis of all subsequent work in the framework of the present thesis to investigate the practicality of element-sensitive X-ray absorptiometry.

In order to compare our own measurement capabilities of spectral absorption data (see section 4.3 for details) with the precisely measured NIST data, we employed pure samples of aluminum, silicon, and titanium. Our own measurements and the NIST data in [8] agree very well, as can be seen from the linear representation in figure 4.3 and the double logarithmic representation in figure 4.4. These graphs also confirm that the simple factorization equation (4.2) is an excellent approximation to the actual physical behavior of the mass-absorption coefficient.

It should be noted that the exponents $a(Z)$ and $b(E)$ do not have a unique value for all possible energy ranges and for all elements. It is rather necessary to restrict oneself to a certain energy range and to a certain selection of elements in a given problem, so that a unique mathematical solution for the decomposition problem could exist.

The dependency of the exponent b on the energy E and of the exponent a on the atomic number is an essential prerequisite for the basic effectiveness of our proposed method. Otherwise the sum $\sum \mu_j(E)$ could be reformulated based on equation (2.5) as

$$\mu(E) = \sum_j \mu_j(E) = \sum_j \rho_j \cdot c \cdot Z_j^b \cdot E^a = E^a \cdot \sum_j \rho_j \cdot c \cdot Z_j^b$$

The factor c is the proportionality factor from equation (4.2). In the last equation the sum $\sum_j \rho_j \cdot c \cdot Z_j^b = c''$ would be independent of the energy E and can be simplified to a single constant. From a measurement based on such an absorption law no information about the elemental distribution could be found in this energy range.

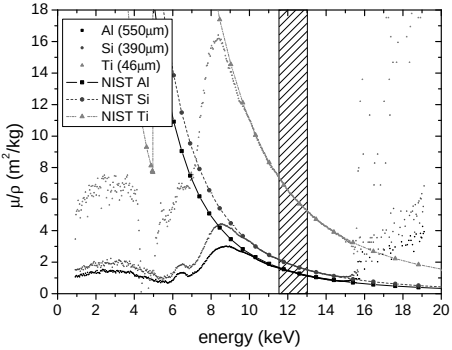

Figure 4.3.: Comparison between tabulated and measured absorption spectra for aluminum, silicon, and titanium. The measurements have been made with an additional silicon sheet of **390 µm** for the base attenuation of the beam.

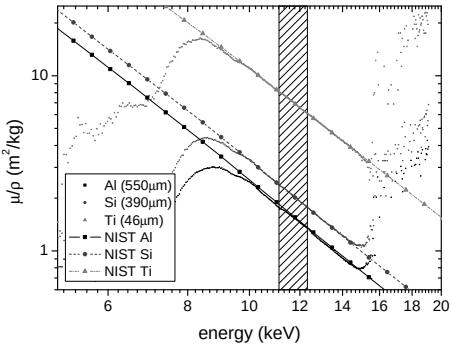

Figure 4.4.: The data of the three references for the element sensitive measurement.

This derivation shows the importance of the dependency of exponent b on the energy E for the method developed in this work.

4.3. Instrumentation

The setup for element sensitive X-ray detection is shown in figure 4.5. An X-ray source (described in section 3.1.1) irradiates the object; the photons traverse the object and hit the spectrometer.

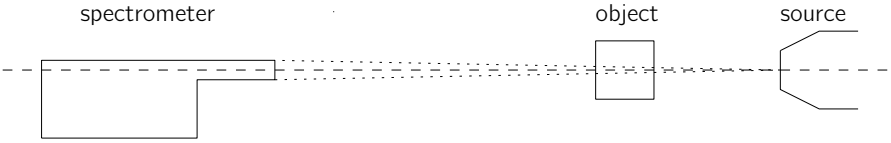

Figure 4.5.: A schematic representation of element sensitive element measurement setup.

4.3.1. X-ray spectrometer

The spectrometer used in this work is produced by Amptek (X-123; see figure 4.6). The spectrometer consists of three parts

- detector and preamplifier (XR100CR)
- digital pulse processor (DP4)
- power supply and interface board (PC4-3)

All of these parts are assembled in one casing.

The detector is a silicon PIN-diode which is protected by a thin ($25\,\mu m$) beryllium window as shown in figure 4.7. The X-ray electrons are absorbed at least partially in this diode with a surface of $5\,mm^2$ and a depth of $680\,\mu m$. The absorbed energy generates electron-hole pairs. The mean energy required to generate an electron-hole pair is $3.63\,eV$ [30]. The energy of the photon can be calculated from this energy and the numbers of electron-hole pairs in the diode. To do so each photon must be detected separately. The diode is cooled down by a thermoelectric cooler to a temperature of

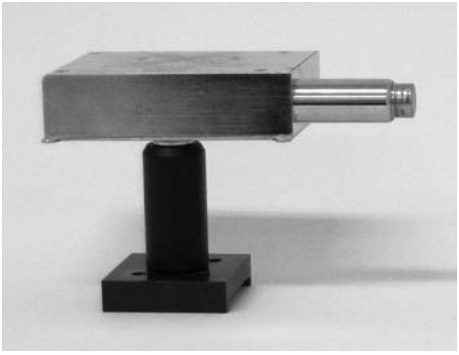

Figure 4.6.: The Amptek X-123 spectrometer. The resolution is 149 eV at 5.9 keV and 25.6 µs time to peak.

85 °C below room temperature. A collimator in front of the diode limits the radiation which reaches the diode. This collimator filters photons partially out, if they are not created in the X-ray source. The collimator is made of silver and has a diameter of 2.05 mm. This is the reason why the silver fluorescence peaks are found in the spectrum at for example 22.16 keV. Those fluorescence peaks are visible when the spectrometer is irradiated by X-ray photons of higher energy than the peaks.

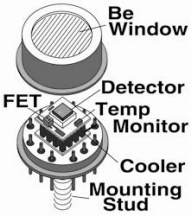

Figure 4.7.: Detection diode of Amptek spectrometer X-123

The design of the digital pulse processor is shown in figure 4.8. The analog to digital converter operates at 20 MHz. The pulse detection can be adapted by adjusting several parameters as for example peaking time, flat top time, and pile-up rejection. The energy distribution is stored in channels. The number of these channels can be

selected from 256 to 8192. Each of these channels has 24 bits storage and therefore allows 16.7×10^6 counts per channel.

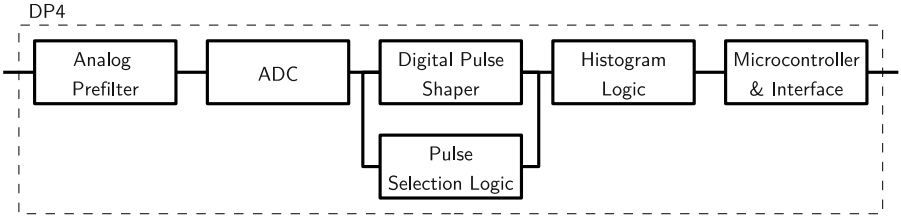

Figure 4.8.: The block diagram of the digital pulse processor (DP4)

An universal serial bus (USB) connects the spectrometer with a computer. It is important to first power up the spectrometer before connecting to a computer through USB otherwise the device is not accessible.

4.3.1.1. Energy calibration

The spectrometer needs a calibration in order to compare the energy of each channel. The energy of the channels can be estimated thanks to the fluorescence peaks of different elements (see figures 4.9a and 4.10a). The fluorescence peak can be approximated by a Gaussian curve. With this intermediate step the resolution becomes better than with only one channel. The energy of the other channels is linearly interpolated (see figures 4.9b and 4.10b). The spectrometer is quite stable over the time but its output will change considerably when the parameters are changed. For example changing the precision will shift the energy.

In a standard environment several fluorescence peaks are visible dependent on the maximal energy. Because the source target is constructed with tungsten, its fluorescence peaks ($L\mathit{l}$, $L\alpha_1$, $L\beta_1$, and $L\gamma_1$) are present in the energy range of 7.39 keV to 7.39 keV. Silver peaks (22.17 keV–24.94 keV) are present in the detector due to the collimator. Other peaks originate from the mechanics and shielding. Peaks from chromium and iron as well as lead are produced by the shielding. Copper and zinc peaks originate from the rotation stage which is made out of brass.

If there are not enough fluorescence peaks for a calibration with a simple measurement, additional elements can be excited. The setup is shown in figure 4.11. It

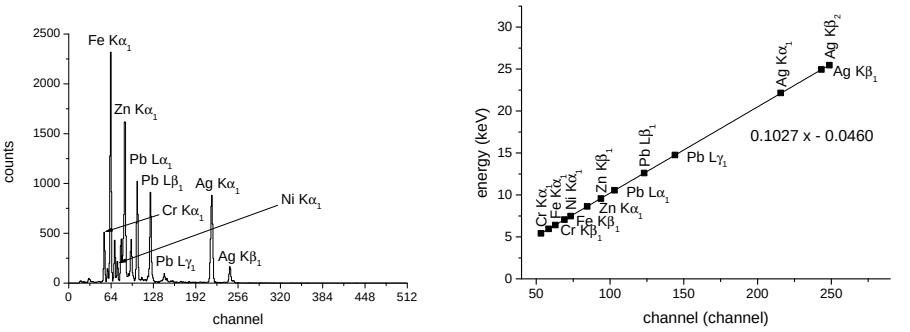

Figure 4.9.: It is possible to calibrate the spectrometer thanks to the fluorescence photons from different elements (a). In (b) the linear fit of the energies of the different peaks is shown.

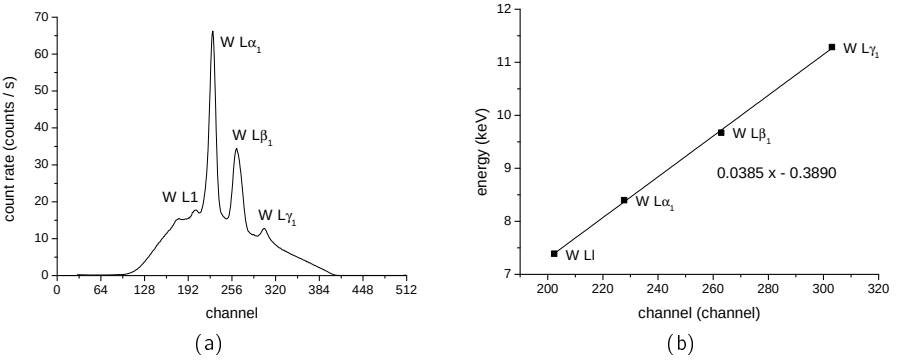

Figure 4.10.: The calibration can be done on the tungsten peaks of the source (a). The fit of the energy of those peaks is presented in (b).

is important that the primary beam is blocked and in this way only the fluorescent photons can reach the detector. Copper, platinum, and lead are used as calibration references in our setup.

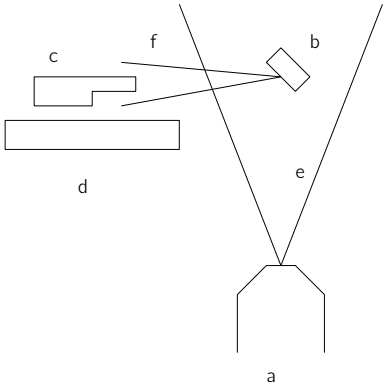

Figure 4.11.: The setup to measure the fluorescence peaks to calibrate the detector. a) is the source, b) the calibration reference, c) the spectrometer, d) the protection of the spectrometer from the direct beam, e) the radiation of the source, and f) the fluorescence radiation.

Iron is not used for the calibration because of its standard form of alloy. An alloy has all the peaks from all elements and therefore the peaks become ambiguous.

4.3.2. Spectrometrical 2D array

The spectrometer used in this work is limited to a single pixel. To avoid scanning for imaging a one or two dimensional array of spectroscopical pixels is necessary. A potential chip is the timepix chip [21]. This chip can measure the energy of each photon by a method called time over threshold. In this method the time during which the signal is above a threshold is measure. This time is proportional to the energy of the photon.

CSEM is developing a low noise scintillator-based spectroscopical pixel [22]. The amplitude noise in pulse detection is $12\,e^-$. In direct conversion this would correspond

to an energy noise of approximately 50 eV. With a scintillator the conversion efficiency is much lower and therefore the energy noise will be larger. The characteristics of this pixel would allow the construction of a pixel array. The potential count rate would be in the same range as in the spectrometer from Amptek. It is possible to detect 5000 counts per second from a pulsed light source. The photons of a X-ray source are not regularly distributed in time but they rather exhibit a Poisson distribution. As a consequence of the uneven time distribution, the spacing between two photons is in some cases shorter than the average. Because of this the average count rate must be lower for such a distribution.

4.3.3. Holders

The holder for the element sensitive measurements are optimized for this work. The first holder used is shown in figure 4.12. With this holder the position of the object could be changed thanks to a special rail. The X-ray beam passes through the hole in the holder. Therefore the acrylic glass used for the holder will not be in the beam path. The object must have the dimension of roughly $5\,\mathrm{cm} \times 2\,\mathrm{cm}$. An object of this size will be constrained by all four sides. This is important in the case where powder is measured between two sheets of metal.

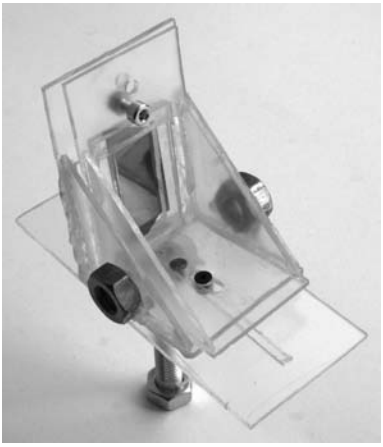

Figure 4.12.: The holder to fix the metal sheets and the powder between the sheets. On the picture there is one silicon plate fixed in the holder. Below the holder the rail is visible to move the holder.

This holder can only accommodate one object. As the source is not stable enough for a measurement over a power cycle, the holder had to be further improved. The second type of holder is shown in figure 4.13. This holder can accommodate two objects at the same time. Because some experiments show the necessity to keep the object at the nearest possible point to the source, the position is fixed near the source. The objects are now fixed on three sides. This makes the fixation of a powder sample more difficult. Also the risk of breaking monocrystalline silicon increases. The algorithm to find the correct geometrical position of both objects is described in section A.3.

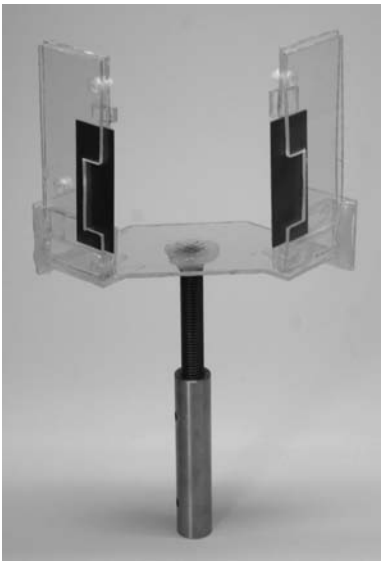

Figure 4.13.: This holder is the development of figure 4.12. The advantage is that this holder has two objects (sheets) fixed, selectable with the rotation stage.

A special holder is shown in figure 4.14. This holder was built to acquire absorption images with the sample of the element sensitive measurements. But in this case the rotation axis is in the center of the sheets. This was needed to rotate the sheets and to increase the projected thickness.

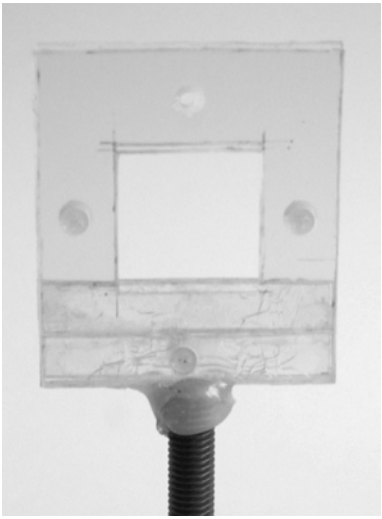

Figure 4.14.: This holder can hold the same samples as the precedent holders but the rotation axis is in the center of the sheets. This is needed in the comparison of the classical X-ray absorption imaging and the element sensitive measurement.

For aqueous samples a holder with cuvettes was built. The cuvette used is a SpecVette from ALine Inc. with part number SV1000-25 (figure 4.15). The cuvettes consist of two separate reservoirs with a volume of **60 µl** each and a path length of **1000 µm**. Up to six cuvettes can be fixed in the the revolver holder in figure 4.16. The plan of the holder is in section A.6.

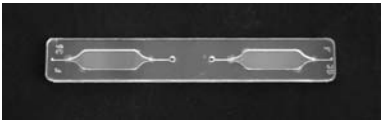

Figure 4.15.: One cuvette with two chambers and a liquid thickness of **1 mm**.

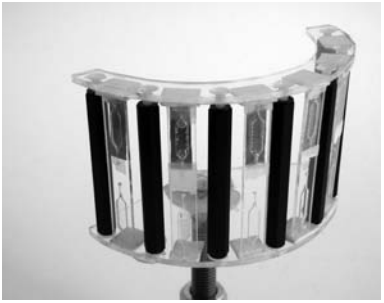

Figure 4.16.: Holder with 6 cuvettes for measuring multiple liquids at one time.

4.4. Algorithms

This section is divided into the following parts. First the selection of the searched elements and the considered energy range is described. After the description of the

measurement a calculation algorithm is described, following an algorithm to decrease the exposure time under certain condition is presented. Finally the error propagation in the presented algorithm is described.

The standard method consists of measuring the absorption spectrum with two measurements. First, the initial intensity is measured without the sample in the X-ray beam. Together with a second measurement under the same conditions but with the sample in the beam path, the absorption of the sample can be calculated with equation (2.6).

In principle, only combinations of pure elements could be detected with the present technique. Chemical combinations of multiple elements do not follow exactly the same power law for absorption as pure elements. Nevertheless our experiments indicate that it is quite possible, in practice, to extend our method of element-sensitive X-ray imaging also to composite materials. For example some measurements with salts (NaCl, $CaCl_2$) have successfully been carried out in this work.

4.4.1. Element selection

For the selection of the detectable elements two properties are important. One is linked to the energy selection. The scattering must only be partially responsible for the absorption. In this work this limit was chosen to be 10 %. This limit is shown in figure 4.17 for aluminum. If the energy is fixed first, the upper limit of the energy will restrict the element selection towards the light elements. In this work the elements are selected in a first step, therefore the energy range had be chosen accordingly to this element selection.

The second property is the difference between the absorption behaviors of the elements. This can be quantified by the exponent $a(z)$ of equation (4.2). The exponents do not need to be a monotonic function of the atomic number but the difference between the various exponents has to be greater than a threshold. It is not only the difference between two neighbors but the difference between the exponents of all elements. A graph of this property is shown in figure 4.18. In this figure the minimal difference is $\Delta d > 0.005$. The shaded area is a possible selection. Other selections would also be possible. For example the two elements $Z = 20$ and $Z = 21$ can be replaced by $Z = 22$ or $Z = 23$.

It is also possible to detect compounds instead of only pure elements. This is possible under the condition that one element of this compound is unique and not present in the sample outside of this compound. Additionally this element fulfills the conditions described above to be detectable. This strategy was used in salt measurements. The two salts sodium chloride (NaCl) and calcium chloride ($CaCl_2$) could be detected in water (H_2O). In the selection of these compounds sodium (Na), calcium (Ca), and

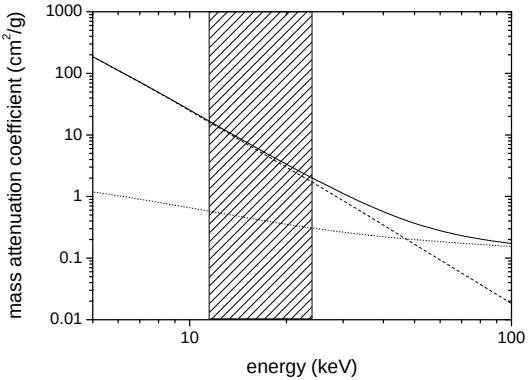

Figure 4.17.: The absorption characteristic of aluminum is given by the solid line. The dashed line is the photo-absorption and the dotted one the scattering. In order to make the algorithm work with sufficient precision, only a limited part of scattering is permitted. This is indicated by the shaded area.

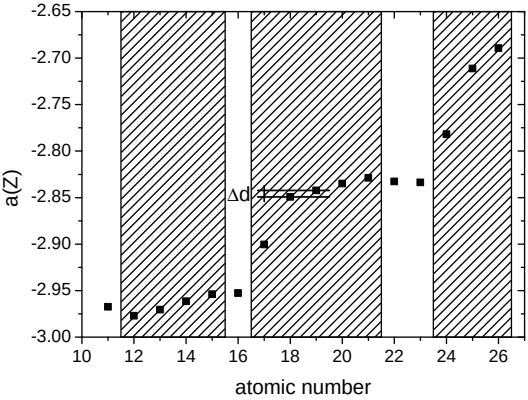

Figure 4.18.: The exponent of the energy in the absorption law is dependent on the atomic number of the element. If the difference is large enough the element can be distinguished with the present method. A possible range of atomic numbers that can be separated is indicated by the shaded area.

oxygen (O) are the detectable elements. The other elements of the compounds cannot be neglected in the calculation but they can be included in those three elements.

4.4.2. Energy selection

Besides the property mentioned in the last section there are several additional aspects that have to be considered. One is the exclusion of fluorescence peaks. All fluorescence photons generated outside the target of the source will perturb the result of the equation (2.6). Especially critical for fluorescence are the sample, the sample holder, the shielding, and the collimator of the spectrometer. This collimator is made out of silver and therefore peaks at 22.17 keV and at 24.94 keV are common. The fluorescence peaks of the target material, in this work tungsten, can be included. Those photons have the same path as the ones generated by the bremsstrahlung. In the figure 4.19 those peaks are visible.

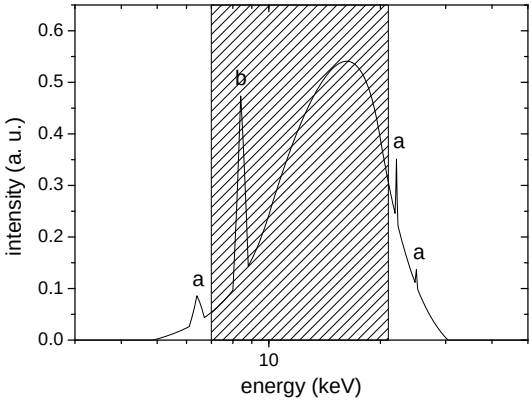

Figure 4.19.: A spectrum of a broadband X-ray source. The shaded area indicate the potential selectable energies. The peaks (a) (e.g. iron and silver) must be skipped. The fluorescence from the target (b) can be part of the energy selection.

Another criteria for the energy selection is the measurable photons flux. The acceleration voltage of the source will limit the potential energies of the electrons and, consequently the upper energy of the emitted X-ray photons. The upper energy limit

can restrain the useful photon flux and therefore determine the exposure time for the measurement without a sample. For the lower limit this is true for the measurement with the most absorbent object.

In most measurements done in this work the energy range was from 11.58 keV to 13.09 keV.

4.4.3. Calculation

The input data of the algorithm are the spectra of the absorption. All elements present in the object must be included in the calculation, and it must be therefore known in advance, which elements could be present in the sample. Of course, impurities below a threshold can be neglected. This threshold is dependent on the atomic number of the element and would require additional research to determine its value in practice. The higher the atomic number is, the lower the threshold will be as the absorption is increasing. All elements outside of the selected range are ignored by the algorithm and therefore they will distort the result if they are present nevertheless in the object.

Due to the strictly linear nature of the X-ray absorption process, the identification of the various elements in a sample can be calculated with a linear method, requiring only linear algebra computations. As mentioned above, the mass-absorption coefficient can be modeled by

$$\mu = \sum_j \rho_j \cdot c \cdot Z_j^{b(E)} \cdot E^{a(Z)} = \sum_j c \cdot Z_j^b \cdot E^{a(Z)} \tag{4.3}$$

where the index j identifies the elements of the composition. The factor c is a constant and $b(E)$ is simplified to a constant b because the measured range in energy is small.

A matrix $\boldsymbol{B}$ can be defined as

$$B_{ij} = c \cdot Z_j^b \cdot E_i^{a_j}$$

where the index i identifies the energy. If the last equation is combined with (4.3) this gives

$$\mu_i = \sum_j B_{ij} \rho_j$$

or in vectorial notation

$$\vec{\mu} = \boldsymbol{B}\vec{\rho} \tag{4.4}$$

The matrix $\boldsymbol{B}$ can also be constructed directly from the reference data. From the reference data the mass-absorption coefficient $\frac{\mu}{\rho}$ is needed. The incertitudes on

the thickness and on the density and their effect on the calculated mass-absorption coefficient are discussed in section 4.7.5. In this case the matrix $\boldsymbol{B}$ is calculated as

$$B_{ij} = \left(\frac{\mu}{\rho}\right)_j (E_i) \tag{4.5}$$

This definition also fulfills (4.4). This vectorial equation is multiplied on both sides by the thickness x, leading to

$$\vec{\tau} = \boldsymbol{B}\vec{\varphi} \tag{4.6}$$

In this equation the length-absorption coefficient $\vec{\tau} = x\vec{\mu}$ is the measured quantity. $\vec{\tau}$ is a vector over an energy range. The result of the calculation will be $\vec{\varphi} = x\vec{\rho}$ for each element searched in the composition. To solve the equation the matrix $\boldsymbol{B}$ must be inverted

$$\vec{\varphi} = \boldsymbol{B}^{-1}\vec{\tau}$$

This inversion is done by QR decomposition [31]. QR decomposition is preferred over LU decomposition because of its higher numerical stability.

In a QR decomposition a matrix $\boldsymbol{B} = \boldsymbol{QR}$ is separated into two matrix. The matrix $\boldsymbol{Q}$ is an orthogonal matrix $\boldsymbol{QQ}^T = \boldsymbol{I}$. The second matrix $\boldsymbol{R}$ is an upper right triangle matrix, i.e. the matrix $\boldsymbol{R}$ with size $m \times n$ has vanishing elements $R_{mn} = 0$ for $m > n$.

The QR decomposition is applied to the equation (4.6)

$$\vec{\tau} = \boldsymbol{QR}\vec{\varphi}$$

Together with the properties of the orthogonal matrix $\boldsymbol{Q}$ this can be rewritten as

$$\boldsymbol{Q}^T\vec{\tau} = \boldsymbol{Q}^T\boldsymbol{QR}\vec{\varphi} = \boldsymbol{R}\vec{\varphi}$$

The left part of the equation $\boldsymbol{Q}^T\vec{\tau}$ can be precalculated and gives a new vector. With this new vector the equation can be solved as $\boldsymbol{R}$ is an upper right triangle matrix and so the elements of the vector $\vec{\varphi}$ can be calculated from the bottom to the top.

From this integrated density φ the density ρ can be calculated if x is known. This is the case in a tomographical image where the dimension of a voxel is fixed and known in advance. In this case the result would be a specific density ρ_j for each element in each voxel of the image.

From the equation of the absorption (2.2) the length-absorption coefficient $\tau = x \cdot \mu$ can be calculated

$$\frac{I_2}{I_1} = \frac{I_0 e^{-(x_1\mu_1 + x\mu)}}{I_0 e^{-x_1\mu_1}} = e^{-x\mu}$$

The matrix $\boldsymbol{B}$ is constructed by the mass-absorption coefficient $\frac{\mu}{\rho}$. In a first step the exponent $\tau = x\rho\frac{\mu}{\rho}$ must be split into its components. The mass-absorption coefficient

can be calculated with

$$\frac{\mu}{\rho} = \ln\left(\frac{I_1}{I_2}\right)\frac{1}{x\rho}$$

For the measurements the length-absorption coefficient τ is directly used

$$\tau = \ln\left(\frac{I_1}{I_2}\right)$$

For the two measurements there are two strategies. One is to make a measurement with the object in question in the beam and a second one without the object. The other strategy is to scan the object and therefore without having an absolute value of the composition but a gradient. If the scan leaves the object at one point an absolute measurement is also possible. In this work only the first strategy is applied.

For the calculation an element selection was done which might not correspond to the actual elemental composition of the sample. In this case, the absorption of non-selected elements must be compensated by the nearest element in the selected range. Because this is a different element the least squares fit will decrease in quality. This effect can be seen by the residue of the least squares fit which is

$$\vec{r} = \boldsymbol{B}\vec{\varphi} - \vec{\tau}$$

From this residue a quality factor

$$q = \frac{\|\vec{\tau}\|}{\|\vec{r}\|}$$

can be calculated. The value of the residue is dependent on the distance to the nearest element in the selection. The residue and therefore the quality factor increase with the distance. Further research must be done to be able to convert the quality factor to a probability of a correct element selection.

4.4.4. Measurements relative to another object

A maximal count rate must be selected to warrant a sufficient quality of the measurement. To guarantee the quality of an absorption measurement, two mandatory measurements must be performed with the same base spectrum. The same spectrum can only be guaranteed with a typical X-ray source when the source is thermally stable, through uninterrupted operation. On each power cycle the spectrum will be slightly different. The absorption capacity of the weaker absorbing object will determine the maximal X-ray power to keep the count rate below the selected level.

At the same time the number of counts per channel will determine the noise in the signal. To get above a selected signal-to-noise ratio the number of counts in each channel must be above a certain limit. From these two constrains (count rate and

number of counts) the time needed for a measurement is dependent on the absorption power. Minimizing the absorption power will minimize the time for the measurement.

Another approach is to limit the time needed for the measurement and to use an additional object with a comparable absorption power as the objects. With this approach only one measurement must be done with a high absorption power and therefore a long integration time for the measurement. All the subsequent measurements will be shorter in time.

As an example one measurement series is done with **75 µm** of titanium to measure **390 µm** silicon and **550 µm** aluminum. The thickness of the titanium was selected to have an absorption power between the silicon and the aluminum object.

The benefit on time will be dependent on the numbers of measurement and can therefore not be quantified. Long measurements will especially benefit from this approach. The main drawback is that four times higher number of counts are necessary for the same result quality. The reason therefore is explained in the next section.

4.4.5. Error propagation

In the calculation for the error propagation the worst case is considered. Some of the errors are considered to be zero as they will only affect the result of one element but not the elemental distribution. The two variables which are considered to be without an error for this calculation are the thickness x and the density ρ of the reference object.

The absorption $A = \frac{I_2}{I_1}$ is calculated by the ratio of two intensities I and has the error

$$\frac{\Delta A}{A} = \frac{\Delta I}{I} + \frac{\Delta I}{I} = 2\frac{\Delta I}{I}$$

In this equation, for simplicity, the error difference with a changing count rate and a different exposition time are neglected.

The absorption-length coefficient is defined as $\tau = x \cdot \mu = \ln(A)$ and has an error of

$$\Delta\tau = \Delta A \cdot \frac{\partial \tau}{\partial A} = \Delta A \cdot \frac{1}{A} = \frac{\Delta A}{A} = \frac{2\Delta I}{I}$$

In the case of the relative measurement as described in the last section the absorption-length coefficient is the sum of the two coefficients $\tau = \tau_1 + \tau_2$. Because of this sum the right side of the last equation must be doubled and becomes

$$\Delta\tau = \frac{4\Delta I}{I}$$

As we assumed that x and ρ do not have an error, the error on the mass-absorption coefficient is

$$\Delta\frac{\mu}{\rho} = \frac{2\Delta I}{I}$$

This is true even if there are errors in x and ρ but they do not have a effect on the element distribution as shown in section 4.7.5.

The second part of this estimation is for the resulting integrated density $\varphi = x\rho = \frac{\tau}{\mu/\rho}$. For this calculation the condition κ of the matrix $\boldsymbol{B}$ must be known. The condition is calculated by the following equation [10]

$$\kappa(\boldsymbol{B}) = \frac{\max\limits_{\|\vec{x}\|=1} \|\boldsymbol{B}\vec{x}\|}{\min\limits_{\|\vec{x}\|=1} \|\boldsymbol{B}\vec{x}\|}$$

The numerical calculation of the condition is done by a singular value decomposition. The condition is the ratio between the biggest and the smallest singular value of the matrix $\boldsymbol{B}$. The condition $\kappa(\boldsymbol{B})$ can be in a wide range. As a numerical example the matrix in the case of aluminum and silicon detection has a condition in the range of 200 to 600.

The error of the resulting integrated density φ is

$$\frac{\|\Delta\varphi\|}{\|\varphi\|} = \kappa(\boldsymbol{B})\frac{\|\Delta\tau\|}{\|\tau\|} = \kappa(\boldsymbol{B})\frac{\Delta\tau}{\tau} = \kappa(\boldsymbol{B})\frac{2\,\Delta I}{\tau\, I} \tag{4.7}$$

The simplification from the norm to one element is possible because all elements of the vector have the same values.

The stability of the algorithm described by equation (4.6) is given by

$$\frac{\tilde{\epsilon}}{\epsilon} = \frac{1}{\kappa}(1+\kappa)$$

where $\frac{\tilde{\epsilon}}{\epsilon}$ is the relative amplification of the error due to the incertitude on the matrix $\boldsymbol{B}$. κ is the condition of the matrix $\boldsymbol{B}$. In our case this equation can be simplified because $\kappa \gg 1$ to

$$\frac{\tilde{\epsilon}}{\epsilon} \approx 1$$

From this result the equation (4.7) gives the error estimation of this algorithm.

4.5. Reference objects

The measurements are made with pure elements (see figure 4.20 and table 4.1). The three metals used (aluminum, silicon, titanium) are in the form of platelets with the dimension $2\,\mathrm{cm} \times 5\,\mathrm{cm}$ and a thickness of around $0.5\,\mathrm{mm}$. As titanium has a stronger absorption also thinner sheets are used. Those sheets can by stacked in the holder (see section 4.3.3). The element range also includes phosphorus and sulfur as powder. To place those elements in the holder two metal sheets and a O-ring are necessary.

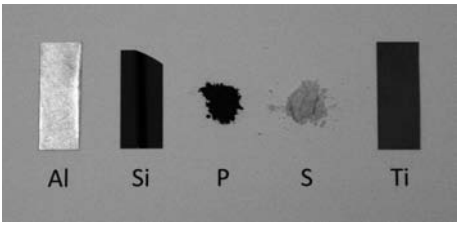

Figure 4.20.: The element sensitive measurements are made with the following five pure elements: aluminum, silicon, phosphorus, sulfur, titanium.

Element	Purity	Thickness	Density
Al	99.9 %	500 µm - 600 µm	2700 $\frac{kg}{m^3}$
Si	99.9999 %	390 µm	2330 $\frac{kg}{m^3}$
P	99 %	1000 µm (O-ring)	$\sim$ 1000 $\frac{kg}{m^3}$
S	99.5 %	1000 µm (O-ring)	$\sim$ 1000 $\frac{kg}{m^3}$
Ti	99 %	23 µm	4500 $\frac{kg}{m^3}$
Ti	99 %	127 µm	4500 $\frac{kg}{m^3}$
Ti	99 %	510 µm	4500 $\frac{kg}{m^3}$

Table 4.1.: characteristics of the used elements.

The powder (phosphorus, sulfur) was placed in a volume defined by two metal sheets and a O-ring in between. The O-ring used is from Normatec[1] with an inner diameter of $17.5\,\mathrm{mm}$ and a thickness of $1.00\,\mathrm{mm}$. This defines the volume of $9.6 \times 10^{-7}\,\mathrm{m}^3$. The density of the powder is not fixed as the powder can be compressed with different strength. The actual density of the powder can be measured by the weight of the powder and the volume fixed by the construction. The density is in the range of $900\,\frac{\mathrm{kg}}{\mathrm{m}^3}$ to $1300\,\frac{\mathrm{kg}}{\mathrm{m}^3}$.

If a second thickness for the powder is necessary an X-ring[2] was selected. This X-ring has an inner diameter of $15.60\,\mathrm{mm}$ and a thickness of $1.78\,\mathrm{mm}$. The volume enclose by this X-ring is $1.4 \times 10^{-6}\,\mathrm{m}^3$.

Another measurement series was performed with two different salts dissolved in water. In this case cuvettes are used with a fixed length through the volume. The variable parameter therefore is the concentration of the salts. For sodium chloride (NaCl) the maximal solubility in water at $25\,°\mathrm{C}$ is $359\,\frac{\mathrm{g}}{\mathrm{l}}$. For the second salt, calcium chloride ($CaCl_2$) the maximal solubility at $20\,°\mathrm{C}$ is higher at $745\,\frac{\mathrm{g}}{\mathrm{l}}$. The water used to solve the salts has a conductivity of $0.055\,\frac{\mu\mathrm{S}}{\mathrm{cm}}$.

4.6. Experimental verification

All the element sensitive measurements are made with an acceleration voltage of $15\,\mathrm{kV}$. The channels 311 to 350 of the spectrometer are used, which corresponds to an energy from $11.6\,\mathrm{keV}$ to $13.1\,\mathrm{keV}$. The spacing between two channels is around $0.04\,\mathrm{keV}$. This energy range is shown in figure 4.21 with the corresponding absorption and count rate. The selected energy range is very narrow because the spectral shape changes strongly between the measurements. Outside this range the available information is limited. The tube current is selected to keep the count rate below $3250\,\frac{\mathrm{counts}}{\mathrm{s}}$ and to remain in the linear range of the spectrometer. For the metal measurements, an additional sheet of $390\,\mu\mathrm{m}$ of silicon must be placed in the beam path to attenuate the beam below this limit. The source is operated at $9\,\mu\mathrm{A}$ for the metal measurements. In the case of the salt measurements the base absorption is made with $25\,\mu\mathrm{m}$ of titanium, as shown in figure 4.29, and the source is operated at $2\,\mu\mathrm{A}$. The exposure time is controlled by the number of counts in the selected channels. The count limit was selected to be $100\,000$ counts for data quality reasons. The control program stops the measurement once this count limit is passed. The measurements will also stop after a maximum time of $10\,000\,\mathrm{s}$ depending on which limit is achieved first. With even longer exposure times, the quality would start to decrease as shown in section 4.7.4. Two measurements with

[1] O-ring part number: Normatec FKM NT 80.7/75 ORM 0175-10
[2] X-ring part number: A+P X-ring NBR 70.45-2 AS 016

the count limit are shown in figure 4.22. Some measurements are only made with the counts as limit, but no limit in exposure time.

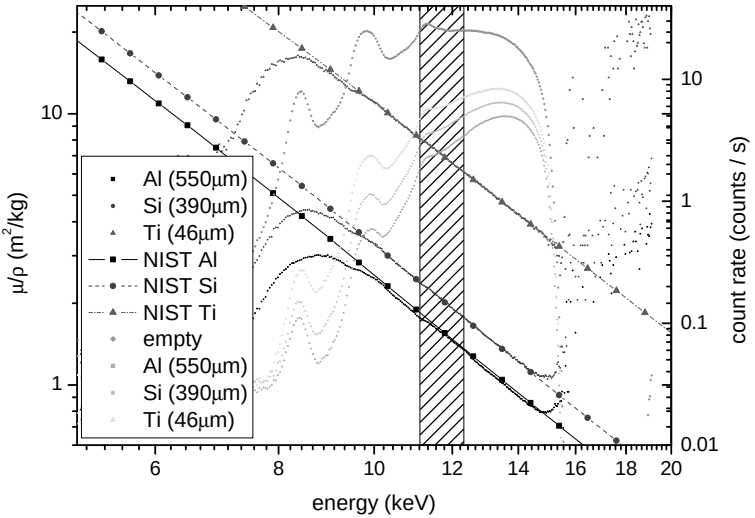

Figure 4.21.: The mass-absorption coefficient from silicon, aluminum, and titanium is compared to the NIST table data and represented by the three stronger grays. The count rate is plotted in the same range with the weaker grays.

In the conventional X-ray imaging the transmission over the entire energy spectrum is integrated into a single value. This value depends on the thickness of the sample, its density, its composition, and the mass-absorption coefficient of all involved elements, but these parameters cannot be separated. Without any prior knowledge, no conclusion on the relative value of these four parameters can be made.

The two samples presented in figure 4.23 cannot be distinguished by conventional X-ray imaging. The experimental setup is shown in figure 4.24. Sample A consists of two slabs. One slab of aluminum with a thickness of $550\,\mu m$ and one slab of silicon with a thickness of $390\,\mu m$ are combined. The second sample B consists of two slabs of silicon with a total thickness of $t = 780\,\mu m$. This second sample is tilted by an angle of $\alpha = 24°$. The effective thickness d becomes $d = \frac{t}{\cos\alpha} = 854\,\mu m$.

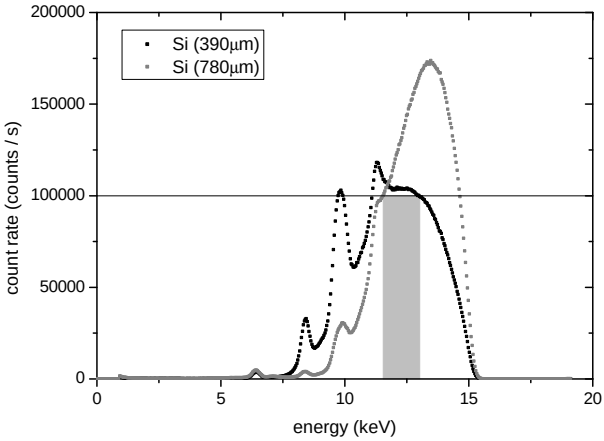

Figure 4.22.: The spectra are integrated until the channels in the selected energy range have at least **100 000 counts**.

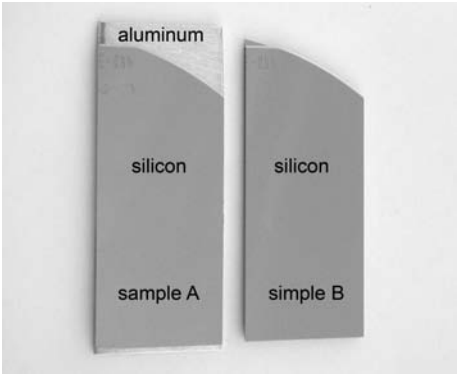

Figure 4.23.: The two samples used in the demonstration of element sensitive X-ray measurements. The object A consists of two platelets, one of silicon (**390 µm**) and one of aluminum (**550 µm**). The object B also consists of two platelets but both are silicon (**780 µm**).

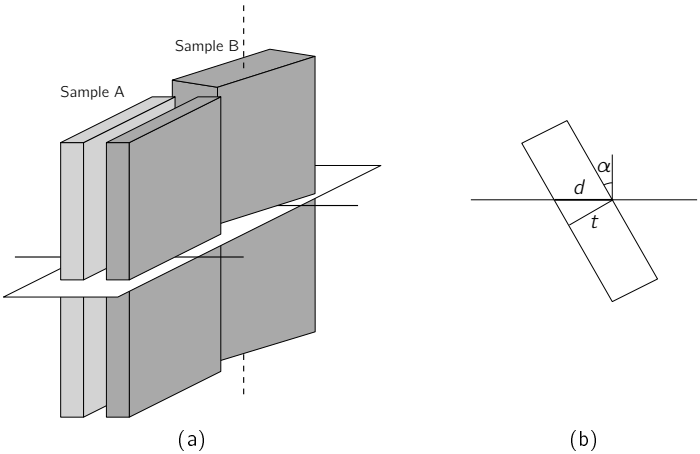

Figure 4.24.: Diagram showing the experimental geometry. The sample B can be rotated to achieve the necessary thickness. In (b) the change of the effective thickness is shown.

The result of the conventional X-ray imaging are presented in figure 4.25. The two samples have the same X-ray absorption and cannot be distinguished in this conventional imaging modality. The two images show a portion of the sample close to an edge. The diagram below the pictures shows the intensity along the dashed line. The diagram visualizes the absolute intensity levels of the image better than the grayscale images. The values of those lines are normalized. $I = 1.0$ is the intensity of the beam without an object.

In figure 4.26, the results of the element sensitive measurements are presented. These results are the average of 64 measurements of sample A and 48 measurements of sample B. 50 energy channels from the spectrometer are selected. From these 50 each time 5 channels are summed together and form a single energy level. This leads to ten energy levels with a spacing of 0.2 keV. The error bars on the results are determined by the standard deviation of the corresponding series.

The actual composition of the two samples is within the error bars of the measurements. The two samples can be clearly separated. In the measurement of the composite sample the result detects more silicon than aluminum. While in fact the opposite is true. The measured ratio $\frac{\rho_{Al}}{\rho_{Si}}$ is for sample A $\frac{\rho_{Al}}{\rho_{Si}} = 0.85$ and for sample B $\frac{\rho_{Al}}{\rho_{Si}} = 0.28$

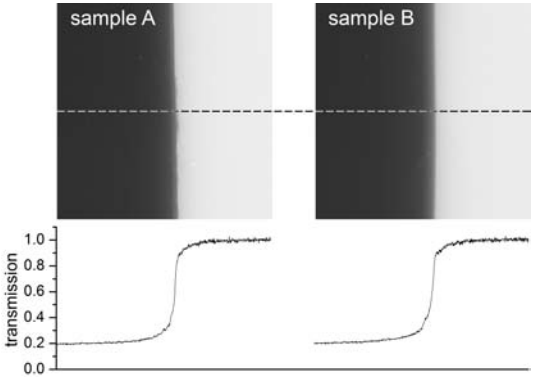

Figure 4.25.: The two plates from 4.23 are imaged by conventional X-ray absorption. The low part shows the intensity along the dash line. These both images cannot be distinguished from each other.

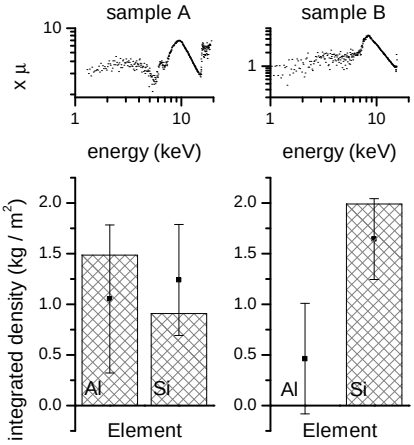

Figure 4.26.: The results of one element sensitive measurement for each sample. The columns represent the actual content and the points the result of the measurement with their corresponding error bars.

With this method the composition of the samples can clearly be detected which is obviously not possible with to the classical X-ray imaging.

To show the capabilities and the limits of our method three materials are measured and detected at the same time. The two metals are aluminum ($Z = 13$) and titanium ($Z = 22$). The third material is the semiconductor silicon ($Z = 14$). Measurements with all seven possible combinations are done. The result are shown in figure 4.28.

The error estimation based on equation (4.7) with only shot noise on the measurement has

$$\frac{\Delta I}{I} = \frac{\sqrt{100\,000}}{100\,000} = \frac{1}{316.2} = 3.2 \times 10^{-3} \tag{4.8}$$

The estimated error for the integrated density $\frac{\|\Delta\varphi\|}{\|\varphi\|} \approx 7.5$ is too pessimistic. But the quality of the signal as seen in equation (4.8) is proportional to one over the square root of the counts. With a higher count rate and the same exposure time the quality could be increased. Because of the too pessimistic error estimation the precision is determined experimentally by a series of measurements on silicon. The result of this series is presented in figure 4.27. The vectorial norm of the average result is $\|\varphi\| = 0.47$. The standard derivation of the vectorial error's norm yields $\|\sigma_\varphi\| = 0.58$. From this calculation the relative error of the result is determined as $\frac{\|\Delta\varphi\|}{\|\varphi\|} = 1.22$.

The error bars are calculated by a simplified model. The errors of all vector elements and therefore of the elements are assumed to be equal. With this model the error of each component is

$$\Delta\varphi = \frac{\|\Delta\varphi\|}{\sqrt{3}} \cong 0.58 \cdot \|\Delta\varphi\| \tag{4.9}$$

for a three dimensional integrated density vector. The gray error bars in figure 4.27 are calculated with this rule. A ten times smaller error would be interesting and could be achieved by a number of counts that are hundred times higher. This could be done with the same exposure time but hundred times higher count rate.

The error bars of all following measurements are calculated based on equation (4.9) relative to their respective norms.

All measurements with the three metals have the same reference data and so the same matrix $\boldsymbol{B}$. The condition of this matrix $\boldsymbol{B}$ is $\kappa(\boldsymbol{B}) = 1271.0$.

For the measurements with the combination of two or three materials the sample absorption is too strong. These measurements are limited by the exposure time of 10 000 s and the desired count level could not be achieved. The quality of these measurements is therefore lower than usual and the error bars for those two measurements must be corrected. The base measurement has still the desired quality. The average counts per channel for the objects measurements is calculated. Those values can be

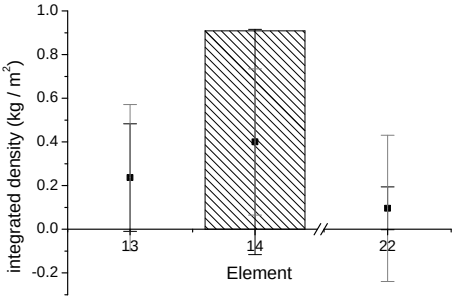

Figure 4.27.: The standard deviation of the element sensitive measurements is determined from the standard of a series of ten measurements. The standard deviation of the measurements series is shown in black and the normalized one in gray.

found in table 4.2. The equation (4.7) is taken to estimate the change in the error. In this equation $2 \cdot \frac{\Delta I}{I}$ is replaced by $(1+a)\frac{\Delta I}{I}$ with the quality change factor $a = \sqrt{\frac{100\,000}{I}}$. The increased errors are indicated on the same table. Because the single material measurements are also slightly too long, the shot noise is no more the only noise present. The error estimation is based on a silicon measurements series. Because those measurements are too long, the errors estimated for the shorter measurements are slightly overestimated.

measurement	counts	error correction
aluminum / silicon	**6750** counts per channel	2.5
silicon / titanium	**25 800** counts per channel	1.5
aluminum /titanium	**18 000** counts per channel	1.7
aluminum / silicon / titanium	**4050** counts per channel	3

Table 4.2.: The number of counts in the selected channels for the measurements stopped after **10 000 s**. In the last column the increases in error by the limited counts is indicated.

In most cases, the difference between actual and measured values is within the error

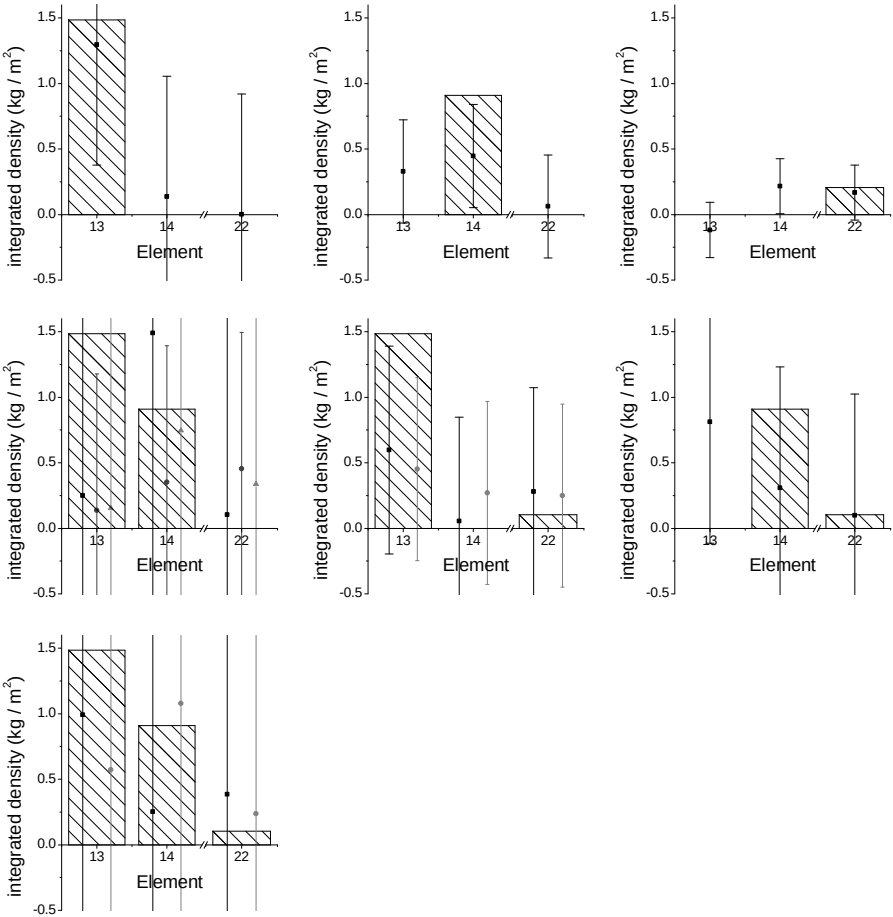

Figure 4.28.: The seven combinations of the three materials (aluminum (13), silicon (14), and titanium (22)) are presented. For some of the combinations multiple measurements are indicated with different grays.

aluminum	silicon	titanium	exposure time	count rate
-	-	-	4200 s	3300 $\frac{\text{counts}}{\text{s}}$
Al (550 µm)	-	-	42 000 s	580 $\frac{\text{counts}}{\text{s}}$
-	Si (390 µm)	-	27 000 s	420 $\frac{\text{counts}}{\text{s}}$
-	-	Ti (50 µm)	18 000 s	810 $\frac{\text{counts}}{\text{s}}$
Al (390 µm)	Si (390 µm)	-	290 000 s	110 $\frac{\text{counts}}{\text{s}}$
Al (550 µm)	-	Ti (46 µm)	190 000 s	140 $\frac{\text{counts}}{\text{s}}$
-	Si (390 µm)	Ti (46 µm)	130 000 s	190 $\frac{\text{counts}}{\text{s}}$
Al (550 µm)	Si (390 µm)	Ti (23 µm)	580 000 s	66 $\frac{\text{counts}}{\text{s}}$

Table 4.3.: The exposure times for the different combinations of 3 materials for **100 000 counts** in all selected channels. In each measurement an additional silicon sheet of **390 µm** is used for the base absorption. The exposure times shaded in gray are exceeding the stability limit of our measurements.

bars. The measurement which works best is the one where pure aluminum is measured.

The element detection is also applied to a more biologically relevant problem, i.e. the detection of different salts in aqueous solutions. The different solutions are measured with cuvettes shown in figure 4.15. The two salts measured are sodium chloride ($Z_{Na} = 11$ and $Z_{Cl} = 17$) and calcium chloride ($Z_{Ca} = 20$). Each series consists of the measurement of five cuvettes. The first cuvette is empty in order to measure the absorption of the cuvette and the titanium of the base absorption. The concentrations and the densities of the second to the fifth cuvettes are described in table 4.4. In case of calcium chloride the calculation of the concentration must consider the fact that the solution is made from dihydrated calcium chloride salt ($CaCl_2 + 2H_2O$). The salt concentrations are selected to give a comparable overall absorption in all three solutions. The exposure times of the different measurements are listed in table 4.5 The third solution is a 1:1 mixture of the two first ones. A filled cuvette with the titanium sheet is shown in figure 4.29.

In figure 4.30, the gray level of two dimensional images of the cuvettes is adjusted to represent the measured values for sodium chloride and calcium chloride respectively, shown as separate images. The sodium chloride solution gives an incorrect result. For both other solutions the best measurements are selected for the illustration. In figure 4.31 all results are presented in two diagrams for both salts in the form of measured values versus actual values. All measurements should lie on the diagonal line.

The error bars are calculated for each measurement separately. As a base, the error

	ρ_{H_2O}	c_{NaCl}	ρ_{NaCl}	c_{CaCl_2}	ρ_{CaCl_2}
second cuvette	$991\ \frac{kg}{m^3}$		-		-
third cuvette	$893\ \frac{kg}{m^3}$	$299\ \frac{g}{l}$	$270\ \frac{kg}{m^3}$		-
fourth cuvette	$936\ \frac{kg}{m^3}$		-	$186\ \frac{g}{l}$	$175\ \frac{kg}{m^3}$
fifth cuvette	$914\ \frac{kg}{m^3}$	$150\ \frac{g}{l}$	$135\ \frac{kg}{m^3}$	$98\ \frac{g}{l}$	$90\ \frac{kg}{m^3}$

Table 4.4.: The concentrations c and densities ρ of the different components of the four solutions used in the salt measurements.

cuvette filled with	exposure time	count rate
empty	9400 s	$3000\ \frac{counts}{s}$
H_2O	13 000 s	$1700\ \frac{counts}{s}$
H_2O + NaCl	24 000 s	$610\ \frac{counts}{s}$
H_2O + $CaCl_2$	27 000 s	$510\ \frac{counts}{s}$
H_2O + NaCl + $CaCl_2$	24 000 s	$590\ \frac{counts}{s}$

Table 4.5.: The exposure times for the different combinations of the solutions for 100 000 counts in all selected channels. In each measurement an additional titanium sheet of 23 µm is used for the base absorption.

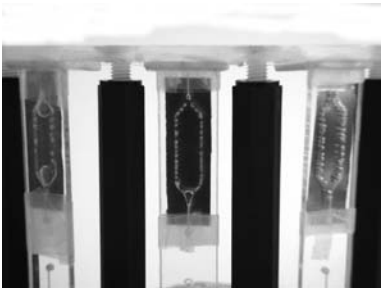

Figure 4.29.: Filled cuvette fixed in the holder. Behind the cuvette a titanium sheet of 23 µm is glued. In the liquid air bubbles are visible. Both holes of the cuvette are sealed to avoid liquid evaporation.

estimation of the silicon measurements from before is used. This error is corrected to account for the two different conditions of matrix $\boldsymbol{B}$. In the salt measurements the condition has the average of $\kappa(\boldsymbol{B}) = 412$. Also in this case the error estimation $\frac{|\Delta\varphi|}{|\varphi|} \approx 2.6$ based on (4.7) is too pessimistic. This gives the relative vectorial error of $\Delta\varphi = 0.71 \cdot \frac{\kappa(\boldsymbol{B}_{\text{salt}})}{\kappa(\boldsymbol{B}_{\text{metal}})} \cdot \|\Delta\varphi\| = 0.23 \cdot \|\Delta\varphi\|$.

This simplified model for the error bar calculation seems to underestimate the errors. For the calcium chloride only half of the results are within the error bars, for sodium chloride even only 25 %. An error estimation series would be needed to verify the error in the salt measurements. Only two compounds are detected in the measurements with aqueous solutions instead of three as in the measurements determining the error. Additionally other materials are searched especially compounds that are no pure elements anymore. Because of these causes the simplified error model seems not to be accurate enough and underestimates the error bars.

In contrast to the two other detections campaigns mentioned earlier in this work, the salt detection only works poorly. One issue of this measurements series is the way water is accounted for. The hydrogen contribution is for example neglected. The point of 50 % scattering and photoabsorption of hydrogen is at 2.6 keV and therefore the scattering is more important in the selected energy range. Hydrogen is very light and it makes only a small fraction of the weight in the solutions. Because of this approximation should not strongly influence the quality of the results. Chlorine on the other side is in the photoabsorption region but is part of both salts. Consequently its absorption characteristic does not help distinguishing the two salts.

The water is taken into account for the calculation of the mass-absorption coefficient of the two salts. For the calculation of the salt concentration the change in the water density is ignored. The measurements are made relative to pure water and therefore the change in water density is not so important.

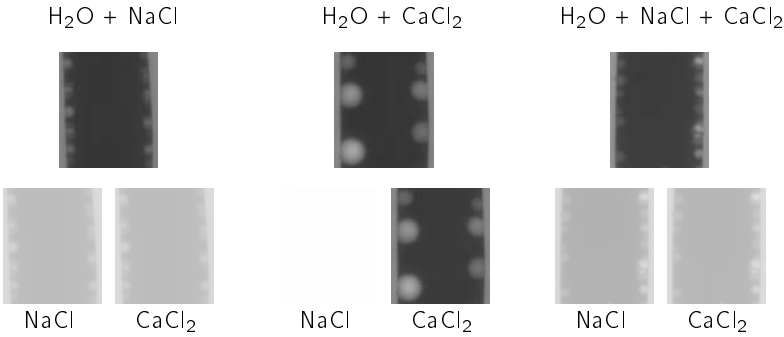

Figure 4.30.: The element sensitivity is simulated with two dimensional images. In the first row the actual X-ray images of the three solutions are shown. In the second row the images are adjusted with the results of the element sensitive measurements.

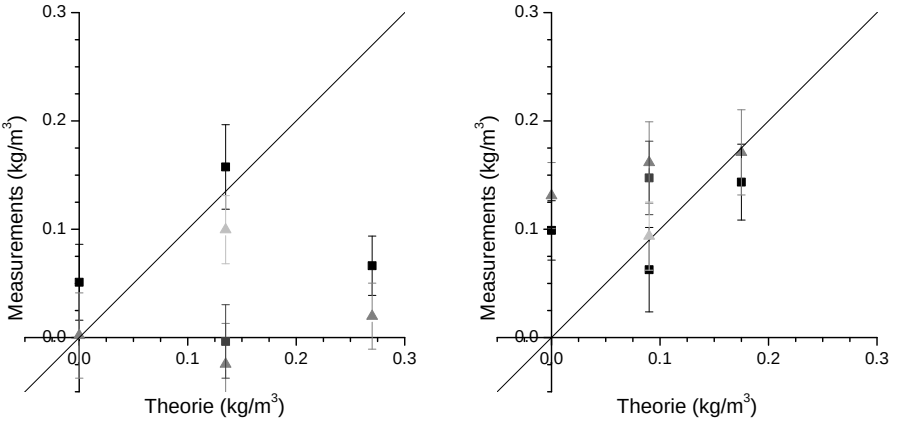

(a) NaCl (b) $CaCl_2$

Figure 4.31.: All measurements are separated into the two salt parts. For both the theoretical values and the measurements are compared. All values should lie on the diagonal line. The two different shapes indicate th two different references.

4.7. Quality of measurements

The quality of the measurements is a major issue in this work. The exploited physical effects are so small that the measurements need to be of very good quality to detect those effects. Many actions are undertaken to potentially increase the quality. These actions are explained in this section.

4.7.1. Quality considerations on the beam

The X-ray source emits photons in all directions. The design of the source gives a preferred direction. The beam forms a primary cone with an opening angle of 39° from the specification of the source. All materials irradiated with X-rays will emit fluorescence photons and act as scatterers. The fluorescence photons are emitted in all directions. Those effects can be counteracted by minimizing the radiation which hits any material. Apart from the design of the shielding the most important effect can be achieved by positioning the sample as closely as possible to the source. In figure 4.32 this concept is visualized.

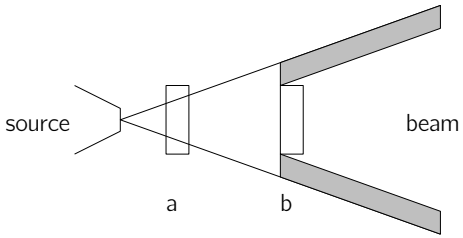

Figure 4.32.: The object in position a is near enough to the source. In position b the grayed area has full intensity behind the object. This leads to a high amount of fluorescence from the shielding, sample holder, etc.

The effect of the sample position on the spectra is shown in figure 4.33. The complete beam path is around 50 cm. For this diagram the object is placed at four positions in the first 7 cm. When the sample is further away from the source, there is an effect of broadening and a strong increase of lower energy photons together with low energy fluorescence peaks.

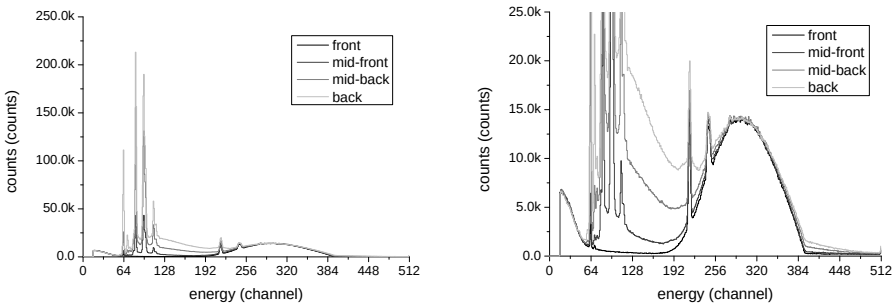

Figure 4.33.: The position of the object has an impact on the measurement. The impact stems from the fact that the radiation can pass beside the object if it is further away from the source. The second graph is a zoom of the first one.

4.7.2. Source

The source has a problem with the linearity at low currents. Below 4 keV the current decreases faster than it should which is shown in figure 4.34. This is one reason why the current cannot be adapted between several measurements. Ideally the current would be adapted for each absorption potential of each object and therefore always maximize the count rate.

The other reason which is the stability of the source over a power cycle has even more consequences. Over a power cycle the source can change the radiation power of more than 10 % (see figure 4.35). This has the consequence that both exposures of an absorption measurement must be done without a power cycle in between. This can be done with the two holders shown in figures 4.13 and 4.16. With those holders the samples can be changed while the X-ray source is in operation. Only one sample can be placed in all other holders. To change the sample the instrument must be opened and the source stopped. The downside of this measurement method especially for the first holder is the necessity for a base measurement for all samples.

4.7.3. Detector

The spectrometer has several properties which can influence the quality of the measurements.

First the major noise source for short measurements is shot noise. This can be

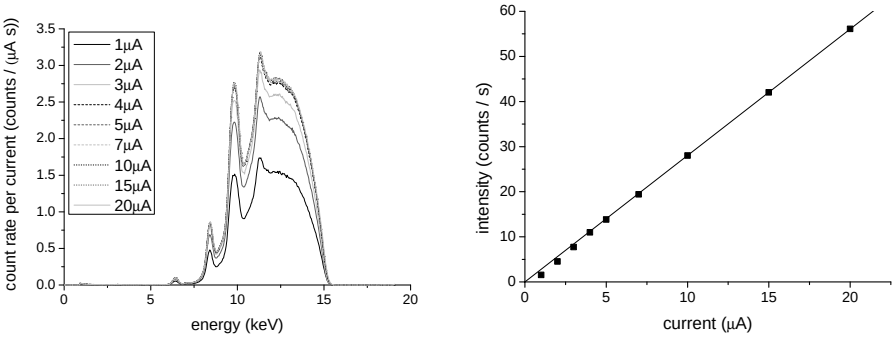

Figure 4.34.: The source loses its linearity below **4 μA** electron current. In (a) the complete spectra are shown, in (b) the average counts per channel in the selected energy range are plotted.

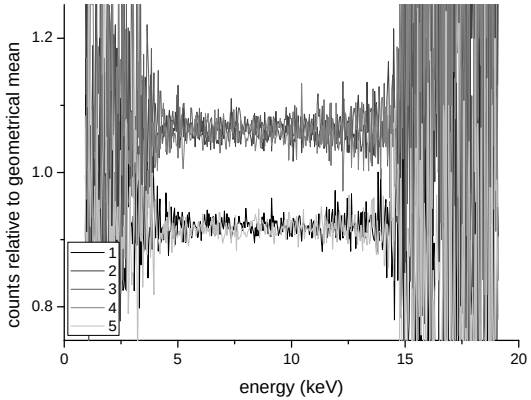

Figure 4.35.: The source is not stable over a power cycle. Five measurements are compared to their geometrical mean.

seen in figure 4.36. In this diagram the jitter of nine measurements is displayed. All measurements are made with 1100 µm of titanium in the beam and with an acceleration voltage of 40 kV and a tube current of 5 µA. The time to peak is 25.6 µs and the exposure time is 1001 s. Those nine measurements are averaged. Then the square root of this average is compared to the standard deviation of the measurements. As the two are in the same order of magnitude shot noise is the primary noise at this exposure time.

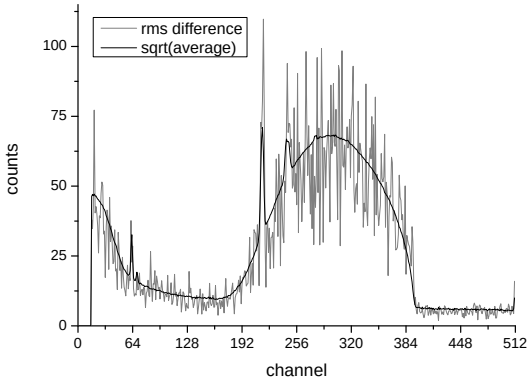

Figure 4.36.: The average noise of several measurements is in the order of the square root of the signal.

The finite thickness of the silicon diode for the detection of the X-ray photons limits the maximal energy that can be detected with this spectrometer. The diode has a thickness of 680 µm. The absorption characteristic of silicon at this thickness is shown in figure 4.37. This diagram explains why the energy used in this work is limited to 40 keV. Above this energy the absorption becomes too small.

Even at 40 keV the absorption is already quite low. The spectra measured with an acceleration voltage in this region will have a different shape than the actual spectrum. Such a spectrum is shown in figure 4.38 together with a corrected spectrum. This effect can be neglected when the absorption is measured. The absorption is detected by the ratio of two measurements. The probability for measuring the photons at a specific energy will be the same in both measurements.

The same is true at the lower end of the energy spectrum. At this end the transmission capability of the two beryllium windows of the source and the detector are critical.

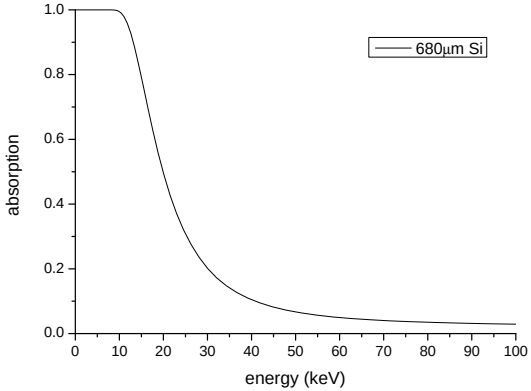

Figure 4.37.: The Amptek X-123 spectrometer has a silicon diode with a thickness of 680 µm. The graph shows the absorption characteristic of this diode.

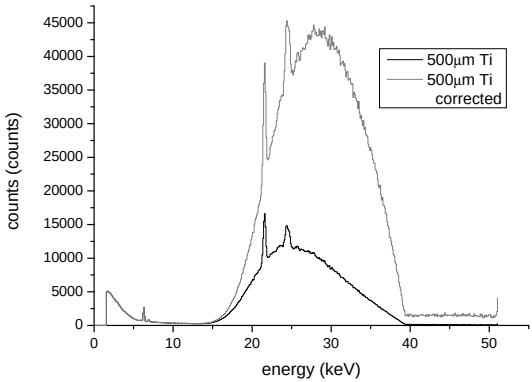

Figure 4.38.: The absorption of the silicon diode in the sensor is decreasing with the energy. To get the actual energy spectrum the absorption characteristic of the diode must be used to correct the measured spectrum.

Both transmission characteristics and the combination are shown in figure 4.39. From this diagram the lower energy limit can be put around **5 keV**. Additionally the absorption of around **0.5 m** of air would also be important to set this limit. The air becomes transparent around the same energy as the beryllium windows.

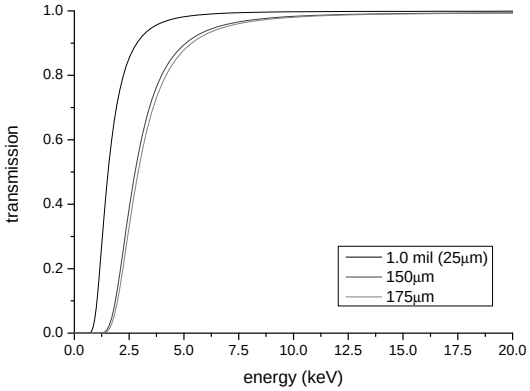

Figure 4.39.: The transmission of **1 mil (25 µm)** thick beryllium windows as used in the Amptek X-123. The second line with **150 µm** is the exit window of the source. The third line is the combination of both and shows the complete transmission characteristic of source and detector.

4.7.3.1. Non-linearity of the sensor

One of the major issues of the detector for quality is the detector linearity. As most of the measurements are done at different count rates this linearity is vital for a correct solution. The linearity is limited by the time the detector needs to handle one event. In this time no other event can be treated (so-called dead-time effects). In the case when two or more events arrive in this time slot two outcomes are possible. First the two or more event cannot be separated and the detector counts one event at the sum of the energy of all contributing counts. In the other case the system can detect that two or more events happened but cannot separate them. In this case the system discards all these events.

Two pulse detections are made in parallel. One is the fast detection with a non-parameterizable rise-time of **400 ns** [3]. From this time and the fast count rate in the detector the estimated actual count rate can be calculated

$$R_{\text{in}} = \frac{R_{\text{fast}}}{1 - R_{\text{fast}}\tau_{\text{fast}}}$$

where R_{in} is the count rate hitting the detector diode, R_{fast} is the fast count rate in the detector, and τ_{fast} is the dead time of the fast counter (**800 ns**). If two or more photons hit the detector within the dead time τ_{fast} these two or more events cannot be separated by the detector. It is not possible to directly measure R_{in} with this detection setup.

The other pulse detection is the slow one. Its rise time is parameterizable. In this discussion only the case with enabled pile-up rejection is considered. In this case the detector can identify double counts if the events are spaced by more than the pulse pair resolution of the fast channel of **600 ns**. This leads to the following equation

$$R_{\text{out}} = R_{\text{in}} \cdot \exp\left(-2.375 \cdot R_{\text{in}} \cdot \tau_{\text{int}}\right) \tag{4.10}$$

where R_{out} is the slow count rate in the detector and $\tau_{\text{int}} = \tau_{\text{rise}} + \tau_{\text{flat top}}$ is the integration time which is the sum of the rise time and the flat top time of the filter. The characteristics of the different integration times are shown in figure 4.40.

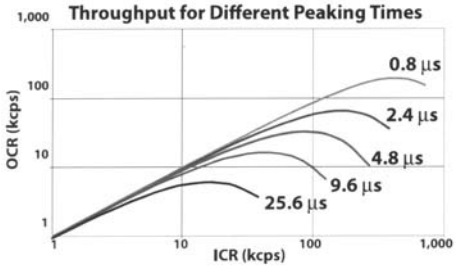

Figure 4.40.: The ICR (input count rate) and the OCR (output count rate) are not strictly linear to each other. The range of their linearity is dependent on the peaking time and hence on the precision.

The measurements are made with an integration time (time to peak) of **2.4 µs**. For this integration time and for a limit of the error on the counting of maximal **2 %** the maximal counts are limited to **3267.4** $\frac{\text{counts}}{\text{s}}$ (see figure 4.41).

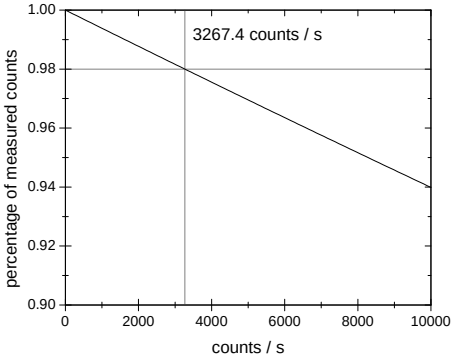

Figure 4.41.: The error due to saturation in the detector in function of the count rate. This diagram is generated from equation (4.10).

Without the pile-up rejection the quality of the spectrum would further decrease because double events would distort it.

The effect of saturation can be seen in figure 4.42. The saturation factor s is applied to the absorption calculation $A' = A \cdot s = \frac{I_2}{I_1} \cdot s$. The illumination with a higher photon flux will have higher saturation and therefore the calculated absorption will be lower. This is shown as a drop in high energies in a double logarithmic representation.

The effect of this non-linearity on the spectrometer is the limit of the count rate in the spectrometer at around $3200\,\frac{\text{counts}}{\text{s}}$.

4.7.3.2. Incertitude regarding the energy

The calibration of the spectrometer is described in section 4.3.1.1. An incertitude on this calibration will be critical in case of a matrix $\boldsymbol{B}$ based on tabulated data. From equation (2.8) it can be deduced that the incertitude of the energy will be dependent on the atomic number for the incertitude of the absorption. Therefore the elemental distribution will be influence by this incertitude.

The calibration loses its importance when all the measurements including reference measurements are realized with the spectrometer. In this case the channel number is used without information about the absolute energy. The energy shifts in the spectrometer over different measurements are more difficult to compensate. The shift in channels is shown in figure 4.43. The peak position ($L\beta_1$ peak of tungsten) is calculated by the position of the maximum of a Gaussian curve over seven values around the maximum. The algorithm for this fit is explained in section A.4. All 19 measurements are done with $390\,\mu\text{m}$ of silicon in the beam path, an acceleration voltage of $15\,\text{kV}$ and

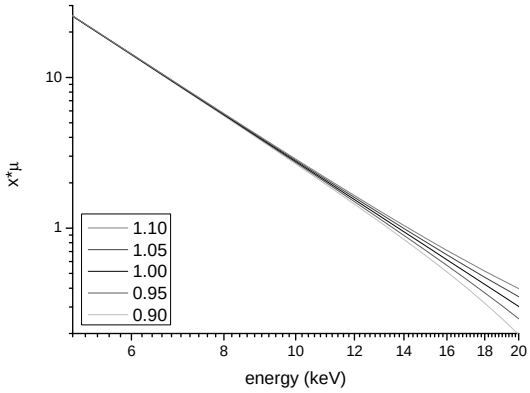

Figure 4.42.: The lines with a saturation factor below 1 indicate the effect on the line by a slightly saturated base signal when calculating $x \cdot \mu$. The lines with a factor above 1 show the case of a base signal with double counts in the spectrum.

a current of 9 µA.

The peak position cannot be compared with measurements obtained with other absorbing objects in the beam path. The absorption distorts the peak and without a correction the measured peak position would be different. Because of this all the calibrations are made without an object in the beam path and therefore close to saturation.

The energy stability of the different measurements is sufficiently high and therefore no additional measures must be taken.

4.7.3.3. Time to peak

The time to peak is one of the integration parameter in the spectrometer. The quality of the energy value increases with the length of the time to peak. This increase can be seen in figure 4.44 and in more detail in 4.45. The tungsten peaks visible in those figures get higher and thinner with the increase of the time to peak. The height and full width at half maximum (FWHM) are shown in figure 4.46.

At the same time the energy calibration must be redone. It is not possible to reuse a calibration obtained with another time to peak parameter, since changing this parameter results in a shift of the energy value of the channels. This effect is very strong for time to peak values between 0.8 µs and 2.4 µs.

The increase in quality at higher time to peak values leads to a decrease in the throughput. In figure 4.47 the acceptance ratio is presented. The acceptance ratio

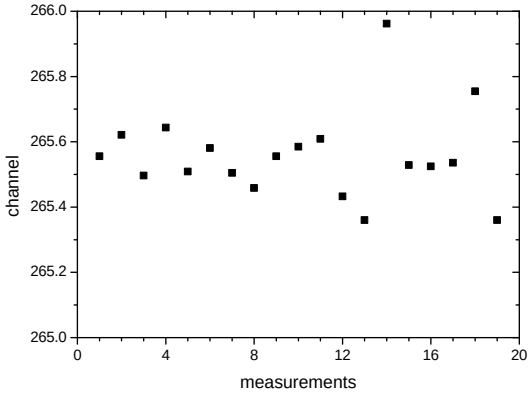

Figure 4.43.: The $L\beta_1$ peak of tungsten and its shift in position over 19 measurements.

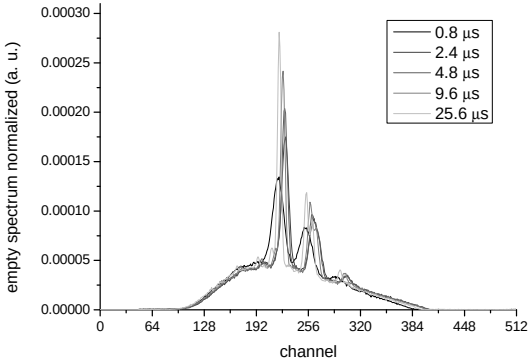

Figure 4.44.: With the time to peak parameter three properties of the spectra change. First, the the peak energy slightly shifts. Second, the peak height increases and the width decreases. The last two effect are the increase in precision with the increase in the time to peak. This diagram is normalized by the count rate.

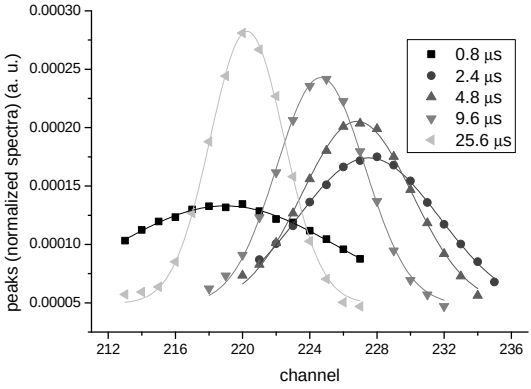

Figure 4.45.: 15 points around the maximum are taken for five time to peak parameters and their tungsten $L\alpha$ peak and a Gaussian fit is made over them.

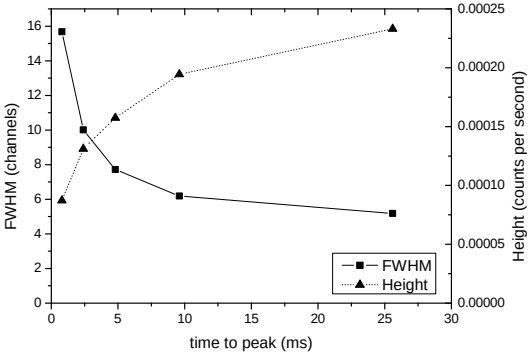

Figure 4.46.: A decreasing time to peak will broaden the peaks. As the total number of counts stays the same the peak height must decrease at the same time.

is the ratio between the fast count rate and the slow count rate. Between those two count rates the pile-up rejection algorithm is applied. The measurements are made with an empty beam path at a tube voltage of 15 kV and a tube current of 1 µA. The exposure time is 101 s.

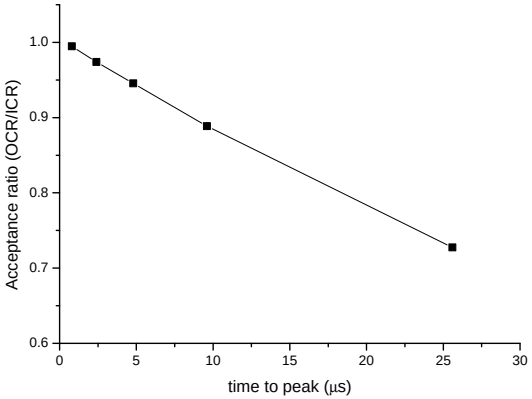

Figure 4.47.: The throughput decreases when the time to peak increases. The probability of a double event rises at the same time and therefore the acceptance ratio decreases.

The selected time to peak in this work was 2.4 µs mainly to increase the possible count rate as discussed in a section antecedent and the energy quality has only second priority.

4.7.4. Long-term stability of the complete system

The long-term stability of the complete system is characterized by the Allan variance [28]. The standard variance is calculated with the mean value

$$A = \frac{1}{N} \sum_{i=1}^{N} x_i$$

for N samples of x and the standard variance of x is

$$\sigma^2 = \frac{1}{N-1}\sum_{i=1}^{N}(x_i - A)^2$$

The factor $N-1$ is due to the fact that the same data is used for the calculation of mean value and of the variance.

Because the spectrometer has a photon counting system the integration in time can be done in the spectrometer or outside with the same result. Therefore a series of measurements with a constant duration and the source continuously radiating can be used to simulate different integration times. Such a series is presented in figure 4.48 in which the exposure time is $10\,\mathrm{s}$ for each measurement. Originally, the series also include a low number ($< 0.8\,\%$) of measurement points, which are clearly outside of the expected range. These errors are caused by two different failure modes of the spectrometer: In one case all events are discarded and a count rate of $0\,\frac{\mathrm{counts}}{\mathrm{s}}$ is measured. In the other the lower limit is ignored and a count rate of around $5200\,\frac{\mathrm{counts}}{\mathrm{s}}$ is measured with a non-negligible saturation. Those measurements are deleted from the series since in principle they could be identified and prevented.

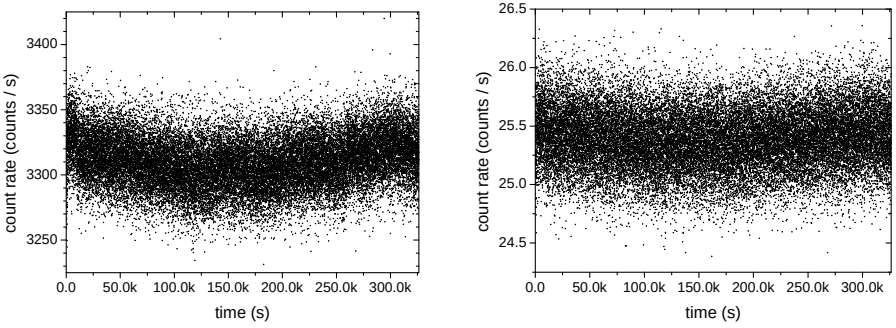

(a) all channels (b) calculation channels

Figure 4.48.: In (a) the signal of the integral over all channels in the measurement range (see section 4.4.2) is shown. In (b) the integral of the channel used in the calculation are shown. All measurements are obtained with an exposure time of $10\,\mathrm{s}$.

All multiples of the exposure time can be simulated from this series. For all these simulated lengths the variance can be calculated. Such a variance is called an Allan variance. First the mean value becomes

$$A_s(k) = \frac{1}{k}\sum_{n=1}^{k} x_{(s-1)\cdot k+n}$$

with s the number of subgroups and k the number of elements in one subgroup. The subgroups simulate the desired length in time. From this mean value the Allan variance in time can be calculated

$$\sigma_A^2(\tau) = \langle \sigma_A^2(k) \rangle_t = \frac{1}{2m}\sum_{s=1}^{m} (A_{s+1}(k) - A_s(k))^2$$

where $\tau = k \cdot \Delta T$ is the integration length and m the numbers of subgroups.

The Allan variance of the spectra's integral is shown in figure 4.49. The first part is the region where the shot noise is the dominant noise. After about $10\,000\,\mathrm{s} = 2.8\,\mathrm{h}$ the quality of the measurement decreases. Other noise sources then become more important than shot noise. This other noises could be an instability in the X-ray source or a shift in the detector.

The fit follows the equation

$$\sigma_A^2(\tau) = c_1 \cdot \tau^{-1} + c_2 \cdot \tau^{1.33}$$

This equation combines two different noises. The c_1 is the shot noise part which follows $\sigma = \sqrt{N}$. The second noise is characterized with the parameter c_2 and follows $\sigma = N^{0.66}$.

From those results the maximal quality of a measurement will be at an exposure time of $10\,000\,\mathrm{s}$. The time between the measurements is not negligible and therefore the value of the optimal exposure time is to be considered as an order-of-magnitude estimation.

4.7.5. Incertitude in length or density of the object

The matrix $\boldsymbol{B}$ can be constructed from the mass-absorption coefficients $\frac{\mu}{\rho}$ from reference measurements as described in equation (4.5). In this case there is an incertitude on those mass-absorption coefficients $\frac{\mu}{\rho}$. The coefficients are calculated from the measured length-absorption coefficients $\tau = x \cdot \rho \cdot \frac{\mu}{\rho}$ and therefore they will have the incertitude propagated from the thickness x and the density ρ. Those two parameters can be combined in the integrated density $\varphi = x \cdot \rho$ with an uncertainty ϵ_φ. This uncertainty will further propagate from the mass-absorption coefficient $\frac{\mu}{\rho}$ to the matrix $\boldsymbol{B}$.

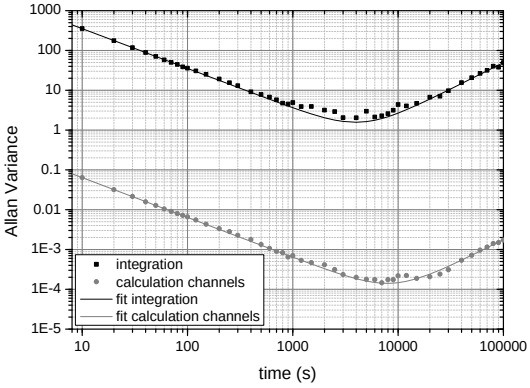

Figure 4.49.: The Allan variance for both the series presented in figure 4.48. The fits combine the shot noise and other noise sources.

As this uncertainty is a constant factor over the energy, no effect on the distribution of the integral density φ of the result from equation (4.6) can be seen. The result will have an additional uncertainty of $\frac{\epsilon_{\varphi_R}}{\varphi_R}$ on the resulting φ_M. The factor $\frac{\epsilon_\varphi}{\varphi}$ is represented as a shift in a double logarithmic graph displaying mass-absorption coefficient versus energy (as for example in figure 4.21).

4.7.6. Channel selection

In the section 4.4.2 an energy range is selected. The main interest of this section is to analyze if all energies or the respective channels have the same quality. The hypothesis is to eliminate the worst channels in order to increase the quality of the measurement. At the beginning a set of **101** channels is selected. At each step the worst channel of this set for the calculation of the elemental distribution is omitted. The worst channel is determined with the following step. The largest vectorial distance to the correct result is searched by omitting one channel after another in the series. The result with the largest vectorial distance to the correct result gives the worst channel. At the end all channels get a number from **0** (best) to **96** (worst).

This procedure is repeated over five measurements. The count result of each channel is summed and a histogram is made from this sum. The histogram is shown in figure 4.50. There are hardly any channels at both extremes. This indicates that no channel is particularly good or bad over several measurements. Therefore no selection of the channels can be made.

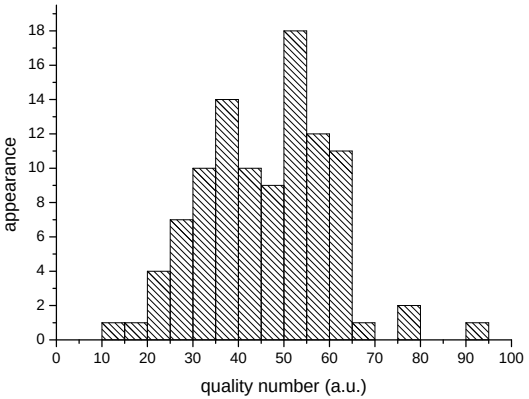

Figure 4.50.: The distribution of the quality number of the channels. The grouping around the center shows that the quality of the channel is similar. No improvement of the signal by selecting specific channels can be made.

5. Conclusion

In this thesis, an instrument for microCT measurements and for element sensitive X-ray imaging was developed.

The microCT capability was verified by examining various samples at the microscopic level. The resolution of the system was found to be approximately $10\,\mu\mathrm{m}$.

The measurements carried out in this thesis indicate that the novel, element sensitive method works. Composite samples made of aluminum and silicon could be distinguished contrary to conventional X-ray imaging.

The advantage of this method compared to other X-ray methods to detect the elemental composition is the ability to detect multiple elements from a single measurement. These measurements give the resulting densities for the multiple elements simultaneously. Also the results are absolute for each element. This was successfully demonstrated with the detection of three elements (aluminum, silicon, and titanium) in one measurement.

The quality of the measurements is however still an issue. For a single measurement, the error on the result is in the order of the result. The data quality is dependent on the counts per channel, which itself depend on two parameters. First the counts are proportional to the exposure time. There is an optimal exposure time at which the quality is maximal. For shorter exposure times the shot noise is higher and for longer exposure times other noise sources start to dominate. The optimal exposure time is where these other noise sources become more prominent than shot noise. For some of the measurements in this work, an exposure time longer than the optimum time was used; in this case, the data quality must then be increased by one of the following methods. The accuracy of the result can be further improved by averaging over a large number of measurements. This is less efficient to increase the quality than an extension of the exposure time. Therefore this is only reasonable when the exposure time cannot be increased anymore. Another method is to increase the numbers of counts per channel.

One potential path to increase the count rate in the desired channels is to narrow the measured spectrum. The shape of the spectrum changes in important manner by samples with different absorption capabilities. This is due to the strong dependence of the absorption on the energy. Therefore the width of the spectrum can only be narrowed in a limited way. Because of this the optimal spectrum shape is also dependent on the object, especially of the absorption properties of the object.

Another path to increase the count rate is a stronger beam intensity. This also increases the probability of double events. This effect can perhaps be corrected by an algorithm. The correction of the detected double events should be a constant factor over the whole spectrum. Undetected double events are much more difficult to compensate because they distort the spectrum. Fortunately only a small fraction of the double events remain undetected with the current spectrometer.

The number of double events could be decreased by a faster spectrometer. The spectrometer used in this work is optimized for fluorescence measurements and therefore the energy resolution is more important than the linearity of the count rate. Another solution to the problem of the count rate is the measurement with a monochromatic beam. In this case the detector does not need to measure the energy of each individual photon. The deposited energy is enough. From the deposited energy the number of photons can be calculated. With a higher quality spectrometer it could also be possible to make longer measurements until noise sources other than shot noise become important.

If the most important noise of the signal measurement is shot noise then the following consideration of the result quality can be done. The signal quality will increase by the square root of the count rate increase if the exposure time is maintained. The result quality is further proportional to the signal quality. For example if the count rate could be increased by the factor of 100 the signal quality will increase by the factor of 10 as well as the result quality.

The spectroscopical measurements are made with a single spatial channel. The extension to a one- or two-dimensional array would be possible with the devices described in section 4.3.2. With such a device an image could be generated with limited or no mechanical scanning which would represent an important gain in measuring speed. From there an extension to a tomographical measurement is straightforward and would generate two- respectively three- dimensional distributions for each elements. Such tomographical images would considerably increase the applications of this method. Besides the known advantages of tomographical images as the visualization of the object's inner structure this method could determine the physical density without any a priori knowledge. Without tomography the thickness must be known to determine the absolute density.

The salt measurements with aqueous sodium chloride and calcium chloride solutions are not completely convincing. In this case new reference measurements with pure elements could be interesting. In general the selection of elements was strongly limited. In addition to the limitations imposed by the selected energy range and by the condition of sufficient distinguishability, only elements, which could be measured in pure form could be selected. The salts are an exception. They are possible because their stoichiometric composition is fixed. The salts are measured as aqueous solutions and therefore the concentration (density) is variable up to a limit. Also the combination

of different salts is possible. For the two elements sulfur and phosphorous reference data could not be measured. The powder form of these two elements resulted in non-reproducible results, because of the uncertainty in effective sample density due to the unstable setup.

The theory of this method is only based on photoabsorption as described in equation (2.7). This equation is a simplified model. The equation (2.8) represents the reality better than the simplified model but it is still not adequate enough. Additionally to better characterize the photoabsorption, the other attenuation factors could also be added to represent the reality more exactly. The combined attenuation factor can be seen in equation (2.1). The better knowledge of the behavior of the mass-absorption coefficient could be used to optimize the calculation.

There is the potential that a better algorithm can be found for the calculation. This could help to increase the quality of the result without further improving the signal quality.

Based on better results and perhaps on a more accurate theory the potential for the different image uses could be better determined. Especially in the medical domain where the ratio between the signal quality and the deposited energy is very important.

In a setup like the one presented in this work this method has several potential use scenarios. For example the case of the aqueous solution could be extended and the concentration of several elements could be detected on the fly. Also when layer are deposited on other materials the thickness could be determined.

Additional use scenarios are possible with a one- or two-dimensional array . First of all the direct identification of different tissue, cells, or even molecules is imaginable. Here the emphasis would lie in the identification of unhealthy tissue such as cancer tissue. This could be possible due to the different elemental distribution in those tissues. In the case of cells or molecules the functional knowledge within biological processes could benefit from this method. Moreover the potential use of lighter tracers must be mentioned. With such tracers it could be easier to cross the blood-brain barrier. This work has great potential which with further development could lead to some interesting applications as shown in those last examples.

A. Appendix

A.1. File definitions

Several file formats have been defined to save specific informations from the CTControl program. The data type of the various formats are described in table A.1. The last two data types are deprecated and are replaced by data type 1 plus additional parameters in the file header.

data type	description
1	unsigned integer 16 bit
2	double precision IEEE-754 (64 bit)
3	boolean
4	single precision IEEE-754 (32-bit)
10	one dimensional list of unsigned integer 16 bit (deprecated)
11	two dimensional list of unsigned integer 16 bit (deprecated)

Table A.1.: Description of the data types used in this work.

Three additional file formats are not described in the sections below. The first format is the comma-separated values (CSV) files. This format is very simple as two values are separated by a semicolon and a new line by a carriage return and a line feed, which is the format used by Microsoft Excel.

Secondly, images are stored in tagged image file format (TIFF) as described in [1]. These TIFF files are written by the library LibTIFF[1].

The third format is visualization toolkit (VTK) file format. It is used to store three dimensional models of a tomography. The files written in this format follow the specifications in [5]. CTControl can only read files written by itself. The files must have the same layout and some options cannot be changed.

[1] The library can be found under `http://www.remotesensing.org/libtiff/`

A.1.1. RAW 2D images

The two dimensional raw image data is stored in the file format defined in this section. The header structure is described in table A.2.

Name	Size	Units	Comments
Version	int (4 bytes)		in version 2 and higher
DataType	int (4 bytes)		
Width	int (4 bytes)	in pixels	
Height	int (4 bytes)	in pixels	
Angle	double (8 bytes)	in radian	
ExpTime	double (8 bytes)	in seconds	in version 2 and higher
Voltage	int (4 bytes)	in kilovolt	in version 2 and higher
Current	int (4 bytes)	in microampere	in version 2 and higher

Table A.2.: The header of the RAW 2D image. Some fields are only available in the version 2.

The actual file format is version 2. The first version has no particular identification. Starting from version 2 an identification is added to the version field. To the version number 0x8000 0000 is added. The data types are described in table A.1.

Directly after the header the data is stored. The length of each element is determined by the data type and can vary from 1 bit to 64 bit. The number of elements is the product of width times height. The pixels are written row after row starting in the top left corner.

A.1.2. List file

This format saves a list of raw images. The header of the file is described in table A.3 and the header of each element of the list in table A.4

The rest of each element is the data fields. The data fields are organized as in the RAW 2D images described in the previous section. The length is dependent on the data type which is defined in table A.1.

Name	Size	Units	Comments
Version	int (4 bytes)		
DataType	int (4 bytes)		
Iteration	int (4 bytes)		in version 4 and higher
ExpTime	double (8 bytes)	in seconds	in version 5 and higher
Voltage	int (4 bytes)	in kilovolt	in version 5 and higher
Current	int (4 bytes)	in microampere	in version 5 and higher
XRay	int (4 bytes)	true/false	in version 5 and higher

Table A.3.: The header of the list file. Some fields are only available in higher version of the file.

Name	Size	Units
Width	int (4 bytes)	in pixels
Height	int (4 bytes)	in pixels
Angle	double (8 bytes)	in radian

Table A.4.: This header precedes the data part of each element.

A.1.3. VRAW 3D models

The volume raw data stores the information from a reconstruction. The file header is described in table A.5.

After the header the data fields follow. The number of data fields is the product of width times depth times height. The length is dependent on the data type defined in table A.1. The data is aligned in the order shown in the figure A.1.

A.1.4. Spectral files

The spectral information is stored in an extensible markup language (XML) file. The different fields are described in table A.6.

Name	Size	Units
Version	int (4 bytes)	
DataType	int (4 bytes)	
Width	int (4 bytes)	in pixels
Depth	int (4 bytes)	in pixels
Height	int (4 bytes)	in pixels
ExpTime	double (8 bytes)	in radian
Voltage	int (4 bytes)	in kilovolt
Current	int (4 bytes)	in microampere
XRay	int (4 bytes)	true/false

Table A.5.: The header of the volumetric raw (VRAW) file.

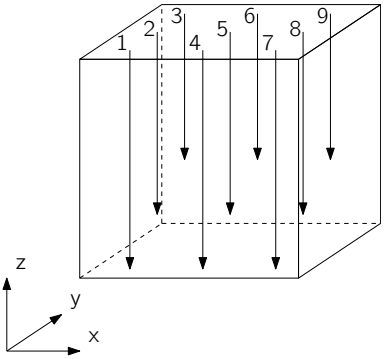

Figure A.1.: The alignment order in the VRAW file. The arrows symbolize the sequence of the data and the number the sequence of the arrows.

Tag	Description	Version
file_version	version number of the file	0.1
start_time	time when the measurement has started	0.1.1
channels	number of the channels	0.1
channel_i	ith channel of the spectrometer	0.1
enable	if X-ray is enabled or disabled	0.1
voltage	acceleration voltage in kilovolt	0.1
current	current in microampere	0.1
FPGA	version of FPGA in Amptek spectrometer	0.1
firmware	firmware of Amptek spectrometer	0.1
serial_number	serial number of Amptek spectrometer	0.1
status_device_indicator	type of spectrometer	0.1
setFastThreshDone	indicates if fast threshold is active	0.1.6
setInputOffsetDone	indicates if input offset is active	0.1.6
board_temperature	board temperature in degree Celsius	0.1
fast_count	number of input counts	0.1
slow_count	number of identified event counts	0.1
accumulation_time	detection time in seconds	0.1
coarseGainIndex		0.1.2
fineGain		0.1.5
fineGainReg		0.1.6
timeToPeakIndex	slope of integration filter	0.1.3
slowThreshold		0.1.4
fastThreshold		0.1.4
decimation		0.1.6
flatTop		0.1.6
PUREnable		0.1.6
timeRatio	ratio between the lapsed time and measuring time	0.1.6

Table A.6.: The description of the spectral files. A tag is available since the version indicated in the table.

A.1.5. BMP

BMP is a standard image storing file format under Microsoft Windows. First the two headers are written in the file. After these two headers a color table can be added. In the table the colors are all four bytes long with the part: reserved (0), red, green, and blue. Following those parts the data is stored. Each line has to be padded to a length of a multiple of **4** bytes.

Name	Size	Value
Identification	WORD (2 bytes)	19778 (BM)
Size	DWORD (4 bytes)	width $\times$ height $\times$ 3 + 54 (e.g. for 24 bpp)
Reserved	DWORD (4 bytes)	0
Offset of image	DWORD (4 bytes)	54 (without color table)

Table A.7.: The 14 first bytes from the bitmap header with the corresponding data.

A.2. Simulation

The backprojection algorithm is tested with different simulations. The first two tests are shown in figure A.2. They generate a single point and concentric circles in the two dimensional case. In three dimensions the patterns are extended in the z direction and give therefore a line and concentric cylinders. After this two very basic tests a Shepp-Logan head phantom [32] is used. The practical implementation used is from Kak et al. [18]. The backprojection of the head phantom is shown in figure A.3. In this figure an artifact called partial volume effect is visible. This artifact is explicated in the next section.

The Shepp-Logan head phantom is a collection of ellipses respectively ellipsoids, in the image space, which together represents a head. The ellipses are for the two dimensional case and the ellipsoids for the three dimensional case. This image has to be projected to the detector space first to test the backprojection. Because the Radon transformation is linear each of these ellipses respective ellipsoids can be transformed separately and afterwards summed in the detector space.

For simplicity reasons the projection is only considered in the parallel beam case. Additional steps must be taken for the fan and respectively cone beam case.

Name	Size	Value
Second header size	DWORD (4 bytes)	40
Width	LONG (4 bytes)	width
Height	LONG (4 bytes)	height
Planes	WORD (2 bytes)	1
Bit per pixel	WORD (2 bytes)	24 (e.g.)
Compression	DWORD (4 bytes)	0 (no compression)
Image size	DWORD (4 bytes)	width × height × 3 (e.g. for 24 bpp)
Pixel per meter (x)	LONG (4 bytes)	0 (no information)
Pixel per meter (y)	LONG (4 bytes)	0 (no information)
Color table	DWORD (4 bytes)	0 (no color table)
Used color from table	DWORD (4 bytes)	0 (all color used)

Table A.8.: The second part of the header contains the information about the bitmap and has a length of 40 bytes. Here the properties of the image are stored.

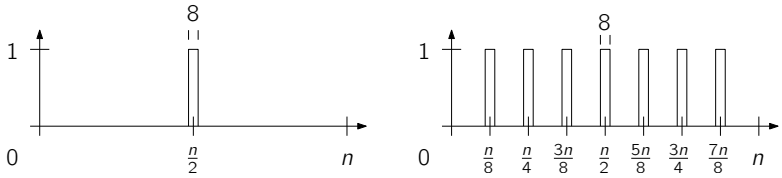

(a) Point (b) Circles

Figure A.2.: To test the backprojection filter simple projection patterns are used. The first pattern gives a single point and the second gives concentric circles.

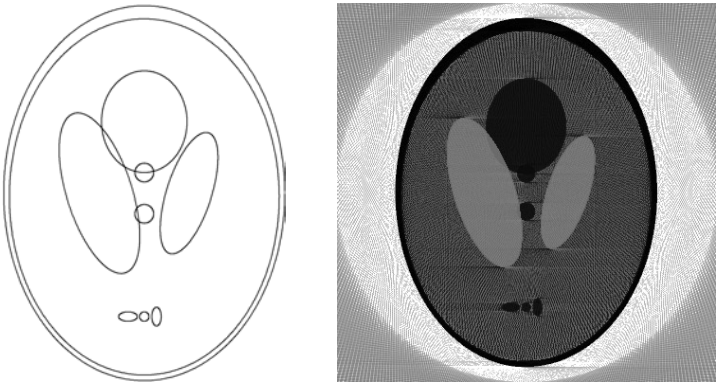

(a) Ellipses (b) Reconstruction

Figure A.3.: The head phantom proposed by Shepp-Logan. The head is constructed by ten ellipses.

In the two dimensional case (see figure A.4) the ellipses of the head phantom are described by the following equation

$$f(x,y) = \begin{cases} \rho & \text{for } \frac{x^2}{A^2} + \frac{y^2}{B^2} \leq 1 \\ 0 & \text{otherwise} \end{cases}$$

The equation of such an ellipse projection in the detector space t is

$$P_\theta(t) = \begin{cases} \frac{2\rho AB}{a^2(\theta)} \sqrt{a^2(\theta) - t^2} & \text{for } |t| \leq a(\theta) \\ 0 & \text{otherwise} \end{cases}$$

where θ is the angle between the x axis and the simulated detector and $a^2(\theta) = A^2 \cos^2\theta + B^2 \sin^2\theta$.

This is true for ellipses that are not rotated and their center is in the origin. If these two conditions are not fulfilled the projection becomes $P_\theta(t) = P_{\theta-\alpha}(t - s \cdot \cos(\gamma - \theta))$ where $s = \sqrt{x_c^2 + y_c^2}$ and $\gamma = \arctan\left(\frac{y_c}{x_c}\right)$. The two coordinates x_c and y_c describe the position of the center of the ellipse and α is the rotation angle between the ellipse and the x axis. The projection axis is t.

The extension from two to three dimensions consists in the following steps

- adding axis z;

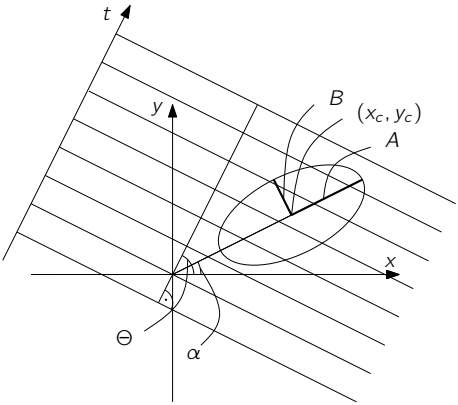

Figure A.4.: The projection of an ellipse into detector space. The various parameters are indicated.

- projection coordinate system $t \rightarrow v$ and w parallel to z;
- ellipsoid is defined additionally by a third axis C.

These ellipsoids have the following projection equation

$$P_{\theta,0}(v,w) = \frac{2\rho ABC}{a^2(\theta,0)} \left[a^2(\theta,0) - v^2C^2 - w^2 \left(A^2\cos^2\theta + B^2\sin^2\theta \right) \right]^{\frac{1}{2}} \qquad \text{(A.1)}$$

where a^2 is

$$a^2(\theta) = C^2 \left(B^2\sin^2\theta + A^2\cos^2\theta \right)$$

This equation only considers the case where the ellipsoid is in the origin. If this is not the case an additional transformation is needed. The coordinate v of the center must be projected to x and y

$$v_c = x_c\cos\theta - y_c\sin\theta$$

Afterwards the origin of the v,w coordinate system must be translated to the origin of the ellipsoid (x_c,y_c,z_c). This leads to the following translation

$$\begin{aligned} \bar{v} &= v - v_c = v - x_c\cos\theta + y_c\sin\theta \\ \bar{w} &= w - w_c = w - z_c \end{aligned}$$

With this equation and the equation (A.1) the projection depth of the ellipsoids for all the points (v,w) can be calculated.

A.2.1. Partial volume effect

The partial volume effect is an artifact in a tomographical backprojection. The object is not imaged continuously but with discrete pixels. The mesh in the image space can have different absorption capabilities in different directions. A simplified case is used to show the effect mathematically. In this case the absorption of two different meshes containing the same material is calculated. The first mesh is filled completely with a density of 50 %. In the second mesh only half of the volume is filled but with a density of 100 %. The setup is shown in figure A.5. A vertical beam would have the same absorption in both cases as $x \cdot \mu$ is constant. In the horizontal case the intensities averaged transmitted through the two meshes are

$$\begin{aligned} I_1 &= I_0 \exp\left(-x \cdot \frac{\mu}{2}\right) \\ I_2 &= \frac{I_0}{2} + \frac{I_0 \exp\left(-x \cdot \mu\right)}{2} \end{aligned}$$

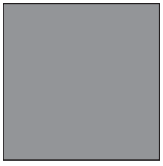

(a) 100 % of the volume with 50 % density

(b) 50 % of the volume with 100 % density

Figure A.5.: The partial volume effect is generated by the fact that (a) and (b) do not have the same absorption in all directions even though they have the same overall density.

The ratio of these two equations is

$$q = \frac{I_2}{I_1} = \frac{\frac{1}{2} + \frac{1}{2}\exp\left(-x\mu\right)}{\exp\left(-x\frac{\mu}{2}\right)} = \frac{1}{2} \cdot \frac{1 + \exp\left(-x\mu\right)}{\exp\left(-x\frac{\mu}{2}\right)} = \frac{1}{2}\left[\exp\left(x\frac{\mu}{2}\right) + \exp\left(-x\frac{\mu}{2}\right)\right]$$

In this equation the Taylor series of an exponential function can insert $e^c = 1 + \frac{c}{1!} +$

$\frac{c^2}{2!} + \ldots$

$$\begin{aligned} q &= \frac{1}{2}\left[1 + x\frac{\mu}{2} + \frac{(x\mu)^2}{8} + \ldots + 1 - x\frac{\mu}{2} + \frac{(x\mu)^2}{8} + \ldots\right] \\ &= 1 + \frac{(x\mu)^2}{8} + \ldots \geq 1 \\ I_2 &\geq I_1 \end{aligned}$$

The last inequality is true for the complete series because the components with an uneven exponent vanish. The remaining components have an even exponent and for $x \cup \mu \in \mathbb{R}$ those components must be positive. Therefore the q must be larger or equal to 1.

This leads to the conclusion that the inhomogeneous volumes absorb less than the homogeneous ones in some directions.

A.3. Multiple objects holder

Holders with multiple samples are used in this work to avoid a power cycle of the X-ray source. Those holders can be positioned by the rotation stage described in section 3.1.3. The selection of the sample is done by this rotation. The holder shown in figure 4.13 is used for the different plates. Two samples can be fixed on this holder at the same time. The procedure is used to detect the two edges of those samples. The angular positions are saved and for the measurement those positions can be approached. The algorithm of the edge detection is described in the next section. After the detection of the edge, the sample must be rotated so the beam crosses the sample. In this work the beam is moved **3.4 mm** $\widehat{=}$ **4.1°** from the edge in the sample as a standard value. Especially with a powder sample this value must be increased to avoid that the beam crosses the O-ring instead of the powder.

The second holder with multiple samples is the one with the cuvettes shown in figure 4.16. With this holder the procedure is different. Only the first cuvette is located in advance. The other cuvettes are detected for each measurement. The rotation stage makes a jump and afterwards the actual edge of the cuvette must be found. The position of the cuvettes is not accurate enough for a direct positioning without a search of the edge. From the edge the holder is rotated by **4.7°** to be in the middle of the cuvette.

A.3.1. Approach algorithm

The approach algorithm detects a change in the overall absorption. All channels are summed together and the exposure time is fixed to **1 s**. For the holder of the plates

the approach algorithm has two stages. This allows a rough positioning of the holder and still a fast and precise detection. Because the cuvettes in the second holder are in a more defined position a single stage search is sufficient. For the first holder the search covers 10° range with a step of 1.5°. The second stage has a step of 0.2°. The algorithm searches a drop of 50 % of the integrated counts.

For the second holder the procedure has steps of 0.5° over 4°. Because the cuvettes do not absorb so much the drop of count must exceed 33 %. For the latter approaches of the other cuvettes the steps are much smaller, typically 0.22°. The rotation form the middle of a cuvette to the next starting point of the approach algorithm is 19.7°.

A.4. Gaussian fit of fluorescence peaks

For the calibration of the spectrometer the position of fluorescence peaks is important. Those fluorescence peaks can be approximated by Gaussian peaks on top of a base signal. For simplicity the Gaussian is assumed to be starting from zero. The non-normalized form of a Gaussian is

$$y(x) = a \cdot e^{\frac{(x-b)^2}{2c^2}}$$

Because this equation has three parameters at least three measurement points are needed for the fitting.

The first step for the fitting is to take the logarithm of the last equation

$$\ln(y_i) = \ln(a) - \frac{(x_i - b)^2}{2c^2}$$

This equation represents a parabola in x and $\ln(y)$. A fit for the parabola can be made.

When the estimation is done with three points the following steps lead to the position. The difference of two points is taken to solve the fitting problem as

$$\begin{aligned} \ln y_1 - \ln y_2 &= \frac{(x_2 - b)^2 - (x_1 - b)^2}{2c^2} \\ \ln y_2 - \ln y_3 &= \frac{(x_3 - b)^2 - (x_2 - b)^2}{2c^2} \end{aligned}$$

Now the quotient q of these two equations is calculated as

$$q = \frac{\ln y_1 - \ln y_2}{\ln y_2 - \ln y_3} = \frac{2(x_1 - x_2)\,b + \left(x_2^2 - x_1^2\right)}{2(x_2 - x_3)\,b + \left(x_3^2 - x_2^2\right)}$$

The searched parameter b can be calculated as

$$b = \frac{q\left(x_3^2 - x_2^2\right) - \left(x_2^2 - x_1^2\right)}{2\left((x_1 - x_2) - q\,(x_2 - x_3)\right)}$$

If x represents the energy channels and all three channels are spaced by $x_2 - x_1 = x_3 - x_2 = 1$ then the equation can be further simplified to

$$b = \left(x_2 + \frac{1}{2}\right) + \frac{1}{q-1}$$

For better results more as three points can be used for the fit. In this case a least square root method must be applied to a polynomial equation of order three.

$$y(x) = Ax^2 + Bx + C$$

The maximum of the parable can be calculated by

$$\begin{aligned} \frac{dy(x)}{dx} &= 2Ax + B = 0 \\ x &= \frac{B}{2A} \end{aligned}$$

This last equation gives the position of the maximum of parable respective Gaussian peak. The least square root is solved with a QR algorithm as described in 4.4.3. Lots of fittings in this work are done with 7 points.

A.5. Regression

Most regressions in this work are done by a least square fit. The photoabsorption follows a power law. Logarithms are used to make a regression of a power law.

$$\frac{\mu}{\rho} = c \cdot E^a \ln\left(\frac{\mu}{\rho}\right) = \ln c + a \cdot \ln E$$

The two logarithms can be replaced $y = \ln\left(\frac{\mu}{\rho}\right)$ and $x = \ln E$. This gives an equation

$$y = \ln c + a \cdot x$$

This fit can be done with a least square regression. In contrary the solution of the power law will not be a least square fit. The error are distorted by the logarithm. The effect is visualized in figure A.6. Nevertheless this method is used for all power law fits in this work.

The same method with logarithms is also used in interpolations. For example when tabulated and measured data are used together.

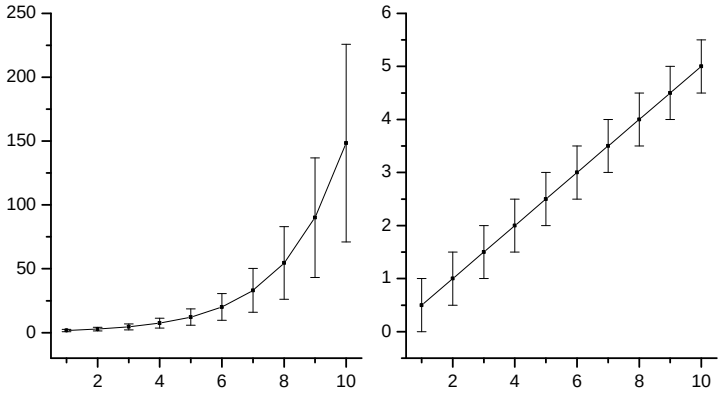

Figure A.6.: The power regression can be simplified if the function is linearized with logarithms. The constant error bars of the linear function (left) have the same size than the ones of the original power function (right). But the errors are not weighted equally anymore and therefore no least square regression is performed.

A.6. Technical drawings

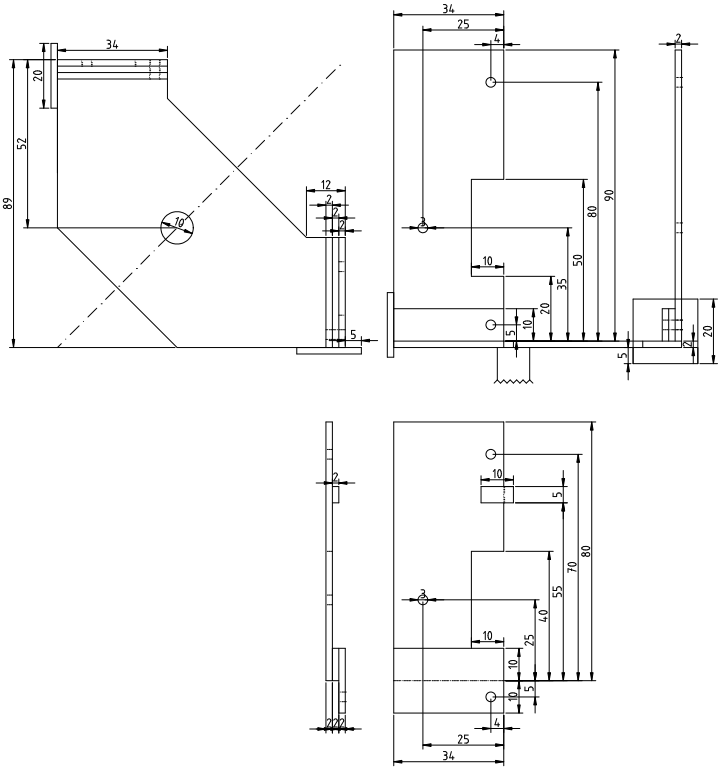

Figure A.7.: The plates holder consists of three pieces. The primary part is shown on top and two plates for the fixation are shown below.

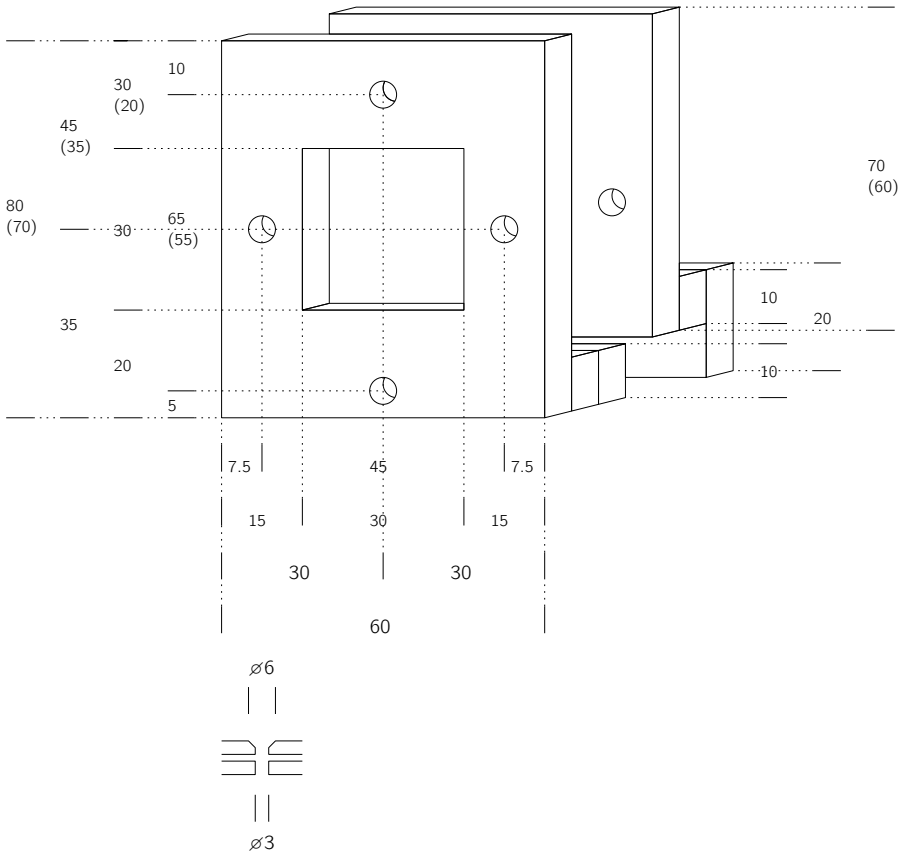

Figure A.8.: The holder to rotate the plate in the middle. The dimensions in the parenthesis are from the actual holder but are incorrect. The screw holes on top cannot be used.

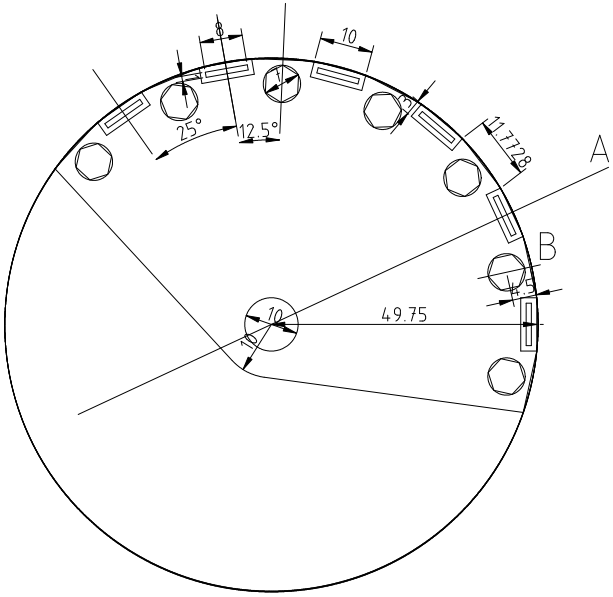

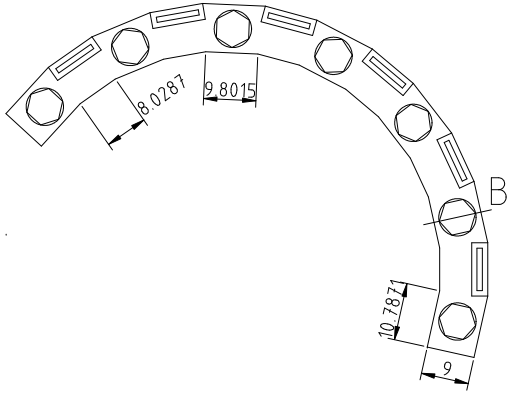

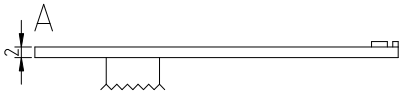

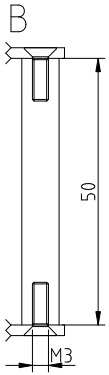

Kuevettenhalterung

CSEM SA Schulstrasse 1 CH-7302 Landquart	Datum: 15. 1. 2010		Rev:
	Gez: J. Nuesch		Rev:
	Format: A4		Rev:
	Mst: 1:1		

Bibliography

[1] Adobe Systems Incorporated. Tiff (tagged image file format) revision 6.0. specification, 1992.

[2] R. E. Alvarez, A. Macovski. Energy-selective reconstructions in x-ray computerised tomography. *Physics in Medicine and Biology*, 21(5):733–744, 1976. doi:10.1088/0031-9155/21/5/002.

[3] Amptek, Inc., Bedford MA. *Digital Pulse Processor DP4 - User's Guide and Operating Instructions*, 2008.

[4] Apogee Instruments Inc. High Performance Cooled CCD Camera System ALTA U2000 & U2000C. URL `http://www.ccd.com/pdf/U2000.pdf`. Specs.

[5] L. S. Avila, S. Barré, R. Blue, et al. *The VTK User's Guide*. Kitware, Inc., 2006. Update for VTK Version 5.

[6] E. P. Bertin. *Principles and Practice of X-Ray Spectrometric Analysis*. Plenum Press, New York, 2nd edn., 1975. ISBN 0-306-30809-6.

[7] L. S. Birks, E. J. Brooks, H. Friedman. Fluorescent x-ray spectroscopy. *Analytical Chemistry*, 25(5):692–697, 1953. ISSN 0003-2700. doi:10.1021/ac60077a004.

[8] C. T. Chantler, K. Olsen, R. A. Dragoset, et al. X-Ray Form Factor, Attenuation, and Scattering Tables. Tech. rep., National Institute of Standards and Technology, Gaithersburg, MD, 2005. URL `http://physics.nist.gov/ffast`. Originally published as Chantler, C.T., J. Phys. Chem. Ref. Data 29(4), 597-1048 (2000); and Chantler, C.T., J. Phys. Chem. Ref. Data 24, 71-643 (1995).

[9] M. Cooper. X ray compton scattering. *Physics Education*, 7(7):449–452, 1972. doi:10.1088/0031-9120/7/7/014.

[10] P. Deuflhard, A. Hohmann. *Numerische Mathematik*. Walter de Gruyter, Berlin, 1991.

[11] Deutsches Institut für Normung e.V. Zerstörungsfreie Prüfung - Strahlenschutzregeln für die technische Anwendung von Röntgeneinrichtungen bis 1MV - Teil 3: Formeln und Diagramme für Strahlenschutzberechnungen für Röntgeneinrichtungen bis zu einer Röhrenspannung von 450 kV, 2005.

[12] W. Duane, F. L. Hunt. On x-ray wave-lengths. *Physical Review*, 6(2):166–172, 1915. doi:10.1103/PhysRev.6.166.

[13] Eastman Kodak Company. Kodak KAI-2020 Image Sensor, 2007.

[14] O. Glasser. *Wilhelm Conrad Röntgen and the early history of the Roentgen rays*. John Hale, London, 1933.

[15] Hamamatsu Photonics K.K. Microfocus X-Ray Source L10101. URL `http://sales.hamamatsu.com/assets/pdf/parts_L/L10101_TLSO1062E01.pdf`. Specs.

[16] J. H. Hubbell, S. M. Seltzer. Tables of X-Ray Mass Attenuation Coefficients and Mass Energy-Absorption Coefficients. Tech. rep., National Institute of Standards and Technology, 1996. URL `http://www.physics.nist.gov/PhysRefData/XrayMassCoef/cover.html`.

[17] Incom Corp. BLS59-18. Online [2009]. URL `http://incomusa.com/pages/bls59-18.html`.

[18] A. C. Kak, M. Slaney. *Principles of Computerized Tomographic Imaging*. IEEE Press, New York, 1988. ISBN 0-87942-198-3. URL `http://www.slaney.org/pct/`.

[19] K. Kanaya, S. Okayama. Penetration and energy-loss theory of electrons in solid targets. *Journal of Physics D: Applied Physics*, 5:43–58, 1968. doi:10.1088/0022-3727/5/1/308.

[20] O. Klein, Y. Nishina. Über die Streuung von Strahlung durch freie Elektronen nach der neuen relativistischen Quantendynamik von Dirac. *Zeitschrift für Physik A Hadrons and Nuclei*, 52(11–12):853–868, 1929. doi:10.1007/BF01366453.

[21] X. Llopart, R. Ballabriga, M. Campbell, et al. Timepix, a 65k programmable pixel readout chip for arrival time, energy and/or photon counting measurements. *Nuclear Instruments and Methods in Physics Research Section A: Accelerators, Spectrometers, Detectors and Associated Equipment*, 581(1-2):485–494, 2007.

[22] C. Lotto, P. Seitz. Synchronous and Asynchronous Detection of Ultra-Low Light Levels. In *Proceedings of the 2009 International Image Sensor Workshop, Bergen, Norway*. 2009.

[23] M. Moszynski, T. Ludziejewski, D. Wolski, et al. Properties of the yag:ce scintillator. *Nuclear Instruments and Methods in Physics Research Section A: Accelerators, Spectrometers, Detectors and Associated Equipment*, 345(3):461 – 467, 1994. ISSN 0168-9002. doi:DOI:10.1016/0168-9002(94)90500-2.

[24] Norland Products Inc. Norland Optical Adhesive 61. Online [2010]. URL `https://www.norlandprod.com/adhesives/NOA%2061.html`.

[25] G. Ramachandran, A. Lakshminarayanan. Three-dimensional Reconstruction from Radiographs and Electron Micrographs: Application of Convolutions instead of Fourier Transforms. *Proceedings of the National Academy of Sciences of the United States of America*, 68(9):2236–2240, 1971.

[26] W. C. Röntgen. Über eine neue Art von Strahlen. *Annalen der Physik*, 300(1):12–17, 1898.

[27] E. Samei, N. T. Ranger, J. T. D. III, et al. Intercomparison of methods for image quality characterization. I. Modulation transfer function. *Medical physics*, 33(5):1454, 2006.

[28] R. Schieder, G. Rau, B. Vowinkel. Characterization and Measurement of System Stability. In *Society of Photo-Optical Instrumentation Engineers (SPIE) Conference Series*, vol. 598, pp. 189–192. 1985.

[29] J. Schlomka, E. Roessl, R. Dorscheid, et al. Experimental feasibility of multi-energy photon-counting K-edge imaging in pre-clinical CT. *Physics in Medicine and Biology*, 53(15):4031–4047, 2008. doi:10.1088/0031-9155/53/15/002.

[30] F. Scholze, H. Rabus, G. Ulm. Mean energy required to produce an electron-hole pair in silicon for photons of energyies between 50 and 1500 eV. *Journal of Applied Physics*, 84(5):2926, 1998. doi:10.1063/1.368398.

[31] H. R. Schwarz. *Numerische Mathematik*. B. G. Teubner, Stuttgart, 4th edn., 1997. ISBN 3-519-32960-3.

[32] L. A. Shepp, B. F. Logan. Reconstructing interior head tissue from x-ray transmissions. *IEEE Transactions on Nuclear Science*, 21(1):228–236, 1974. doi:10.1109/TNS.1974.4327466.

[33] E. Sickles. Mammographic features of "early" breast cancer. *Am. J. Roentgenol.*, 143(3):461–464, 1984.

[34] P. Sprawls. *Physical Principles of Medical Imaging*. Medical Physics Publishing Corporation, Madison, WI, 2nd edn., 1995. ISBN 0944838545. URL `http://www.sprawls.org/ppmi2/`.

[35] A. C. Thompson, D. Vaughan, eds. *X-RAY DATA BOOKLET*. Lawrence Berkeley National Laboratory, University of California, Berkeley, California 94720, 2nd edn., 2001.

List of Patents

- J. Nüesch, P. Seitz, "Authentication item and system for packaged articles and method for the manufacturing of the authentication item", European patent application, No. 10157911.8
- J. Nüesch, P. Seitz, "System and method for determining the composition of an object", Swiss patent application, No. 00511/10

List of Figures

List of Tables